Evolution of Microstructure and Its Effect on Mechanical Properties of Additively Manufactured Ni-based Superalloy During Heat Treatment

by

Tahmina Keya

A dissertation submitted to the Graduate Faculty of
Auburn University
in partial fulfillment of the
requirements for the Degree of
Doctor of Philosophy

Auburn, Alabama
August 5, 2023

Keywords: Laser Powder Bed Fusion, Ni-based Superalloy, Inconel 625, Microstructure

Approved by

Barton Charles Prorok, Chair, Professor, Materials Engineering
Dong-Joo Kim, Professor, Materials Engineering
Xiaoyuan Lou, Former Associate Professor, Materials Engineering
Byron H Farnum, Associate Professor, Chemistry and Biochemistry
Elham Mirkoohi, Assistant Professor, Mechanical Engineering

ABSTRACT

Additive Manufacturing (AM) is a powerful tool to manufacture parts with unique benefits over traditional manufacturing, such as design freedom, reduction in manufacturing time and time, enabling use of broad range of materials etc. Laser Powder Bed Fusion is an AM technique that provides better part density and high dimensional accuracy. But there are some challenges associated with AM/LPBF process such as porosity, inclusion, complex residual field etc. which affect microstructure and mechanical properties of the material. Post-processing can tailor the microstructure to wrought standard, hence designing suitable heat treatment for LPBF parts is crucial. This study investigates microstructural evolution through various heat treatment schedules at different temperatures for different times that provides better understanding of tailoring desired microstructure and mechanical properties. LPBF Inconel 625 parts were heat treated at 700^{o}C, 900^{o}C and 1050^{o}C for various lengths of time from 1 hour to 40 hours depending on objectives of the study. Then microstructure and hardness are compared between as-printed LPBF and wrought material.

Fine dendritic microstructure with visible melt pool boundaries was detected in as-printed LPBF IN625. Columnar growth of grains along the build direction was also observed that is caused by downward heat transfer towards the substrate. Strengthening γ'' precipitate was detected in as-printed condition using transmission electron microscopy (TEM) that not only proves its presence, but also reveals its type. Very few researchers mentioned this phenomenon previously, but did not present with convincing proof. Hardness of as-printed IN625 is much higher than traditionally wrought IN625 due to its fine dendritic microstructure with the presence of γ'' precipitates.

LPBF IN625 that were heat treated at 700°C for 1h showed presence of γ'' precipitates as well. The 3rd variant is also visible after this heat treatment which indicates presence of tensile

residual stress in as-printed condition that promoted the growth of this variant. The dendritic microstructure as well as the melt pool boundaries are still visible after heat treatment at 700℃ for 1, 2, 5 and 10h, but the columnar growth seems to be remodeled with increasing heating time. The hardness initially increases after 1h from as-printed, then decreases with increasing time until it increases again after 10h.

Heat treatment at 900℃ caused precipitation of δ phase that appears as plate or needle in the microstructure. With increasing time from 1 to 40h, the precipitates grow in size and amount. The precipitates on grain boundaries grew larger than the ones inside the grains. Hardness values for this temperature are lower than those for 700℃ due to the dissolution of strengthening γ″ phase and formation of δ phase. Further analysis on this precipitate revealed that precipitation occurs much faster on the surface exposed to the furnace ambience during heat treatment compared to that in the bulk of the sample. Volume fraction analysis revealed that 1% precipitation of δ phase occurs in between 2 to 5 h in LPBF IN625 when heat treated at 900℃.

The anisotropic and heterogenous microstructure becomes fully recrystallized after heat treating at 1050℃. Melt pool boundaries, dendritic structure and precipitates are completely dissolved, however, carbides are detected at this temperature. These carbides get redistributed and remodeled with increasing heating time. Hardness values are lowest at this temperature due to the dissolution of precipitates as well as stress relief. Metal oxide inclusions in the form of Al_2O_3 has been found in all heat treatment conditions.

This study is a useful resource to understand the evolution of microstructure and precipitates in LPBF IN625 on its way to complete recrystallization. We have also been able to achieve a range of hardness that can be tailored using suitable heat treatment. Volume fraction

analysis of δ phase can contribute to the establishment of new TTT diagram for LPBF IN625 in future.

TABLE OF CONTENTS

LIST OF TABLES

LIST OF FIGURES

LIST OF ABBREVIATIONS

AM	Additive Manufacturing
LPBF	Laser Powder Bed Fusion
SEM	Scanning Electron Microscopy
BSE	Backscatter Electron
EBSD	Electron Backscatter Diffraction
EDS	Energy Dispersive Spectroscopy
XRD	X-Ray Diffraction
TEM	Transmission Electron Microscopy
FIB	Focused Ion Beam
TTT	Time Temperature Transformation
FFT	Fast Fourier Transformation
GB	Grain Boundary

CHAPTER 1: INTRODUCTION

1.1 Additive Manufacturing

Additive manufacturing (AM) can be defined as the process of manufacturing a part from its three dimensional computer aided design (3D CAD) model by adding layers of material without process planning [1,2]. The term 'additive manufacturing' is the formal name of the process 'rapid prototyping' which is also popularly known as '3D printing'. Rapid prototyping used to refer as the manufacturing process where a part is rapidly produced from its CAD design before releasing in the market. Therefore, it is basically presenting the physical prototype of the actual product in its complete 3D form unlike only giving an idea about the design. Even though it started with 'prototyping', since parts were actually produced in bulk using the additive approach, the ASTM has adopted the new term 'additive manufacturing' for this particular type of manufacturing which is now widely being used in general. The typical steps in most AM processes are shown in Fig. 1.

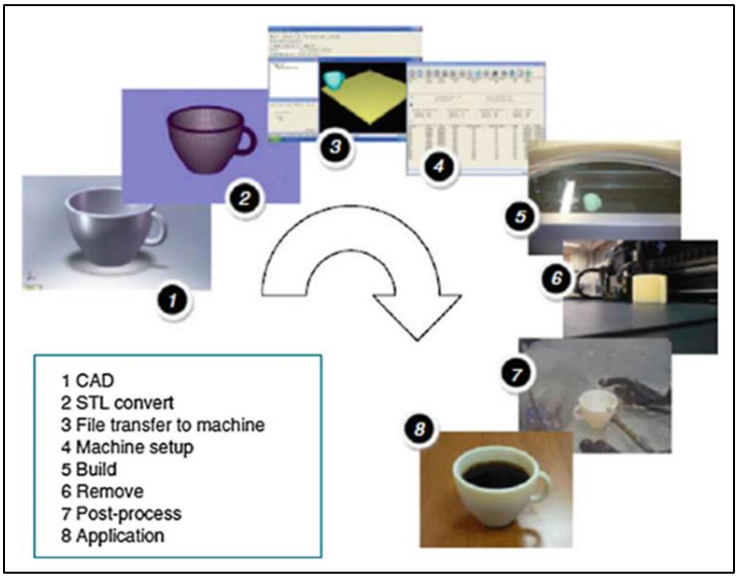

Figure 1: Steps in Additive Manufacturing process [1]

Unlike traditional manufacturing processes, additive manufacturing deals with the entire part as a whole instead of looking at details and separating it into segments since the entire part can be fabricated from its 3D model as one single body. But additive manufacturing emphasizes on making the design properly and understanding the manufacturing machine. This gives the freedom of design while making a very intricate object. A part is made by adding layer upon layer, so the layers must have a finite thickness. Also, the final outcome depends on how the layers melt and bond with each other. This also determines how the post processing will be performed. So, additive manufacturing has its own requirements and systems to get a perfectly fabricated part. Some advantages of AM processes are:

- As the name 'rapid prototyping' implies, the process is rapid. Time is a major concern when it comes to business and AM gives speed in manufacturing products. It does not require process management since it is usually done in one step. Even if the design is changed, it will only change some parameters in the process, but not number of steps. So, no matter how complex the design is, it will produce the part in just one single step.
- Number of processes and resources gets significantly lower for additive manufacturing compared to casting and molding [1]. Several molds may need to be built to produce a single part in molding. In addition to that, several fixtures may also need to be produced to use in CNC machining. In AM process, since the part is produced directly from its CAD model, no extra mold or fixture is necessary.
- AM eliminates the requirement of skilled labor. It obviously require someone expert to operate and maintain the machine, but any manual crafting or operating while building the part are not necessary.

- It is possible to use AM technology in conjunction with traditional processes which will make the entire manufacturing process much cleaner and well managed.
- Freedom of part design complexity is one of the most important advantages of AM process. The more complex the design is, the more applicable this technology becomes. Because, traditional manufacturing techniques can become tedious and time consuming if the design becomes intricate. But in AM process, complexity of design hardly matters.

1.2 Laser Powder Bed Fusion

The first commercial AM process was Selective Laser Sintering (SLS) which is a Powder Bed Fusion (PBF) process and was first developed the University of Texas at Austin. During Laser Powder Bed Fusion (LPBF) process, a focused high-energy laser beam selectively melts a powder layer accompanied with rapid cooling/solidification for a predetermined shape defined via computer aided drawing (CAD) data. This process is followed by the coating of a new powder layer that is melted selectively to the previous layer. This cycle goes on until the final product is completely manufactured. A schematic diagram of LPBF process is shown in Fig. 2(a). During the melting, high localized heat associated with high power is produced in a small area causing high thermal gradient [3]. During solidification, cooling rate can be as high as 10^3 K/s to 10^6 K/s whereas tradition methods, e.g. casting has a cooling rate in the order of 1 to 1000 K/s [4]. This complex thermo-mechanical phenomena leads to fine dendritic inhomogeneous microstructure and residual stress. This unique microstructure produced by LPBF techniques requires separate investigation since its performance in different applications especially in extreme conditions can introduce some benefits as well as challenges compared to wrought materials. LPBF process enables producing complex parts using wide range of metals and alloys with high dimensional accuracy. Examples of LPBF produced parts are shown in Fig. 2 (b, c).

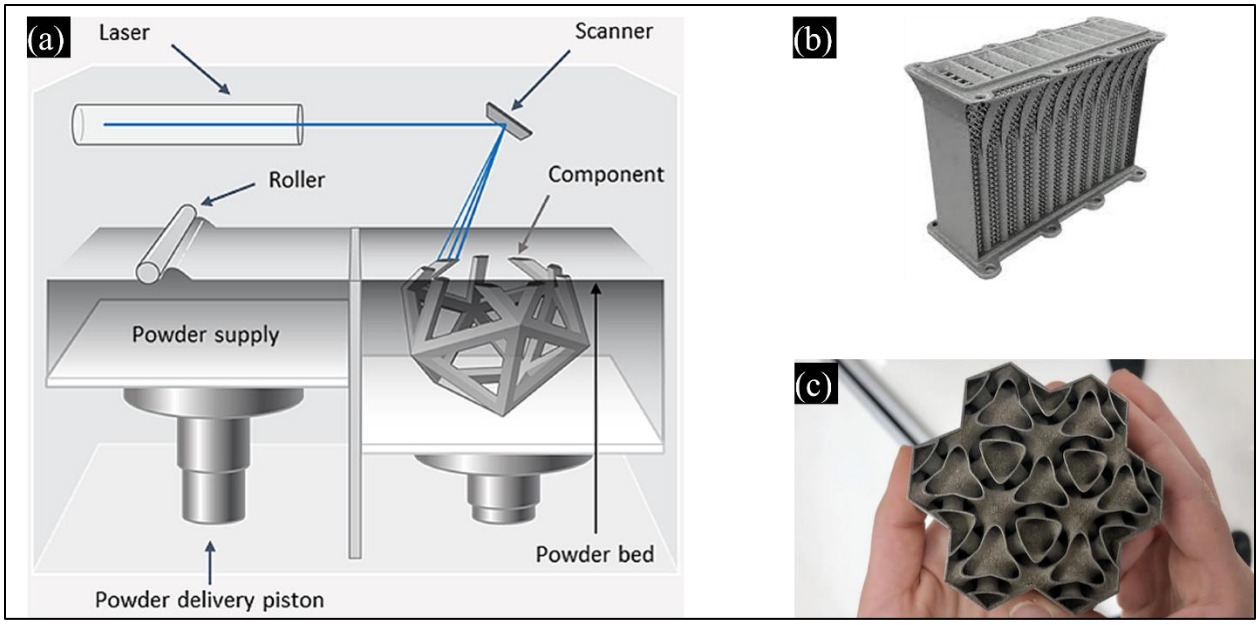

Figure 2: (a) Laser Powder Bed Fusion process [5]; (b-c) examples of LPBF produced complex parts [6,7].

1.3 Ni-based Superalloys

Nickel is one of the most versatile elements and being used for many applications since the beginning of civilization [8]. It is used as a base of many alloys since its wide solubility range makes it easy to form alloys with several other metals like iron, chromium, copper etc. Nickel alloys have wide range of applications due to their following unique properties [4] :

- Nickel-chromium alloys are ideal to be used as electric resistance heating elements due to their high resistivity and heat resistance;
- Nickel-iron alloys have soft magnetic properties which make them suitable for electronic devices;
- Equiatomic nickel-titanium alloys have shape memory characteristics to be used as actuators, hydraulic connectors and eyeglass frames;

- Wrought nickel-beryllium-titanium alloys have high strength at elevated temperature and these are resistant to stress relaxation, so are suitable for electronic applications such as springs subjected to elevated temperatures;
- Cast nickel-beryllium-carbon alloys have high thermal conductivity and wear resistance, so these can be used for tooling in glass forming operations.

Some other applications pf nickel and nickel alloys include [4] :

- Aircraft gas turbines
- Steam turbine power plants
- Medical applications
- Nuclear power systems
- Chemical and petrochemical industries

Sometimes nickel is used by itself in pure form or after adding very small amount of other metals for enhanced properties. Some of the important variants of nickel and nickel alloys are discussed here:

- **Pure nickel:** Nickel 200, Nickel 201, Nickel 205, Nickel 270 and 290, Permanickel Alloy 300, Duranickel Alloy 301 are some examples of commercial nickels where at least 94% nickel is used.
- **Nickel-Copper alloys:** These alloys have high corrosion resistance, thus making it useful for environment like sea water for nuclear submarines. Alloy 400 (66% Ni, 33% Cu), Alloy R-405, Alloy K-500 are some of the examples of nickel-copper alloys.
- **Nickel-Chromium-Iron alloy:** These are known for their high strength at elevated temperature. Some of most used alloys are Alloy 601(61% nickel), Alloy X750, Alloy 718 etc. Alloy 625, Alloy G3/G30 (Ni-22Cr-19Fe-7Mo-2Cu), Alloy C-22 (Ni-22Cr-6Fe-14Mo-4W),

Alloy C-276 (17% Mo plus 3.7W), Alloy 690 (27% Cr addition) etc. offer higher corrosion resistance as well.

Inconel 625 (IN625) is a nickel superalloy with exceptionally superior mechanical properties that derives its strength from solid solution strengthening by Chromium (Cr), Molybdenum (Mo) and Niobium (Nb) atoms [9–11]. In addition to solid solution strengthening, IN625 exhibits precipitation hardening primarily from the precipitation of fine metastable γ″ phase. It is suitable for high temperature applications and is corrosion resistant making it an ideal candidate for aerospace, medical or energy sector.

1.4 Major Phases of IN625

IN625 derives its superior strength from solid solution strengthening by primarily Nb and Mo. It is also prone to form secondary phases at elevated temperature that results in precipitation hardening in the material [11,12]. Various heat treatments introduce different precipitates in Ni-based superalloys depending on annealing temperature and aging time. Major phases present in as-received and heat treated Inconel 625 are given in table 1 [13,14].

Table 1: Major Phases in IN625

Phases and their crystal structure	Composition in IN625
γ matrix FCC	Ni-Cr
γ′ FCC	Not significant
γ″ BCT	Ni_3(Nb, Ti, Al)
δ Orthorhombic	Ni_3Nb
Pt_2Mo type Body Centered Orthorhombic	Ni_2(Cr, Mo)

Laves HCP	$(Cr, Fe, Ni)_2(Si, Nb, Mo, Ti)$
Carbides Cubic	MC, M_6C, $M_{23}C_6$

The microstructure produced by AM techniques is significantly different than that by traditional manufacturing processes [9,15–19]. The fast cooling rate during LPBF process produces a fine dendritic microstructure with elemental segregation on interdendritic boundaries. Such microstructure greatly influence the precipitation behavior in LPBF IN625. Precipitation is likely occur much faster in LPBF IN625 compared to that in its wrought counterparts [19–21]. There are 5 major precipitates in IN625 that have been addressed in the literature namely γ″, δ, and carbides such as MC, M_6C and $M_{23}C_6$ [22]. Oxide inclusions have also been mentioned in a number of studies [18,23,24]. A schematic diagram of the primary γ phase, strengthening γ″ phase as well as detrimental δ phase is shown in Fig. 3.

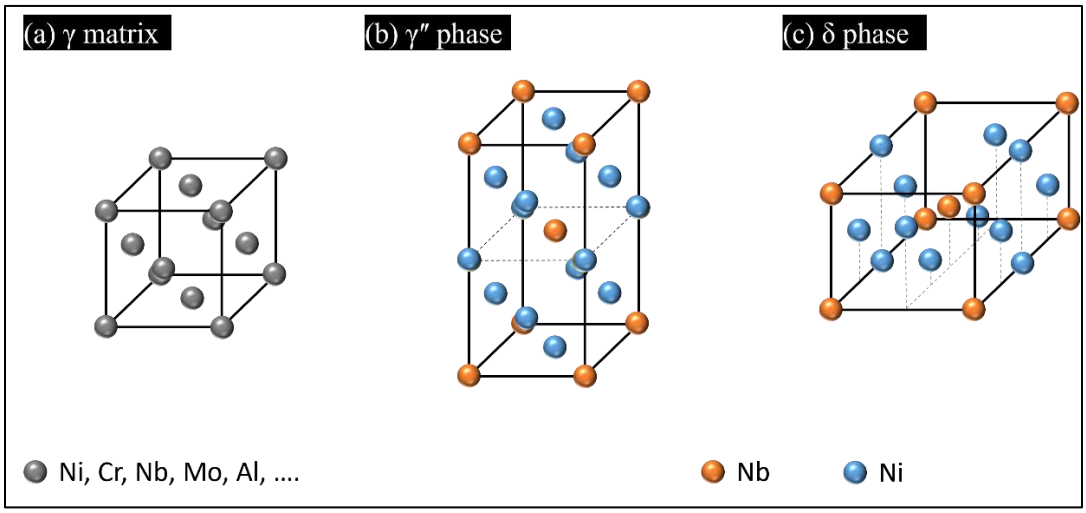

Figure 3: Crystal structure of major phases in IN625; (a) primary γ matrix, (b) strengthening γ″ phase, and (c) detrimental δ phase.

γ″ is the major strengthening precipitate in IN625 [11,25,26]. It is a body centered tetragonal (BCT) $D0_{22}$ phase with chemical composition of $Ni_3(Nb, Ti, Al)$ [13,25,27–29]. Several

research groups reported formation of metastable γ″ precipitate in the range of 550-750°C temperature [13,26,28,30,31]. These precipitates can be plate, disc, lens, spherical or elliptical shape. There are 3 variants of γ″ precipitates that are shown in Fig. 4(b) [32]. The orientation relationship between the 3 variants of γ″ and the parent phase γ is as follows [33]:

$$(100)\gamma'' \parallel \{100\}\gamma,\ [100]\gamma'' \parallel \langle 100\rangle\gamma''$$

It can be observed from Fig. 3(a, b) and 4(a) that the c-axis of γ″ phase is longer than that of γ phase. IN625 derives its precipitation hardening from the strain caused by this lattice mismatch [25,32]. It can take long time to form γ″ phase in traditionally manufactured IN625 [13], but precipitation may occur as soon as in 1h in AM produced materials [9,34]. Amato et al. reported formation of γ″ precipitate in as-built IN625 produced via selective laser melting [15]. However, it is difficult to be certain about the presence of γ″ with characterization techniques such scanning electron microscopy (SEM), energy dispersive spectroscopy (EDS) or X-ray diffraction (XRD), especially when the size and amount of the precipitate are small [35]. The XRD peaks of γ matrix and γ″ phase virtually overlap [31]. Therefore, presence of γ″ precipitate in as-built condition or short-term heat treatment condition have rarely been presented with convincing proof.

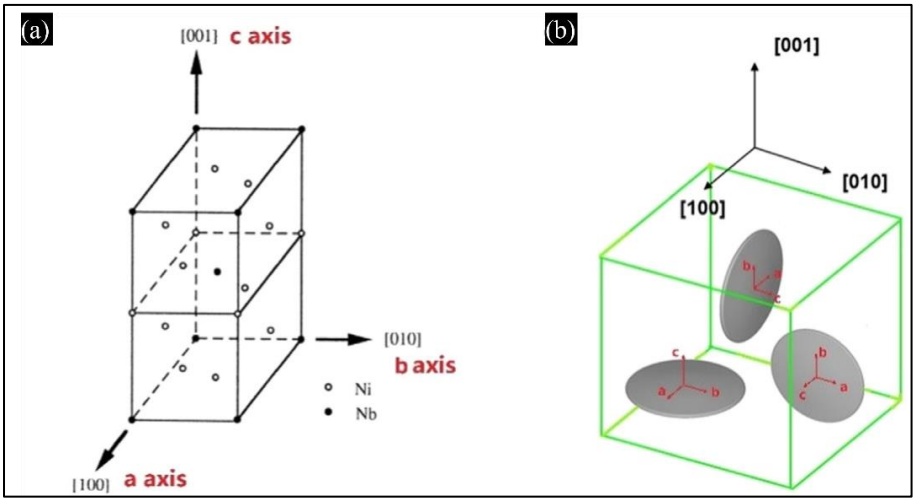

Figure 4: Schematic representation of (a) γ″ crystal structure with 3 axes, and (b) 3 different variants of γ″ precipitates with respect to FCC γ crystal [32].

A more studied precipitate that forms in IN625 is δ precipitate that has orthorhombic $D0_a$ structure with composition of Ni_3Nb or $Ni_3(Nb, Mo)$ [13,36]. It can be acicular, plate or globular shaped. There are total 12 variants of δ phase with the following orientation relationship with γ matrix [37]:

$$(010)\delta \parallel \{111\}\gamma, [100]\delta \parallel \langle 110\rangle\gamma$$

Researchers have reported formation of δ phase formation at 650-982℃ [13,28,36,38]. Stable δ phase forms from metastable γ″ precipitates when it dissolves into the matrix leaving high local concentration of Nb atoms [34,38]. It usually starts forming at grain boundaries, then spreads out throughout the grain. δ precipitates form much faster in AM materials compared to wrought IN625 [9,20]. Due to nature of LPBF process, there is Nb enrichment along interdendritic regions that triggers formation of precipitates that are Cr deficient, but enriched with larger Nb and Mo atoms. Stoudt et al. reported formation of δ particles in LPBF IN625 at 870℃ after 15 minutes [20]. They found δ precipitation on interdendritic region that grew in size and amount with increase in time. Lass et al. reported formation of plate shaped δ precipitates at 870℃ for 1h in LPBF IN625 [9]. Based on these findings, an attempt was made to establish a revised TTT diagram for LPBF IN625 showing approximately 1% δ precipitate (Fig. 6b) [20]. However, the presence of δ phase was determined by XRD on the outer or external surface of the sample. Supporting SEM images were taken from etched internal surfaces of the sample. It has been established that chromium oxide layer formed during heat treatment causes a continuous layer of δ precipitates underneath the oxide scale at the oxide-alloy interface [39–41]. Chyrkin et al. found that chromium oxide formation on the outer surface of forged IN625 causes Cr depletion right below the oxide scale which indirectly triggers Nb diffusion towards the scale after heat treating it for 1000h at 900℃. This Nb enrichment acts as the driving force to form large amount of δ precipitates at the scale-

alloy interface and a precipitate free zone below the δ phase-rich zone due to lack of Nb there (Fig. 5d) [41]. Parizia et al. reported similar observations for LPBF IN625 that was heat treated for 8h at 900°C as shown in Fig. 5(a-c) [39]. δ precipitates were found at the grain boundary (red arrows) as well as inside grains (red circles) in the bulk sample and at the alloy-oxide interface indicated by yellow dashed arrows. XRD scan on the outer surface revealed presence of Cr_2O_3 and δ phase. The study found that there is indeed Cr depletion below the oxide scale which caused Nb migration towards the oxide layer. This phenomenon can be explained by the fact that solubility of Nb increases in γ matrix at the absence of Cr [42]. Based on the above mentioned studies, it is clear that XRD scans on the oxide-rich external surface is not ideal to predict precipitation behavior of IN625. Moreover, etching a surface can erroneously exaggerate presence of certain phases.

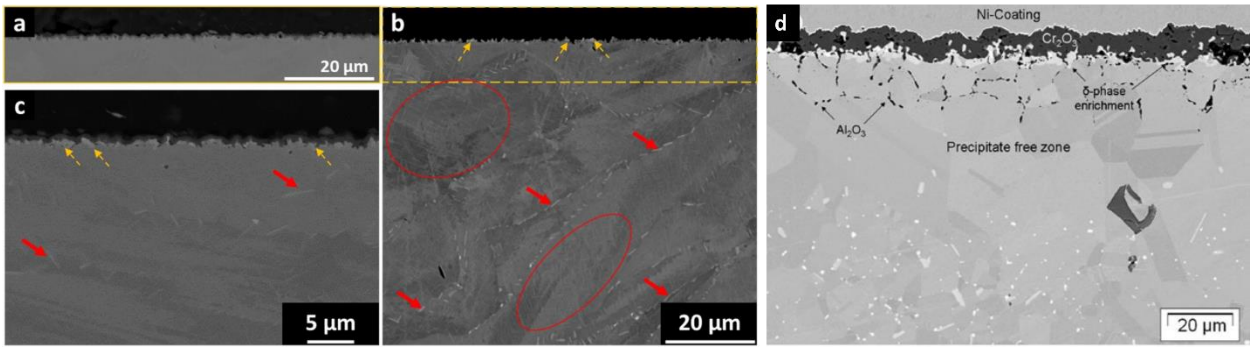

Figure 5: SEM images of cross sections of (a, b, c) LPBF IN625 heat treated at 900°C for 8h [39], and (d) forged IN625 oxidized at 900°C for 1000h [41].

Carbides are also found in traditionally and additively manufactured IN625. They have cubic crystal structure with compositions of Nb-rich MC, Ni, Cr and Mo-rich M_6C and Cr-rich $M_{23}C_6$ [13,21,22]. These carbides can form both in grain boundaries (GB) as well as in matrix and can contribute to the strengthening of IN625 [11]. They usually appear in blocky, globular, dendritic or irregular, random shape. The primary carbide MC is usually transformed into secondary M_6C or $M_{23}C_6$ upon aging heat treatment [21,22]. Carbides can be found in AM produced IN625 in both as-built as well as heat treated conditions [9,18,21,34,43,44]. Metallic and

non-metallic oxides are also found in AM produced alloys. These oxide formation is promoted by the oxygen inclusion in the material during inert gas atomization process and presence of moisture/oxygen in the build chamber [23,24,45,46]. Lou et al. reported presence of Si-rich oxide in LPBF stainless steel and its detrimental effect on the mechanical properties in high temperature water environment [47]. Deng et al. reported formation and evolution of Si, Mn-rich non-metallic oxides or Cr-rich metallic oxide in absence of Si/Mn in LPBF 316L [46]. Few researchers mentioned metallic oxide formation in AM as-built and heat treated IN625 [18,23,24].

Time-Temperature-Transformation (TTT) diagram is a useful tool that describes precipitation behavior of an alloy. A typical TTT diagram for wrought IN625 is shown in Fig. 6(a) [12] and a proposed TTT diagram for δ phases in LPBF IN625 is shown in Fig. 6(b) as mentioned earlier [20].

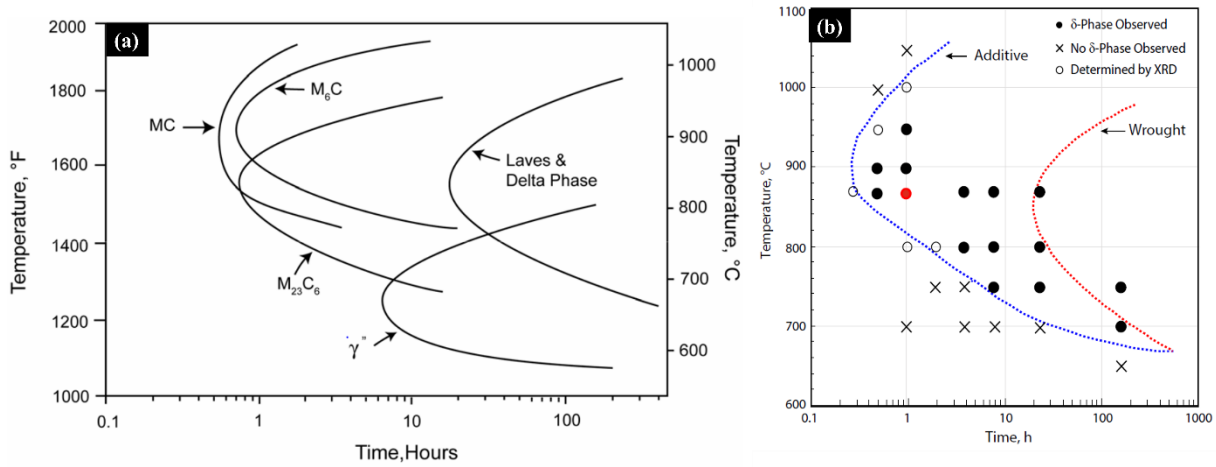

Figure 6: TTT diagram of IN625, (a) wrought [12], and (b) LPBF [20].

1.5 Additive Manufacturing of Ni-based Superalloys

Ni-based superalloys are known for their superior strength and high hardness, but their mechanical properties also make it difficult to produce complex parts using traditional subtractive manufacturing techniques [48]. Therefore, they are widely applied in different AM technologies that can be used in various industries that require superior performance in extreme environments.

One of the most studied Ni-based superalloy for AM, especially LPBF technology is Inconel 718 (IN718). IN718 is also strengthened by γ″ phase in addition to γ′ phase [13,49]. Typical as-printed microstructure of IN718 produced by LPBF technique is shown in Fig. 7 [50]. Columnar grain growth along build direction can be observed on XZ and YZ surfaces. This directionally solidified microstructure is influenced by vertical heat flux direction from cooler substrate. Microstructure consisting of laser track morphology can be observed on XY plane. LPBF IN718 is also highly susceptible to elemental segregation of Nb, Mo and C atoms. This elemental segregation causes formation of brittle intermetallic phases including δ and Laves during manufacturing process [50].

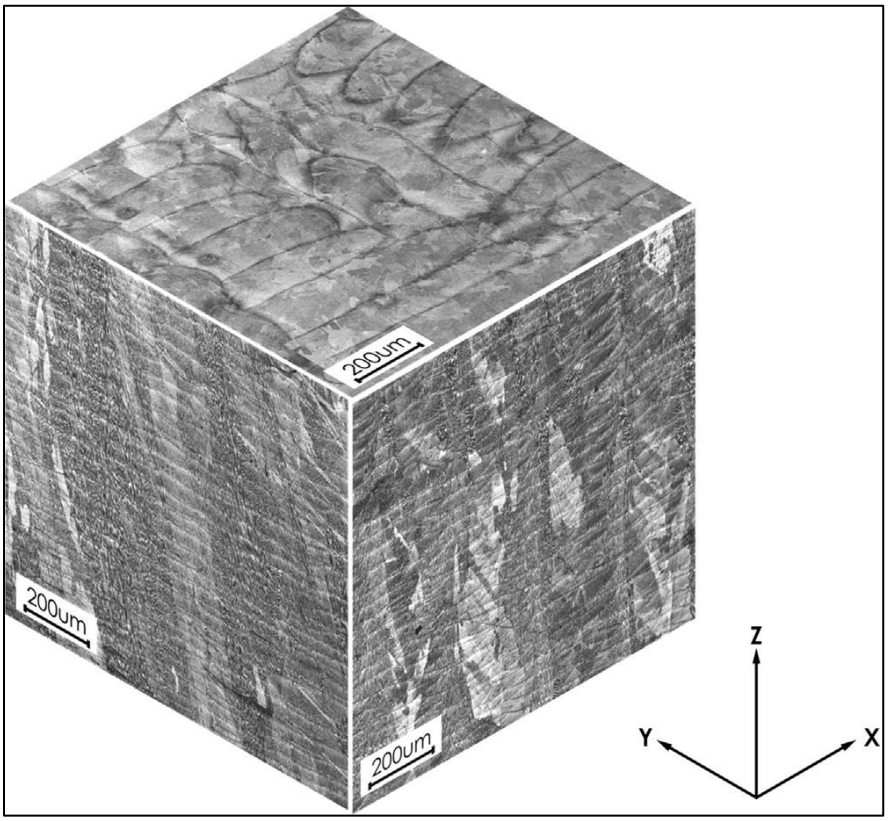

Figure 7: Microstructure of as-built LPBF IN718 [50]

Another Ni-based superalloy that has been successfully applied AM is Hastelloy X. Columnar growth and strong {001} texture along build direction have been reported for LPBF Hastelloy X as well [51]. Zhang et al. investigated the effect of different scanning strategy for

LPBF Hastelloy X and reported that island scanning strategy with 67^{o} hatch angle provide optimal mechanical properties. Marchese et al. reported dendritic microstructure with elemental segregation at the dendritic boundaries in as-built LPBF Hastelloy X [52] as shown in Fig. 8. Similar microstructural features have been reported for other Ni-based superalloys produced via LPBF [48,53].

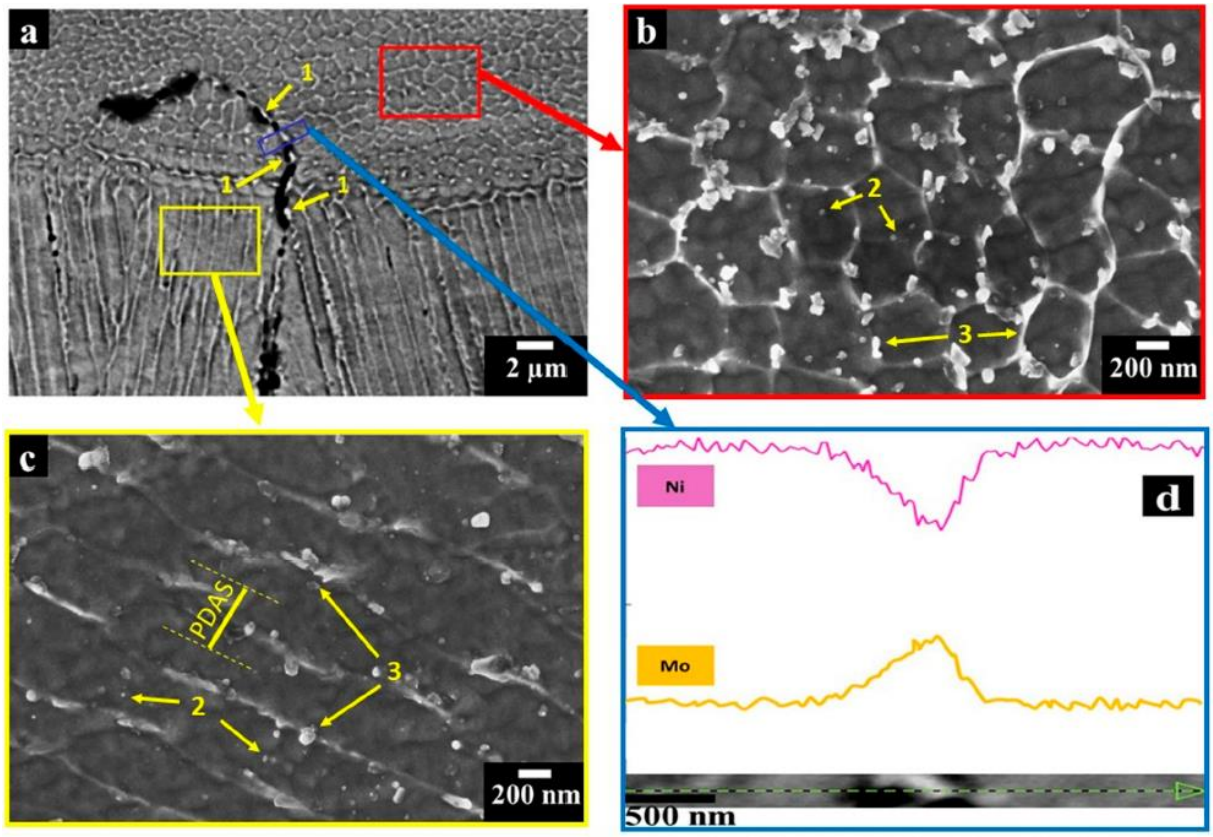

Figure 8: Microstructure of Hastelloy X produced by LPBF [52].

Due to the heterogeneity and anisotropy in LPBF microstructure, heat treatment is performed to tailor desired microstructure and mechanical properties. Ni-based superalloys are prone to precipitation hardening upon heat treatment. Cao et al. reported presence of γ′, 3 variants of γ″ and δ phase in LPBF IN718 after solution annealing followed by 2 step aging [49]. Zhao et al. compared between two different heat treatment schedules in LPBF IN718 [54]. They reported presence of δ phase along with residual Laves phase after heat treating at 980^{o}C. Metallic carbides

also continue to be present in all conditions. However, the carbides provide coherency strengthening to the matrix as opposed to δ and Laves phase composites that cause brittle fracture, therefore, a solution annealing at higher temperature is more suitable to obtain desired mechanical performance. Yang et al. compared stress relieved LPBF Haynes 230 alloy with as-printed counterpart and reported conversion of $M_{23}C_6$ carbides into M_6C carbides after heat treating at 980^{o}C for 1h [48].

1.6 Microstructure and Mechanical Properties of AM Inconel 625 upon Heat Treatment

A substantial amount of research work has been performed to investigate microstructure and mechanical properties of additively manufactured Ni-based superalloys in both as-printed and heat-treated conditions. Several researchers reported fine dendritic microstructure with elemental segregation along interdendritic regions in as-printed LPBF IN625 [18,34,44,55,56]. Fast cooling rate ($\approx 10^6$ K/s) causes local segregation of large Nb and Mo atoms along interdendritic region which facilitates faster precipitation upon heat treatment [20,34,57]. Fig. 9 shows optical and SEM images of XY and XZ planes from as-built and stress-annealed LPBF IN625 [23]. The microstructures appear significantly different on these planes. “Fish-scale” microstructure with U-shaped melt pool contours are visible on XZ plane whereas melt pool tracks created by the laser beam can be observed on XY plane that is perpendicular to build direction. SEM images reveal fine dendritic and cellular substructure as shown in Fig. 9 (c, d). Stress relieving heat treatment at 980°C for 1h does not completely get rid of this fine dendritic microstructure (Fig. 9e-h).

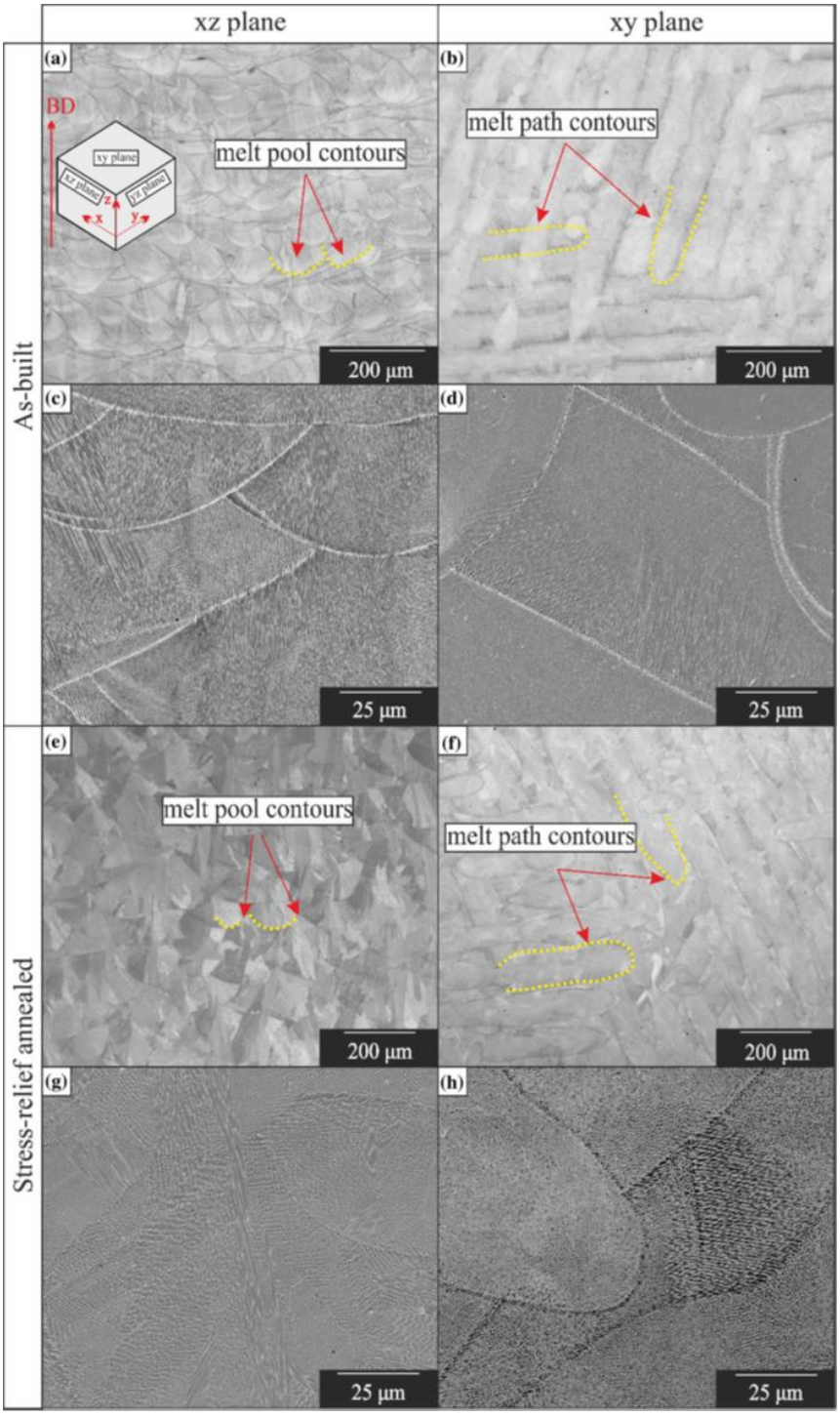

Figure 9: Optical and SEM images of (a-d) as-built IN625, and (e-h) stress-annealed LPBF IN625 [23].

Due to this unique microstructure produced by LPBF method, which is completely different than that in traditionally manufactured material, it is crucial to understand and design

proper heat treatment schedule to tailor desired microstructure and mechanical properties. Typical stress relieving and annealing heat treatments for wrought IN625 are at 870°C for 1 hour and 980°C for 1 hour, respectively [11]. Solution treatment is performed at 1150°C for 2h followed by fast cooling below 540°C to dissolve all second phases and prevent precipitation while cooling [11]. Studies have been performed on effect of multiple stages of heat treatment, which is more of a traditional approach as well as direct aging on microstructure and mechanical properties of LPBF IN625. A significant difference in precipitation behaviours between wrought IN625 and LPBF IN625 was reported by Stoudt et al. [20]. Temperatures and times for δ phase formation in LPBF IN625 compared to wrought IN625 were summarized in their study. It has been observed that formation of δ precipitate occurs significantly faster in LPBF IN625 than in its wrought counterpart. Faster cooling rate and large thermal gradient accompanied by elemental segregation associated with LPBF process cause such reduction in required time to form precipitates [19,20]. Zhang et al. reported finer dendritic microstructure in LPBF IN625 due to faster cooling rate compared to other AM processes like Electron Beam Melting or L-DMD. Interdendritic region in such microstructure is Mo and Ni-enriched, but deficient in Ni and Cr.

Multiple studies have been conducted to on stress relieving heat treatment on LPBF IN625 [19,58], because typical stress relief heat treatment performed on wrought alloys mentioned in earlier paragraph causes precipitation of detrimental δ phase due to elemental segregation found in LPBF microstructure [19]. δ phase as well as carbides were found after stress relieving heat treatment at 870°C for 8 hours. The authors also demonstrated using X-Ray Diffraction (XRD) analysis that a homogenization treatment at 1150°C for 1 hour can dissolve precipitates. Another work of the same group studied feasibility of stress relief heat treatment at a lower temperature to avoid δ precipitation [58]. The study found that heat treatment at 700°C can still precipitate δ

phase, but in smaller amount and size compared to other stress relief heat treatments performed at 800°C or 870°C.

Effect of different routes of heat treatment on LPBF IN625 have also been explored in some studies. Marchese et al. reported microstructure and mechanical properties of LPBF IN625 after direct aging, solution treatment and solutioning followed by aging [44]. γ″ as well as C-rich $M_{23}C_6$ carbides were detected using Transmission Electron Microscopy (TEM) images after direct aging at 700°C for 24 hours. This heat treatment increased strength at the cost of ductility. Solution treatment encouraged grain growth and promoted ductility in the material, however, causing decline in strength. Nb- and Ti-rich MC carbides are found after solutioning. Solutioning followed by aging at 700°C also introduced strengthening γ″ precipitates, but distributed evenly compared to that in directly aged IN625. This heat treatment also increased strength, but decreased ductility. Hardness values measured on each sample condition are shown in Fig. 10. It can be observed that direct aged LPBF IN625 demonstrated much higher hardness compared to solutioned+aged samples.

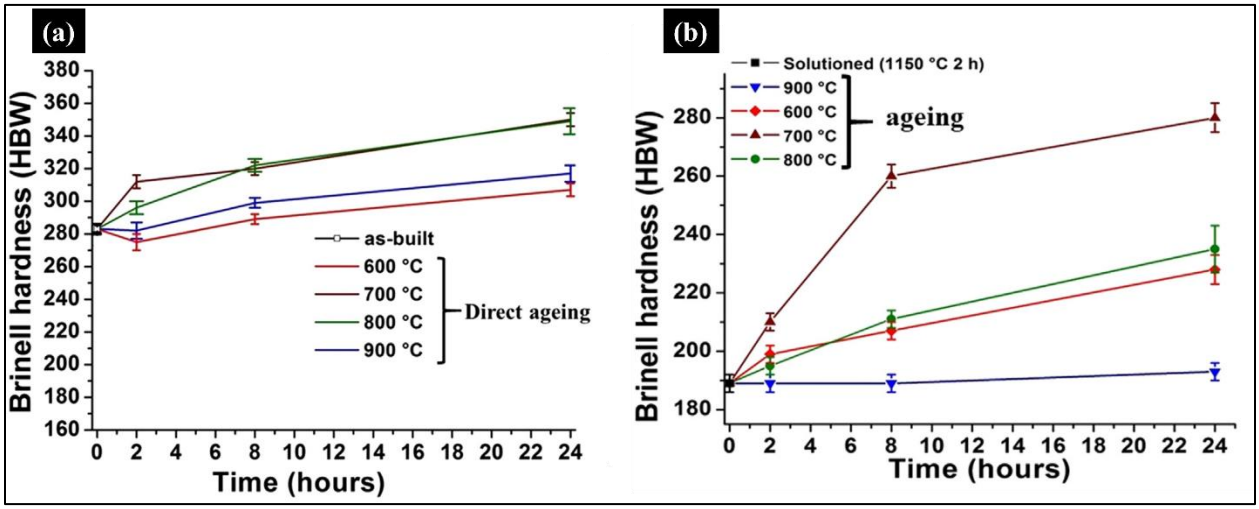

Figure 10: Brinell hardness for LPBF IN625, (a) direct aged, and (b) solution annealed+aged [44].

Same research group also investigated effect of longer heat treatment for up to 200 hours [59]. Precipitation of γ" was detected after prolonged heat treatment at 600°C and 700°C. Heat treatment at 700°C also introduced δ phase. δ phase was formed after heat treatment at 800°C and 900°C as well. Finer δ precipitates in higher amount was found in directly aged IN625 compared to solution annealed followed by aged material. The mechanical properties were more dependent on the heat treatment temperature for solution annealed plus aged IN625 whereas they were similar for directly aged material until 900°C when significant recrystallization takes place. Li et al. reported evolution of microstructure and mechanical properties after stress relief heat treatment as well as heat treatment at 980°C and solutioning at 1150°C of SLM IN625 [18]. As-built IN625 demonstrated high dislocation density, Nb-rich precipitates as well as high tensile residual stress. MC carbides were also observed in XRD analysis after high temperature heat treatment. Another study on SLM IN625 reported no precipitation in as-built state, but formation and growth of carbides after heat treating at 1000°C and 1150°C became evident. The study reported decrease in hardness after heat treating at 700°C, increase in hardness after heat treating at 800°C and 900°C. Hardness decreased again heat treatment at 1000°C due to dissolution of δ precipitate that was found after 800°C and 900°C.

1.7 Motivations and Objectives

This research focuses on the as-printed microstructure of LPBF Inconel 625 as well as effect of various heat treatments on its microstructure, precipitation and mechanical performance. LPBF introduces unique fine dendritic inhomogeneous microstructure with complex residual stress field that affects its mechanical properties. Parts produced with this technique respond differently to heat treatment processes as well compared to wrought making the study inevitable.

Studies have been carried out that investigate microstructural evolution of LPBF Inconel, but still there is lack of information in this field considering AM is still a fairly new technology. Formation of all the phases are not well understood yet and there is not enough comprehensive approaches that observe the heat treated microstructure for a wide range of temperatures and aging times. Due to the nature of the precipitates, sometimes it can be difficult to properly identify them and the results may often come out as ambiguous. Complete TTT diagrams are yet not established for these alloys manufactured using LPBF technology. Traditional heat treatment processes may not be suitable for parts that produced using LPBF or any other AM process. This study focuses on short term direct aging instead of multi-step, long term heat treatment to investigate any possible advantages of the fine dendritic microstructure produced by LPBF. This study also establishes the fact that precipitation occur faster on external surface making the TTT study more crucial.

To carry on the studies discussed in chapter 3, 4 and 5, IN625 samples were printed using a Concept Laser LPBF machine. Then some of the samples were heat treated at 3 different temperatures for various lengths of time. The microstructure and mechanical performance of the as-printed and heat treated LPBF samples were studied using various characterization techniques including electron microscopy and X-ray diffraction. Major precipitates that occur in IN625 were studied in chapter 3. Then microstructure and microhardness evolution from as-printed to heat treated LPBF IN625 was investigated in chapter 4. Finally, an attempt to take a deeper look at the evolution of δ precipitate was made to quantify size and volume fraction of the phase at 900℃ for various times that will facilitate TTT diagram for LPBF IN625.

CHAPTER 2: EXPERIMENTAL DETAILS

2.1 Materials

IN625 cubes of 1 cm × 1 cm × 1 cm are printed using Concept Laser MLab Cusing 100R LPBF machine. The laser is 100W with wavelength of 1070 nm. Build volume of the machine is 90mm × 90mm × 10mm. A thorough parameter study was carried out to determine optimal density which is shown in Fig. 11. Following parameters were chosen after optimal density parameter study to manufacture the parts:

- Laser Power 90 W
- Scan speed 800 mm/s
- Layer thickness 25 μm
- Hatch spacing 60 μm
- Laser Diameter 80 μm

Density of the parts is 99.79% with these parameters for cube no. 14 in Fig. 11. Island scanning approach was adopted to print the parts to reduce residual stress [60]. A schematic of the scanning process is shown in Fig. 12(b). 5mm × 5mm islands were chosen and each layer was shifted by 1mm and rotated by 90°. The printing process was carried out in an argon atmosphere.

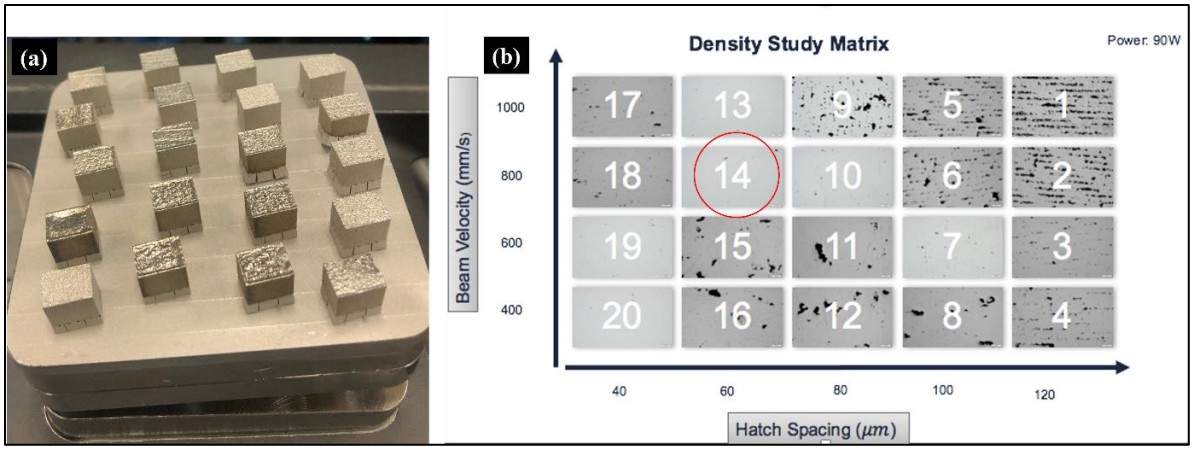

Figure 11: Parameter study for LPBF IN625, (a) samples printed using parameters shown in (b).

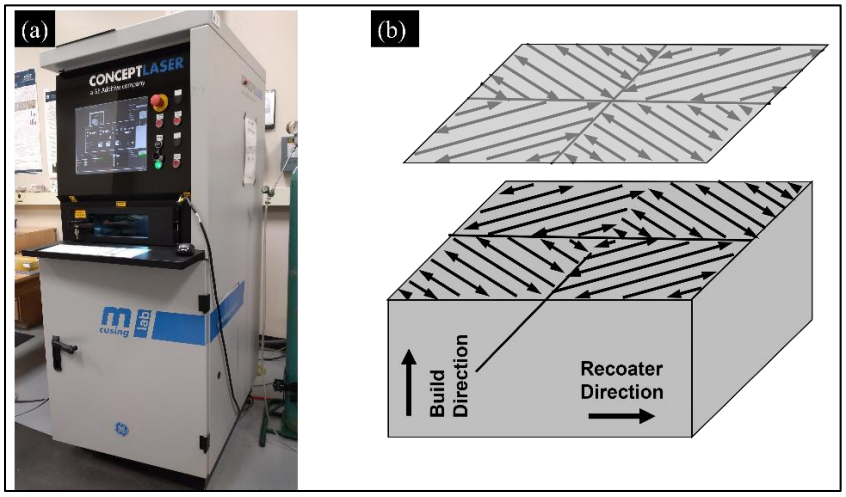

Figure 12: (a) Concept Laser LPBF machine; (b) Island Scanning Pattern.

Wrought IN625 is used to compare microstructure and properties in as-received condition. 10 mm^3 cube was sectioned from a 5 mm thick plate (Metalmen, NY, USA) of AMS5599 specification using wire electrical discharge machining (EDM).

Compositions of both IN625 powder and wrought IN625 are given in table 2.

Table 2: Composition of IN625

% wt.	Ni	Cr	Mo	Fe	Nb+Ta	Co	C	P	S	Al	Ti	Mn
LPBF	Bal	21	9	<5.0	3.5	<1.0	< 0.1	<0.015	<0.015	<0.4	<0.4	<0.5

Wrought	Bal	22.36	9.0	4.72	3.32	0.8	0.035	0.009	0.005	0.08	0.3	0.18

2.2 Heat Treatment

Heat treatment was performed on some of the cubes using a TreetAll box furnace. Direct aging at 700ºC, 900ºC and 1050ºC for 2, 5 and 10h for each temperature was adopted for this study. Additional heat treatment at 900℃ for 1h and 40h was also performed to support study of δ precipitate in detail in chapter 5. A K-type thermocouple was used to monitor the temperature.

These combinations of time and temperature were chosen based on TTT diagram of LPBF IN625 shown in Fig. 13. As mentioned in earlier chapter, precipitation occurs faster in LPBF IN625 compared to in wrought material as shown in Fig. 6 [20]. At 900ºC, δ phase takes about 40 hours to form in wrought IN625 whereas it takes less than an hour to form in IN625 manufactured using LPBF. Microstructure produced by LPBF method consists of fine dendrites with elemental segregation on interdendritic regions which may facilitate faster precipitation [19,20]. 700℃ was chosen to encourage precipitation of γ″ phase and 1050℃ was chosen to ensure dissolution of secondary phases and complete recrystallization according to established research on IN625 [12,13].

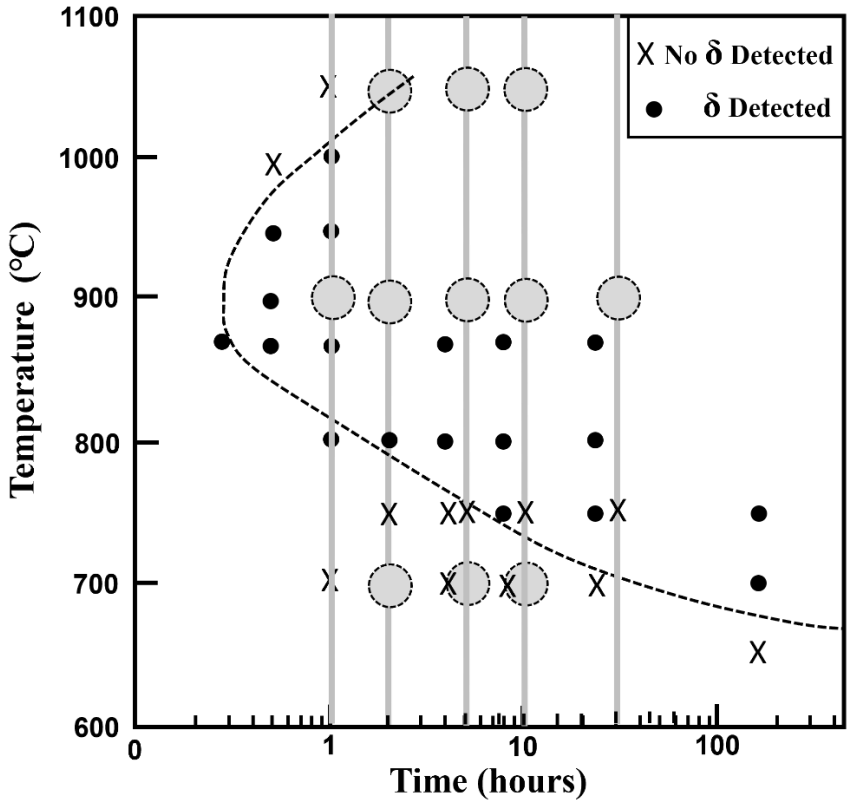

Figure 13: TTT diagram for δ phase in LPBF IN625 (adapted from [20])

Samples are designed as "heat treatment temperature_time". Names of all the samples are shown in table 3.

Table 3: Heat Treatment parameters for LPBF IN625 samples

Sample	Heat Treatment Temperature (ºC)	Time (hours)	Cooling Method
AP	As-printed (No HT)	N/A	N/A
700_2h	700	2	Air Cooled
700_5h	700	5	Air Cooled

700_10h	700	10	Air Cooled
900_1h	900	1	Air Cooled
900_2h	900	2	Air Cooled
900_5h	900	5	Air Cooled
900_10h	900	10	Air Cooled
900_40h	900	40	Air Cooled
1050_2h	1050	2	Air Cooled
1050_5h	1050	5	Air Cooled
1050_10h	1050	10	Air Cooled

2.3 Metallographic Sample Preparation

2.3.1 Sectioning

To study effect of heat treatment on microstructure, LPBF and wrought cubes of IN625 were sectioned parallel to the build direction using Buehler IsoMet 2000 precision saw to reveal internal surface at 3600 rpm speed and 400 grams load.

2.3.2 Mounting

To facilitate revealing internal microstructure using electron microscopy, samples were hot mounted using Struers mounting press. CONDUCTOMOUNT^{TM} mounting resin was used as the mounting material at 20 kN force.

2.3.3 Grinding and Polishing

Mounted samples were ground and polished using Struers automatic polisher. Samples were first ground with 220 grit SiC pad followed by polishing with 9μm and 3μm diamond polishing suspensions. A final polishing was performed using 0.25μm colloidal silica suspension. Any alumina suspension was avoided to eliminate confusion with the Al-oxide present in the alloy. Vibratory polishing for 2-3 hours was performed using 0.04μm colloidal silica for EBSD analysis. All polished samples were cleaned using ultrasonicator with water and alconox powder. A final rinsing step with acetone was performed as well.

2.3.4 Etching

To reveal microstructure and precipitates, samples were electro-etched with 70% phosphoric acid at 3-5 volts for 5-40 seconds.

2.4 Characterization Techniques

2.4.1 Scanning Electron Microscopy (SEM)

A JEOL 7000F field emission SEM unit is used to take high magnification images of the microstructure of the samples. 20kV accelerating voltage, 8 probe current and 10mm working distance are usually used for secondary electron imaging. Backscatter electron images were also at the same parameters to reveal grains and precipitates.

EDS line scans were performed on certain areas of the microstructures to reveal composition of those areas.

EBSD analysis was performed on vibratory polished surfaces to reveal texture and grain information. Scanning area was chosen at a magnification that ensures capturing around 10,000 grains before post-processing the data. The scanning was performed using 20kV accelerating voltage, 16 probe current, and 15mm working distance. A scanning step size of 2μm was used

considering the grain size. MTex tool of MATLAB program was used to post-process experimental data.

2.4.2 Transmission Electron Microscopy

TEM analysis was carried out on AP, 700_2h and 900_2h to confirm and identify γ″ and δ precipitates using a FEI Tecnai F20 (scanning) transmission electron microscope ((S)TEM) operated at 200kV by conventional bright field and selected area electron diffraction (SAED) techniques. Samples for TEM examination were extracted and thinned to electron transparency using standard focused ion beam (FIB) lift-out techniques using a Tescan Lyra dual FIB – scanning electron microscopy (SEM) unit [61]. ImageJ software was used to invert contrast of some SAED patterns to get a clearer visual of the diffraction spots.

2.4.3 X-Ray Diffraction

X-ray diffraction of every specimen is performed after heat treatment and sectioning. A Bruker D8 Diffractometer with a copper X-ray source is used. Bragg-Brentano beam geometry is used with a working voltage of 40 kV and a current of 40 mA. Fast full range scan was performed from 20°-100° using 0.02° increment and 0.2 sec/step scanning speed. Local slow scan was performed to reveal δ phase in the range of 45°-48° using 0.02° increment and 4 sec/step scan speed. Cukα_2 peaks were attenuated from all XRD pattern using Bruker EVA software.

2.4.4 Vickers Hardness

Vickers hardness is also measured before and after heat treatment on a Leco DM-400 hardness tester with an applied load of 1000 gf (1 kgf = 9.8 N) for 30 seconds. Measurements were performed after sectioning and polishing the hot mounted samples.

CHAPTER 3: IDENTIFICATION AND EVOLUTION OF MAJOR PRECIPITATES IN LPBF IN625 UPON RELEVANT THERMAL TREATMENT

Microstructure of LPBF as-printed and heat treated IN625 has been studied by multiple researchers, however, a more detail and comprehensive look at each precipitate that confirms and identifies types of them is still essential to understand the evolution of microstructure for various applications. Traditionally manufactured materials have widely been studied for different applications, but the same post-processing techniques may not be suitable for AM produced parts. Evolution of each precipitate was studied for various heat treatment temperatures, but same amount of time. As-printed LPBF IN625 samples were heat treated in the range of 700°C to encourage formation of strengthening γ″ phase, 900°C to facilitate formation of stable δ phase that is formed from γ″ phase and 1050°C to dissolve all precipitates and dendritic structure leading to complete recrystallization. Each heat treatment temperature was hoeld for 2 hours and done separately on individual samples. The microstructure was observed using scanning electron microscopy imaging as well as electron backscatter diffraction. Each precipitate has been separately investigated with the help of several characterization techniques such transmission electron microscopy (EBSD) and energy dispersive spectroscopy (EDS). X-ray Diffraction (XRD) was performed to calculate lattice parameter of γ matrix as an indicator of formation of secondary phases. Microhardness was measured for all samples using Vickers indenter and was explained using the microstructure observations and precipitation behavior. Metastable γ″ phase was detected in as-printed condition as well as at 700°C. Different variants of the phase were identified as well. Detrimental δ phase was also found at 700°C and confirmed using TEM. This phase was observed at 900°C as well. Other than major phases γ″ and δ, presence of carbides and Al_2O_3 is reported in all conditions that has not been mentioned widely in literature to author's best knowledge.

3.1 General Microstructure

Fig. 14 presents SEM micrographs of the general microstructure of LPBF as-printed and heat treated IN625. Microstructure of each LPBF sample was acquired on the surface normal to sweep direction after etching. “U” shaped melt pools are clearly visible in as-printed LPBF IN625 as shown in Fig. 14(a). This shape is caused by Gaussian energy distribution of the laser beam interaction with the alloy [34,62]. The width of these melt pools approximately range between 100-120 μm, as their exact width is obscured by their overlapping. This enables high part density with no gap between the melt pool boundaries [17,34]. At higher magnification, Fig. 14(b), it can be observed that the microstructure actually composed of networks of solidified and elongated dendrites of in different directions, widely reported by other researchers [16,18,34,55,56]. Here, the cross-section of neighboring dendrite networks of different orientation are observed. This can be interpreted as group of dendrites growing in different directions and the cross-sections of certain groups appear as cellular structure or network. The width of the dendrites is about 500 nm. Researchers have reported chemical segregation of larger metallic atoms, namely Nb and Mo, in interdendritic regions [63,64]. Apart from laser-related dendritic microstructure, columnar grain growth along build direction can progress through several LPBF layers, as shown in Fig. 14(a). This morphology indicates re-melting of layers and continued grain growth in a preferred direction upon subsequent passes of the high energy laser beam [62,65].

Melt pools boundaries are still visible after heat treating at 700^{o}C for 2h with dendrtic structure (Fig. 14c, d). The microstructure is fairly similar to as-printed microstructure. Remnants of melt pools can be seen in the 900_2h sample, Fig. 14(e). Here, some regions have recrystallized, and precipitates grow along melt pool and dendritic boundaries at this temperature as can be seen from high magnification image in Fig. 14(f). These precipitates will be identified and discussed in

detail in later sections. Columnar growth can no longer be observed at 900℃. Melt pool boundaries, major precipitates, dendritic structure with elemental segregation are completely dissolved in 1050_2h sample (Fig. 14g, h). Microstructure of this sample consists of equiaxed grains with some annealing twins that indicates residual stress release [18,44]. Some irregular, blocky shaped precipitates can be observed in the matrix and on grain boundaries that will be identified and discussed in later sections. This microstructure is comparable to wrought microstructure that will be discussed in detail in chapter 4.

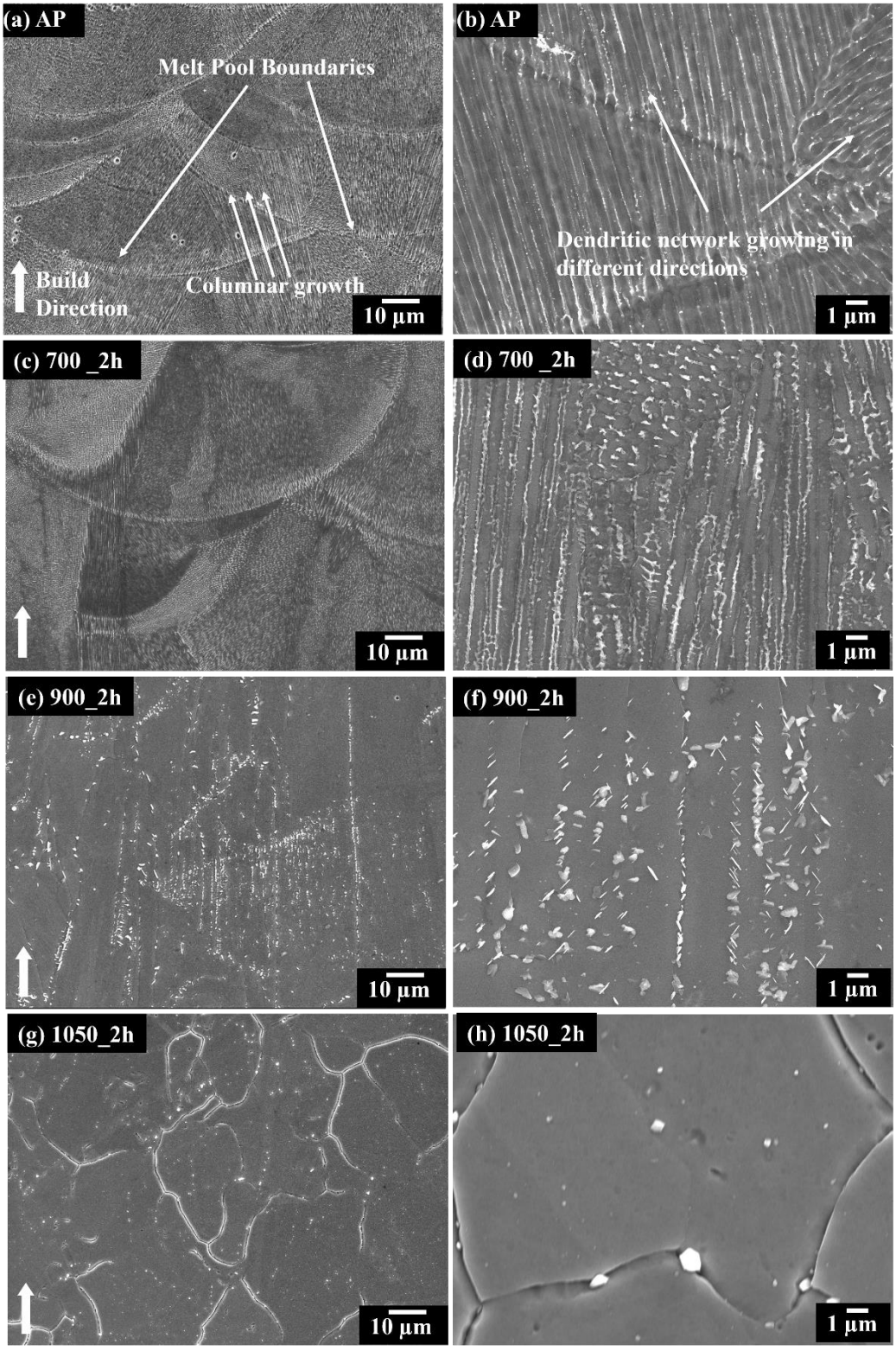

Figure 14: SEM images of microstructure of LPBF IN625; (a, b) as-printed, (c, d) heat treated at 700℃ for 2h, (e, f) heat treated for 900℃ for 2h, and (g, h) heat treated at 1050℃ for 2h.

Figs. 15, 16 and 17 reveal the evolution of texture in LPBF samples compared to wrought IN625. Inverse pole figures (IPF) are shown in Figs. 15 and 14. Fig. 16 is a comparison of one IPF from all samples, the IPF point of view is the plane that was scanned which is perpendicular to sweep direction. Fig. 17 shows example from one sample (700_2h) where all 3 IPFs are shown. Although IPF-BD and IPF-TD do not represent the grains on those respective planes since they were not actually scanned, however, the Euler shading provides idea on the grain orientations from those points of view. IPFs in Fig. 15 show that there are large, elongated grains growing roughly along build direction as well as a reasonable number of very small grains that are ≤ 30 μm in AP, 700_2h and 900_2h samples. These observations are in agreement with the findings from other researchers for IN625 [18,59]. Li et al. suggested that the sizes of the smaller grains are induced by the remelting near the melt pool boundaries and epitaxial growth of the grains. Although the heat treatment up to 900℃ does not cause any major change in grain growth, the texture appears to get stronger along (100) plane with increasing heat treatment temperature as can be observed from pole figures (PF) presented in Fig. 16. Multiple Uniform Density (MUD) values in PFs are kept in the same range to facilitate visual comparison between different planes as well as for different samples. The average grain size of the AP sample is 40.4±16.8 μm that increases up to 52.1±19.7 μm after heat treating at 900℃ as shown in Fig. 18. Detrimental δ phase is expected to form at somewhat at 700 and profusely at 900℃ [13,17,28,36,38]. Therefore, the increase in grain size can be attributed to the strain produced by δ phase formation, which will be discussed later. A noticeable change is observed in the 1050_2h sample where the grains become equiaxed with random texture as shown in Figs. 15(d) and 15(d). The grain size is here is actually reduced to 20.43 ± 9.26 μm at this temperature. Although precipitates, elemental segregation, melt pool boundaries and dendritic structure are dissolved at this temperature, the counteracting effect of

stress release may cause this reduction in grain size. The sudden drop in grain size at 1050°C can also be explained by Fig. 19. Kernel average misorientation plots for all LPBF samples are shown in Fig. 19. It can be observed that there is a dominance of misorientations inside the grain for AP, 700_2h and 900_2h samples since there are groups of dendrites that are slightly misoriented with each other. With heat treatment at 1050°C, those groups of dendrites make their own grains causing the larger grains breaking apart into smaller grains and almost complete recrystallization.

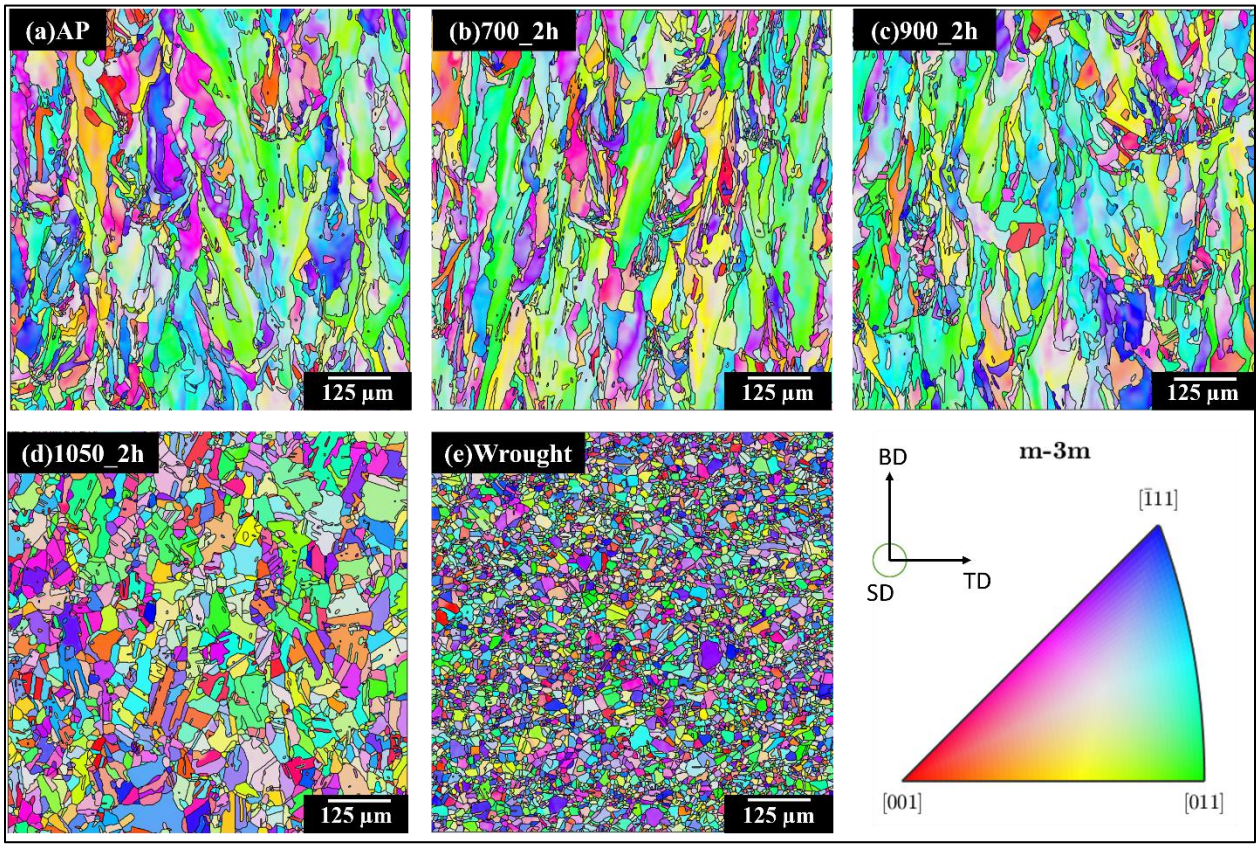

Figure 15: (a-d) Inverse Pole Figure (IPF) maps of as-printed and heat treated LPBF IN625 compared to (e) wrought IN625.

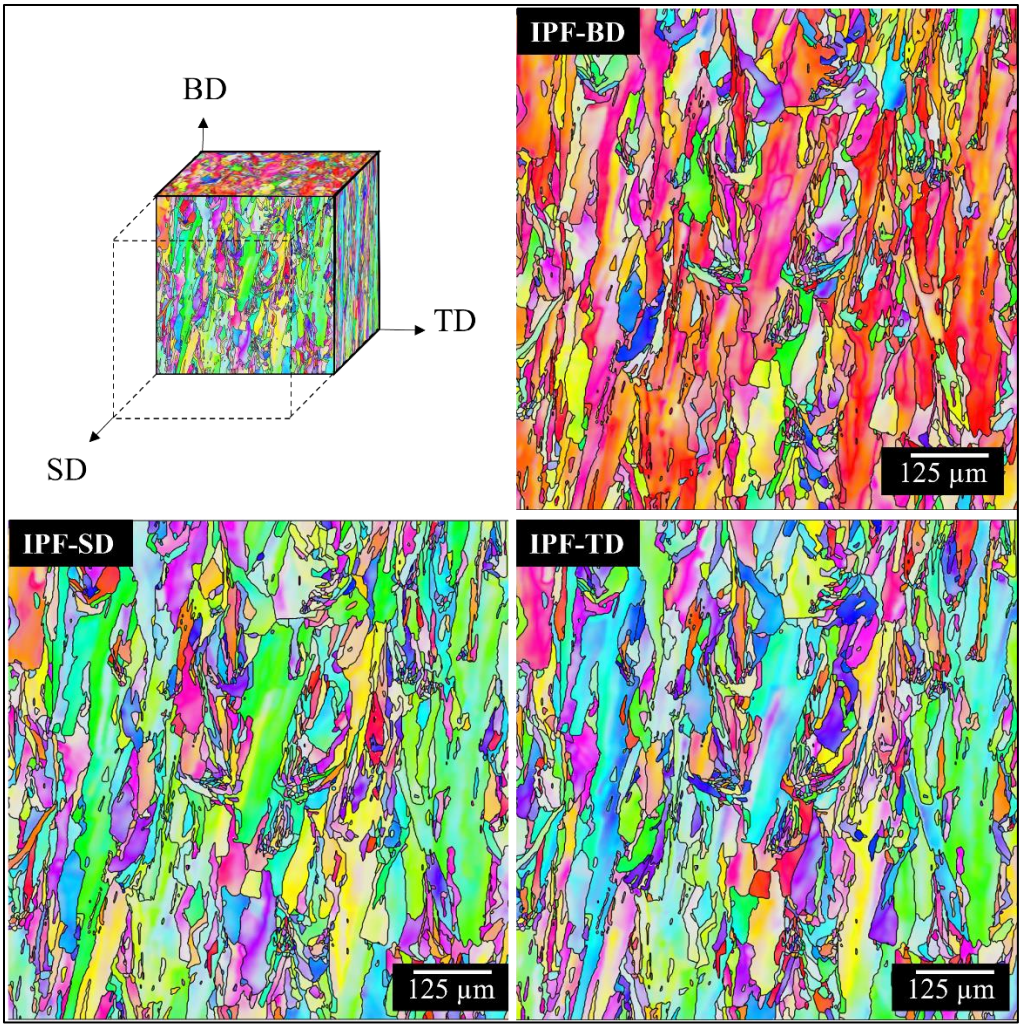

Figure 16: IPFs of all 3 points of view from 700_2h LPBF sample.

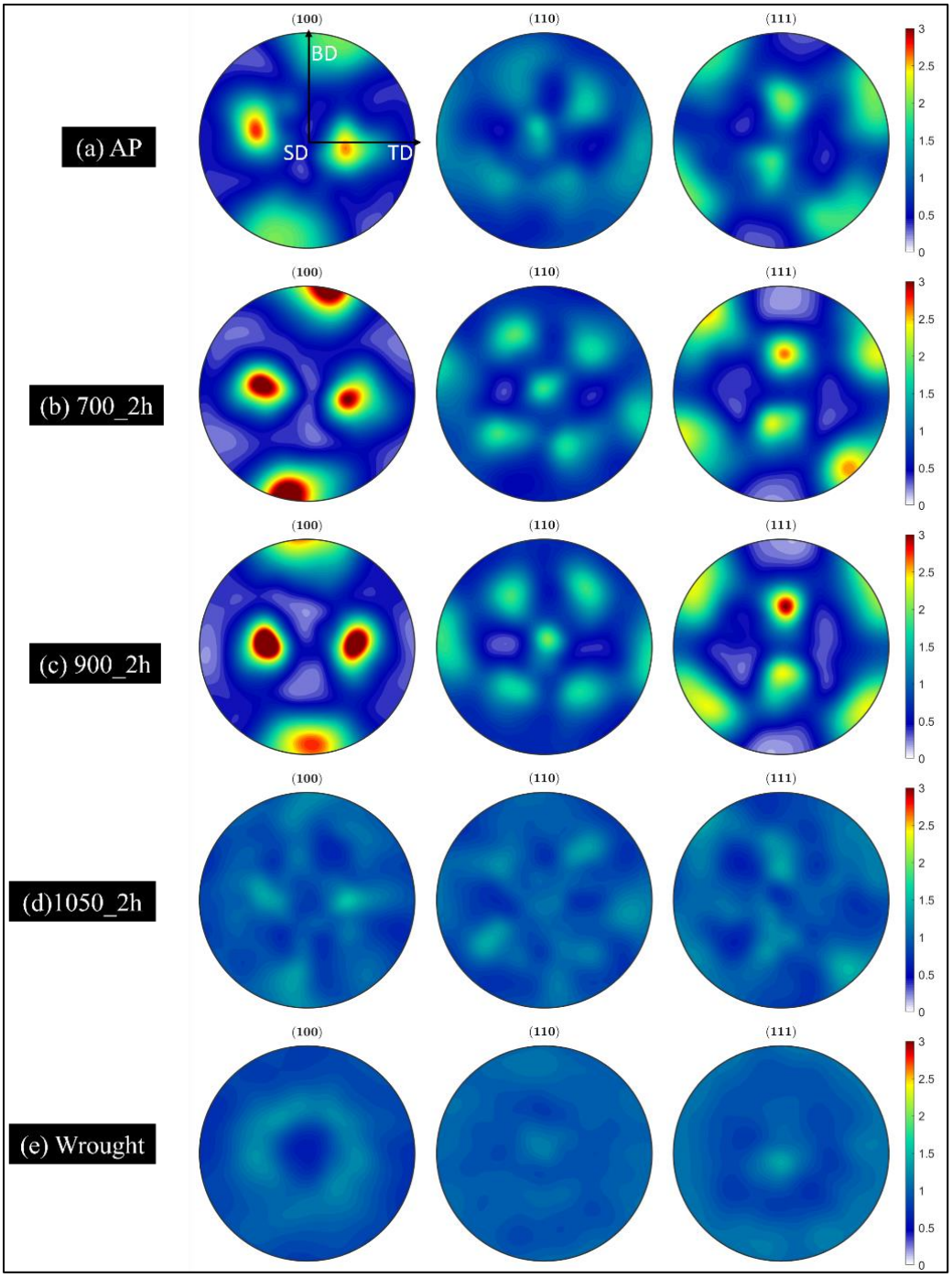

Figure 17: Pole Figures (PF) of as-printed and heat treated LPBF IN625 compared to wrought IN625.

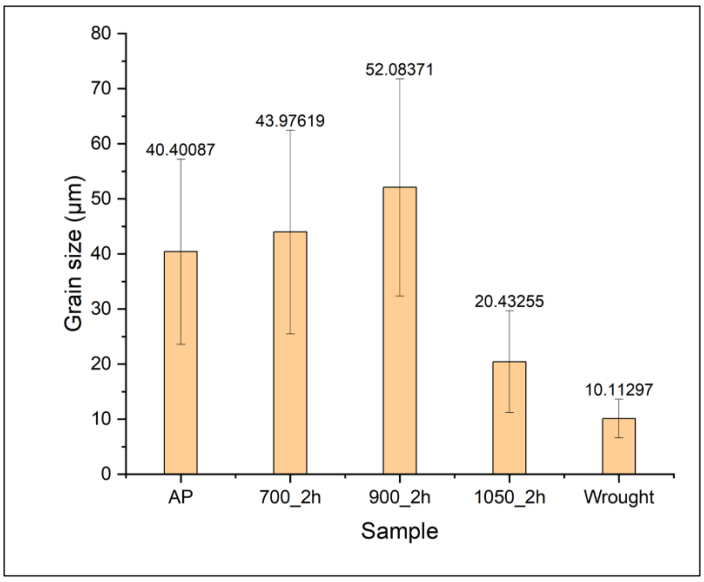

Figure 18: Grain size evolution in LPBF IN625 heat treated at different temperatures

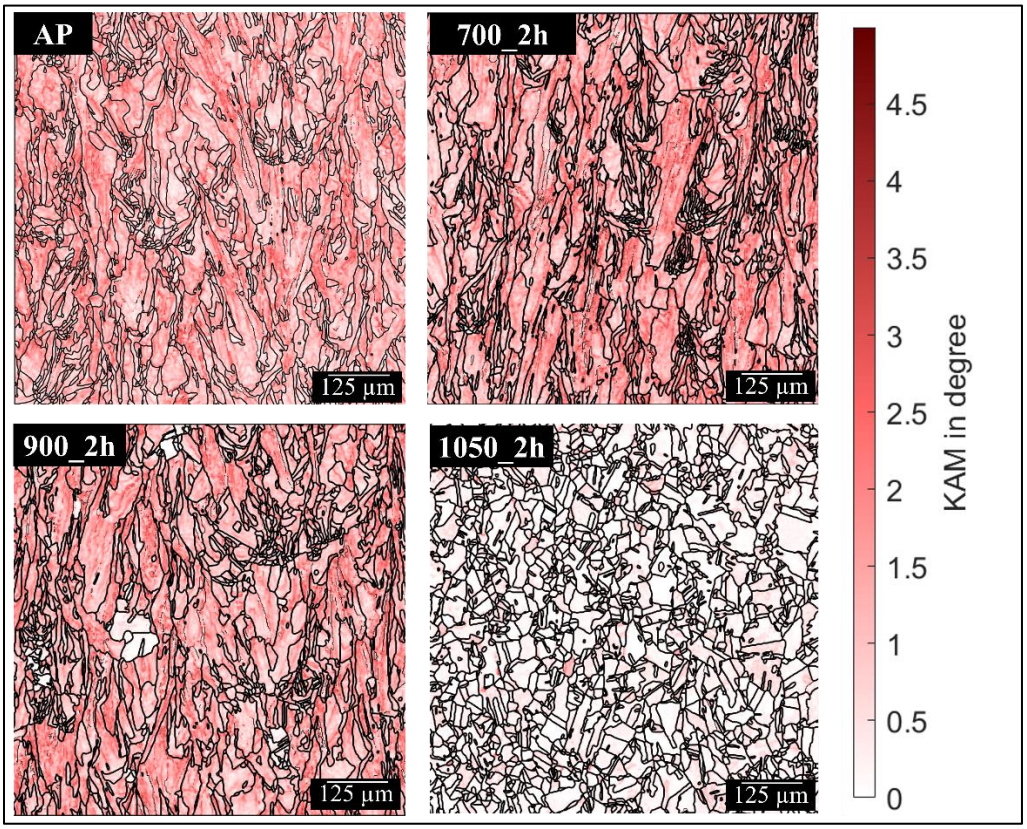

Figure 19: Kernel Average Misorientation for LPBF IN625samples

X-ray diffraction analysis was performed on these specimens to identify existing phases as shown in Fig. 20. Peaks for γ matrix can be identified in all conditions, but any other phase cannot

be detected for 2h heat treatment which is not uncommon if the amount of precipitation is not enough or the particles are too small [15, 17, 20]. Moreover, peaks of γ″ overlap with γ matrix peaks making it even more difficult to identify and separate [20].

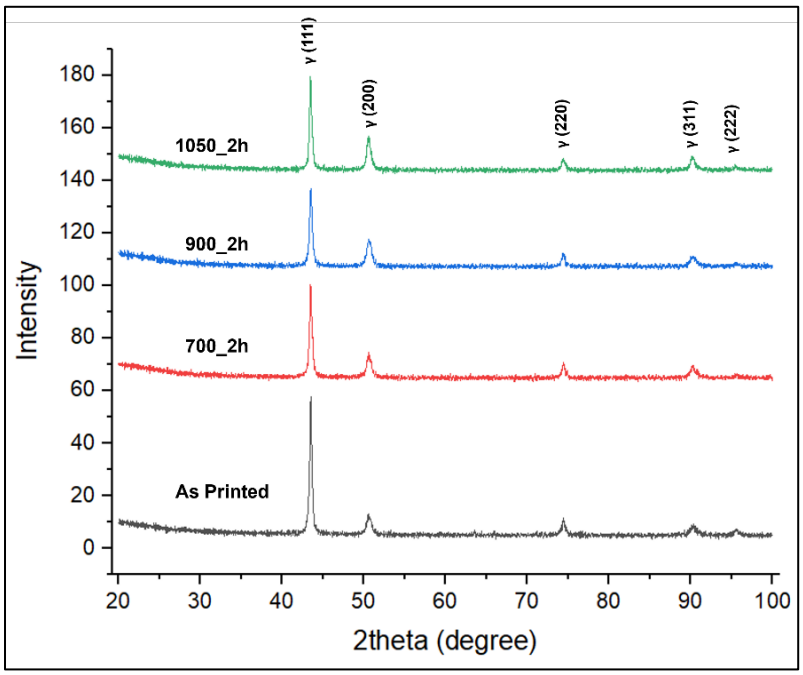

Figure 20: XRD pattern for LPBF IN625

Since XRD is not enough to identify phases present, other characterization techniques such as energy dispersive spectroscopy (EDS) and transmission electron microscopy (TEM) are required. The phases that were identified and discussed in upcoming sections are summarized in table 4.

Table 4: Precipitates identified in LPBF IN625

Phases	**AP**	**700_2h**	**900_2h**	**1050_2h**
γ”	Matrix	Matrix	--	--
δ	--	Matrix	Matrix & GB	--
Carbides	Matrix	Matrix	Matrix & GB	Matrix & GB

Al_2O_3	Matrix	Matrix	Matrix & δ precipitates	Matrix

3.2 γ″ Precipitate

The γ″ precipitate was only observed in the as-printed (AP) and 700°C sample sets. Fig. 21 shows bright field TEM micrographs with selected area diffraction patterns (SAED) from the as-printed and 700_2h conditions. For the AP condition, the bright field images (a) show disc-shaped precipitates on the order of 3 to 10 nm and SAED pattern indicated these consisted of γ″ phase. The γ″ precipitate phase is the main strengthening precipitate that is found in a number of Ni-based superalloys [25,49,66–68]. It has a body centered tetragonal crystal structure that is coherent with the FCC γ matrix. The strengthening they impart results from coherency strain hardening. These precipitates have an ellipsoidal disc shape that is induced by the lattice misfit with γ matrix. The [001] axis or c-axis of tetragonal γ″ precipitate is longer than the c-axis of FCC γ matrix, causing a large misfit strain that encourages the disc-like shape of the γ″ precipitate [25,69]. The orientation relationship between the two phases is described as [32,37]:

$$(100)\gamma'' \parallel \{100\}\gamma$$

$$[001]\ \gamma'' \parallel \langle 100\rangle\gamma.$$

There are only 3 possible variants of γ″ precipitate that grow from {100} planes of γ matrix. In the AP sample, only the [100]γ″ (indicated by blue circles) and [010]γ″ (indicated by green circles) variants are visible in the SAED pattern, Fig. 21(b), while the [001]γ″ variant is missing. According to Oblak et al., the [001]γ″ variant can be suppressed upon direct aging under compressive stress [25]. In case of LPBF fabrication, it can be linked to the ultrafast cooling rate and directional solidification [17].

After heat treating at 700°C for 2 hours, there is little change in the size of the γ″ precipitates, Fig. 21(c). Also, the missing [001]γ″ (indicated by orange circles) variant appeared in the SAED pattern, as shown in Fig. 19(d). This is due to the release of the tensile residual stress that had developed from LPBF processing. The tensile stress in AP IN625 was measured to be 77±15 MPa, reported in prior work by the authors [70]. Direct aging under tensile residual stress mimicked the effect of stress aging under tensile load which promoted the growth of [001]γ″ variant [25,32,69,71]. The size of the other two variants is unchanged since stress aging under tensile load suppresses growth of [100]γ″ and [010]γ″ compared to [001]γ″ [25].

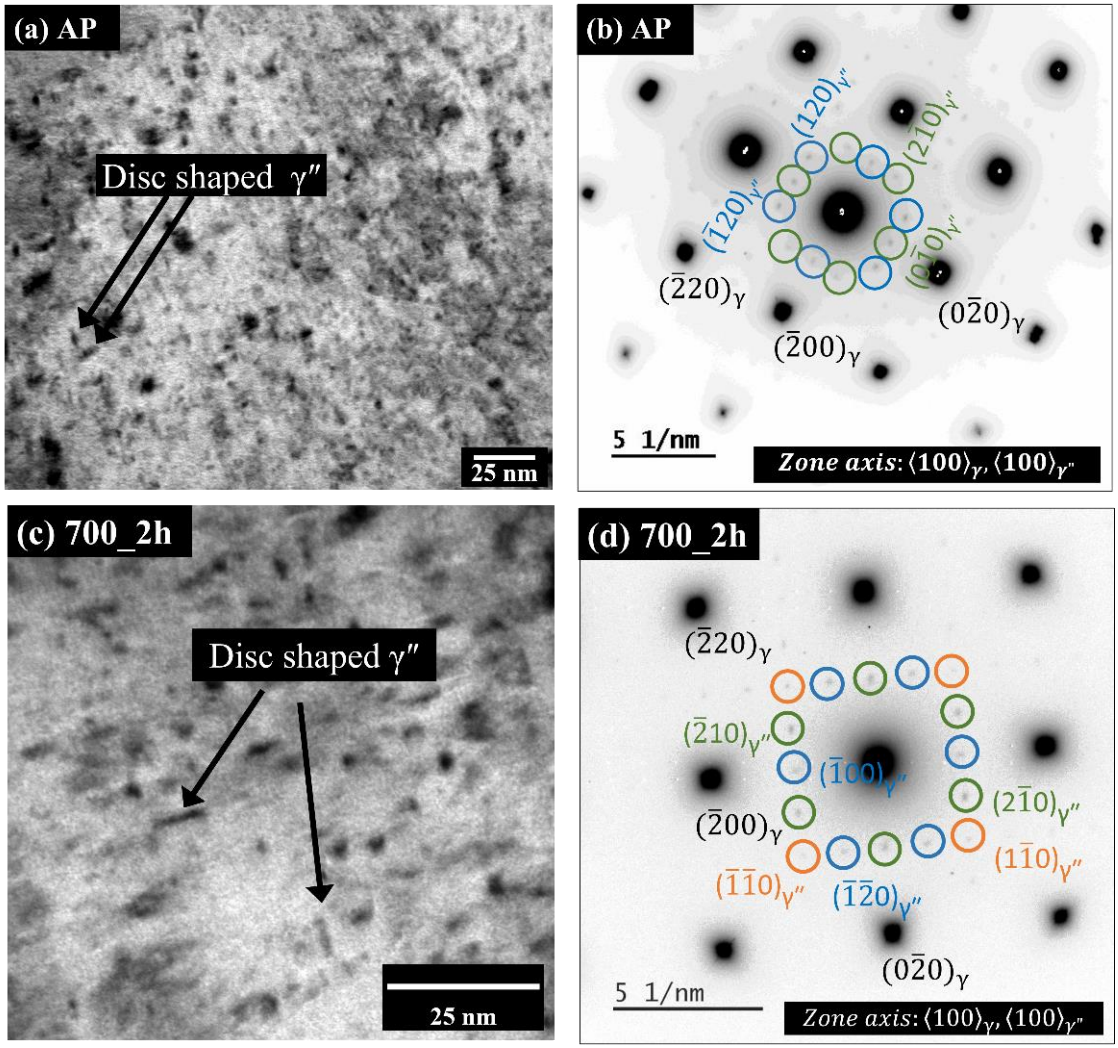

Figure 21: TEM micrographs from (a) AP and (c) 700_2h sample; SAED patterns from (b)AP and (d) 700_2h samples showing presence of γ″ precipitate.

3.3 δ Precipitate

The δ phase precipitate was only observed in the 700°C and 900°C sample sets. Fig. 22(a) shows a bright field image of the 700_2h sample where 20-100 nm long, needle shaped precipitates can be observed. The SAED pattern shown in Fig. 22(b) confirms these precipitates are δ phase. Here, the orientation along <110>γ zone axis confirms the presence of at least 2 δ phase variants (δ1 and δ2) as oriented with the matrix γ phase habit plane (111)γ. The variants are orientedapproximately 70° angle with respect to each other. Similar findings were reported by

other researchers for traditional Inconel alloys where two variants of δ precipitates were found that can be defined as “orientation twins” or “antiphase domain structures” [72,73]. The orientation relationship of the δ phase precipitates with γ matrix is [9,37]:

$$(010)\delta \parallel \{111\}\gamma$$

$$[100]\delta \parallel \langle 110\rangle\gamma.$$

When slight rotating the sample the precipitates disappear, which indicates that they are actually plate-shaped and not needle-shaped. Although the heat treatment temperature is in the range that favors formation of δ precipitate in IN625. To the best knowledge of the author, it has not been reported with proof before for LPBF IN625 for temperature as low as 700°C and treatment time as low as 2 hours. The δ precipitate is actually formed from metastable γ″ phase [13] which is already present in the as-printed and 700_2h conditions. Thus, the presence of γ″ precipitate likely facilitated the early formation of the δ phase.

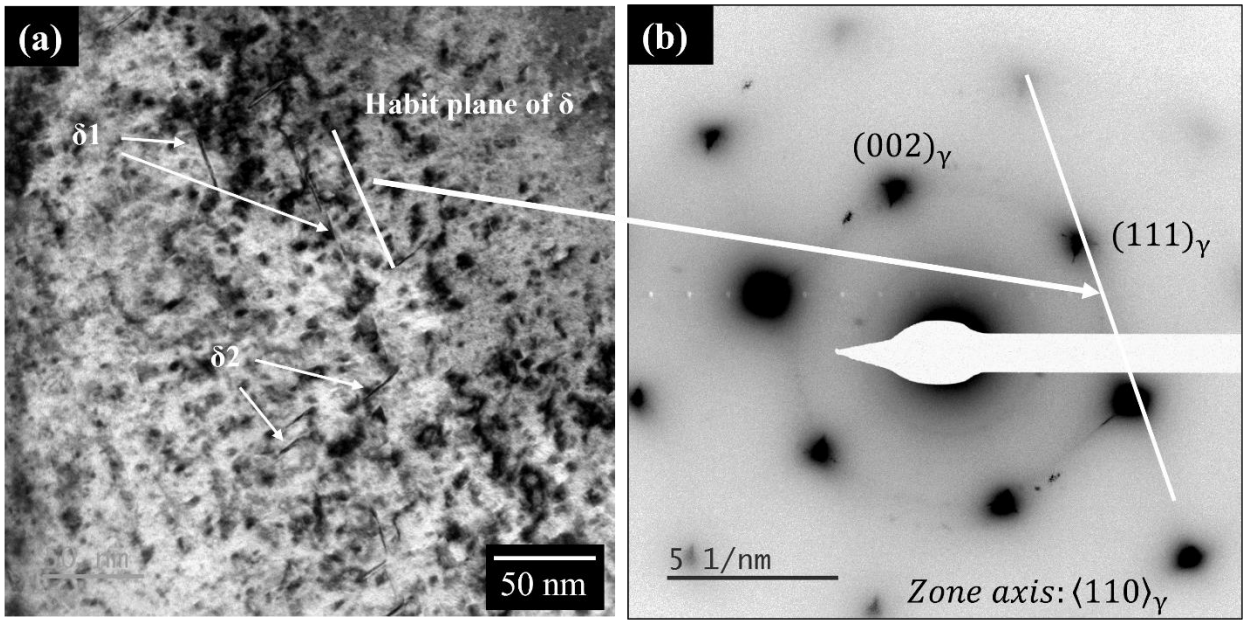

Figure 22: (a) TEM image inside a grain in 700_2h sample; (b) SAED pattern from (a) indicating presence of δ

Fig. 23 shows TEM images and electron diffraction patterns of the δ precipitate in 900_2h condition. An overall view of the sample is shown in fig. 23(a) where needle-like and plate-shaped precipitates can be observed both within grains and at grain boundaries (GB). The size of these precipitates ranges from few hundred nm to over 1 μm depending on their location. Thick plate-shaped precipitates on grain boundaries were identified as δ phase by SAED pattern as shown in Fig. 23(b) and (c). The smaller precipitates within the grains are also identified as δ precipitates as shown in Fig. 24. Therefore, the precipitates are actually 2 dimensional plate shaped forms that are rotated at a certain angle giving 1 dimensional appearance. One such precipitate is shown in Fig. 24(a). The high resolution TEM (HRTEM) images are presented in Fig. 24(b) and (c). Here, the coherency between δ precipitate and γ matrix can be observed. Three areas in the HRTEMs were chosen to perform Fast Fourier transform (FFT) simulations, defined as 1 and 2 in Fig. 24(b) and 3 in Fig. 24(c). In area 1, the majority of the area contains only the γ matrix as identified from the simulation. Area 2 also primarily covers the γ matrix. However the FFT simulation reveals is the presence of a stacking likely caused by formation of the δ precipitate. Area 3 includes both part of the precipitate as well as γ matrix. Here, the FFT simulation presented in Fig. 24(d) confirms it as a δ precipitate within the grain. The precipitates grew much larger at 900℃ compared from those at 700℃, whereas, δ precipitates formed on the grain boundary appear to be significantly larger.

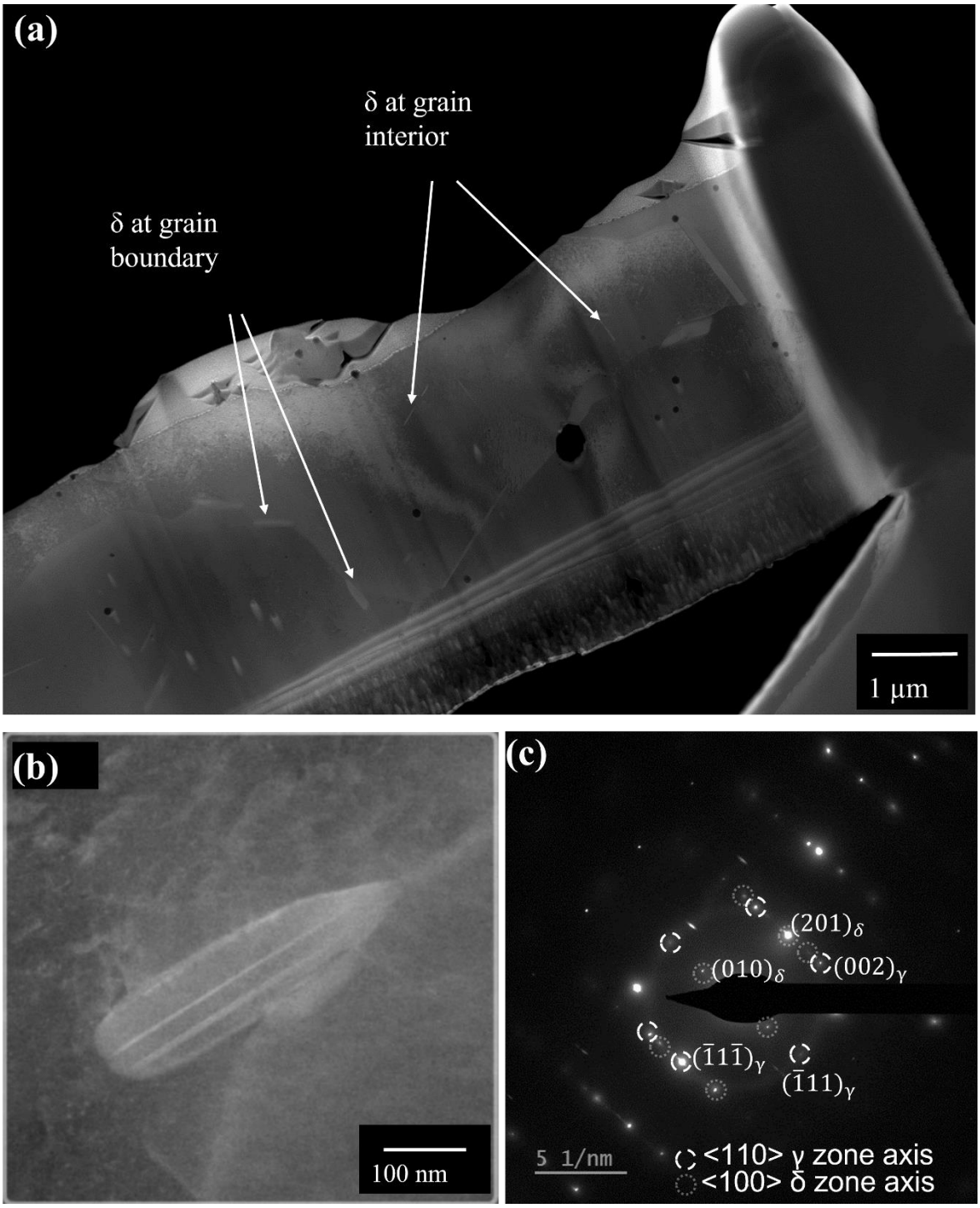

Figure 23: (a)TEM thin film taken from 900_2h sample; (b) bright field TEM image of a δ precipitate on GB and (c) corresponding SAED pattern; (d) bright field TEM image of a δ precipitate inside grain.

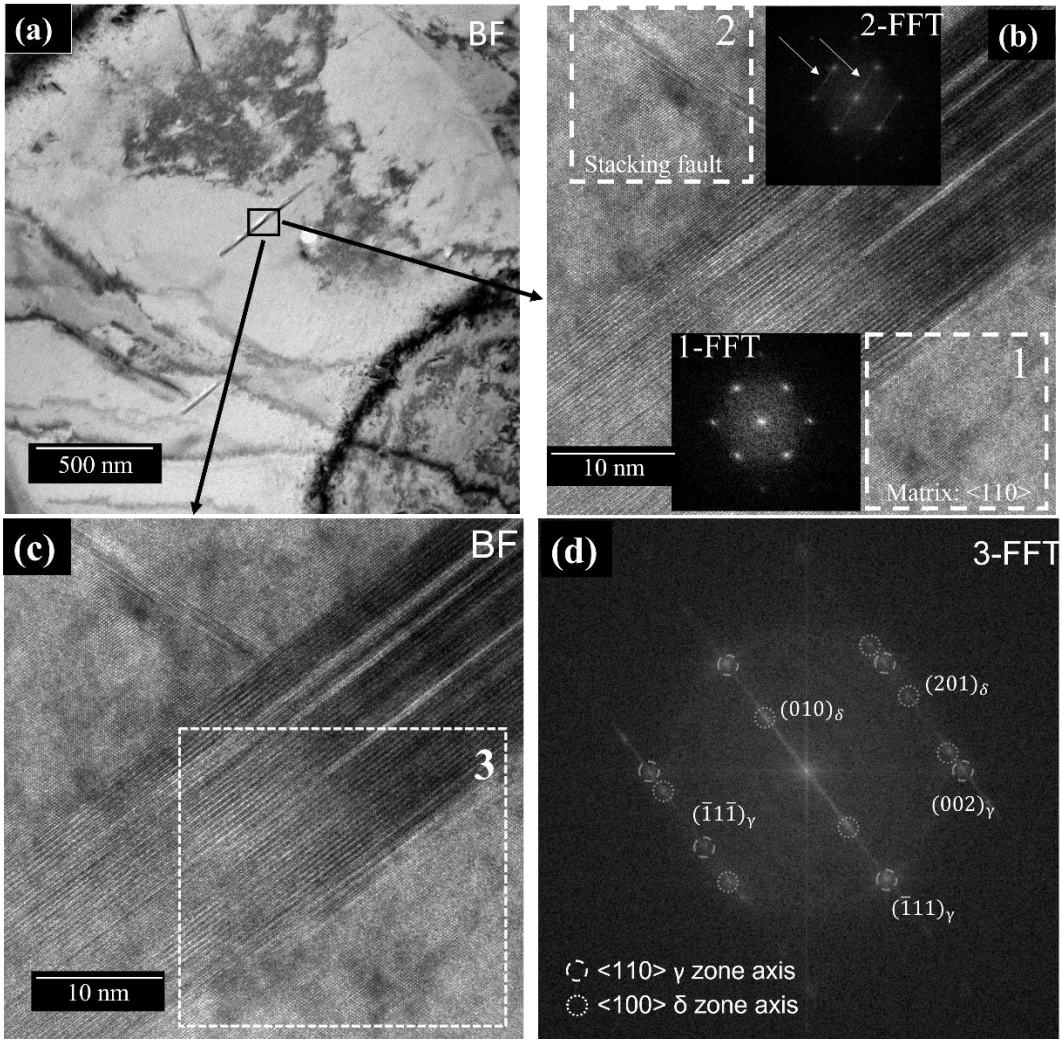

Figure 24: (a) δ precipitate in matrix, (b) HRTEM image of the δ precipitate with FFT showing γ matrix and stacking fault; (c) HRTEM image of δ precipitate with (d) FFT pattern of the area 3 indexed for δ precipitate.

3.4 Carbides

Carbides are another precipitate typically observed in alloy IN625. In this work they were observed in all LPBF samples as shown in Fig. 25. Energy dispersive spectroscopy (EDS) analysis was performed on each sample to confirm the presence of carbides. Clusters of irregular shaped carbides were observed in locations where two melt pool boundaries meet in AP IN625 (Fig. 25a). The deficiency of Ni and Cr, coupled with Nb and Mo enrichment in the particles indicate presence of (Nb, Mo)C. The irregular morphology, formation during solidification and in their

interdendritic location also point toward formation of MC [11,13,44]. The formation of carbides is generally facilitated by Nb and Mo segregation in the interdendritic region due to fast cooling rate [44]. The accurate size of the carbides is challenging to measure since they can be overlapped with the elemental segregation. Marchese et al. [44] reported presence of nanometric sized Nb-rich MC near interdendritic region of as-built LPBF IN625. Liu et al. [43] observed circular $M_{23}C_6$ precipitation in as-built IN625 produced via selective laser melting (SLM) as well as laser engineered net shaping (LENS) in intergranular region.

At the 700°C treatment, similar carbides are also found on the grain boundaries as shown in Fig. 25(b) and corresponding EDS pattern. These carbides are also rich in Nb and Mo and deficient in Ni and Cr. Their irregular shapes indicate that they are most likely the primary MC carbides that formed during printing. The treatment temperature is also not high enough for these carbides to evolve or to form any other type of carbide. $M_{23}C_6$ has been shown form at similiar temperatures; however, they are usually rather rich in Cr [11,13,22].

Block-shaped carbides are observed in evanescent interdendritic regions of 900_2h sample, as shown in Fig. 25(c). Considering the treatment temperature and their composition as measured by EDS, they appear to be the already formed primary MC carbide that grew after aging. The carbides are around 770 nm. However, some significantly smaller carbides on the order of 300 nm can also be observed in the matrix. These carbides are likely secondary carbides and are developed in the form of MC and M_6C at this temperature [13,22]. The presence of 9% Mo in the alloy composition also facilitates formation of Mo-rich M_6C [11].

Carbides can be found in both intergranular as well as intragranular locations in 1050_2h sample, see Fig. 25(d). Larger carbides are mostly residing on GBs with a size of 380-970 nm. Smaller carbides can be found on both GBs as well as grain interiors with size range of 160-305

nm. Also, a few large carbides of size approximately 600-700 nm can be found inside grains [17]. The larger carbides are primary MC carbides that grew upon aging. The smaller carbides may have been transformed from primary carbides in the form of either MC or M_6C. Presence of carbides around this temperature have widely been reported for both traditional and AM IN625 [11,13,18,21,34].

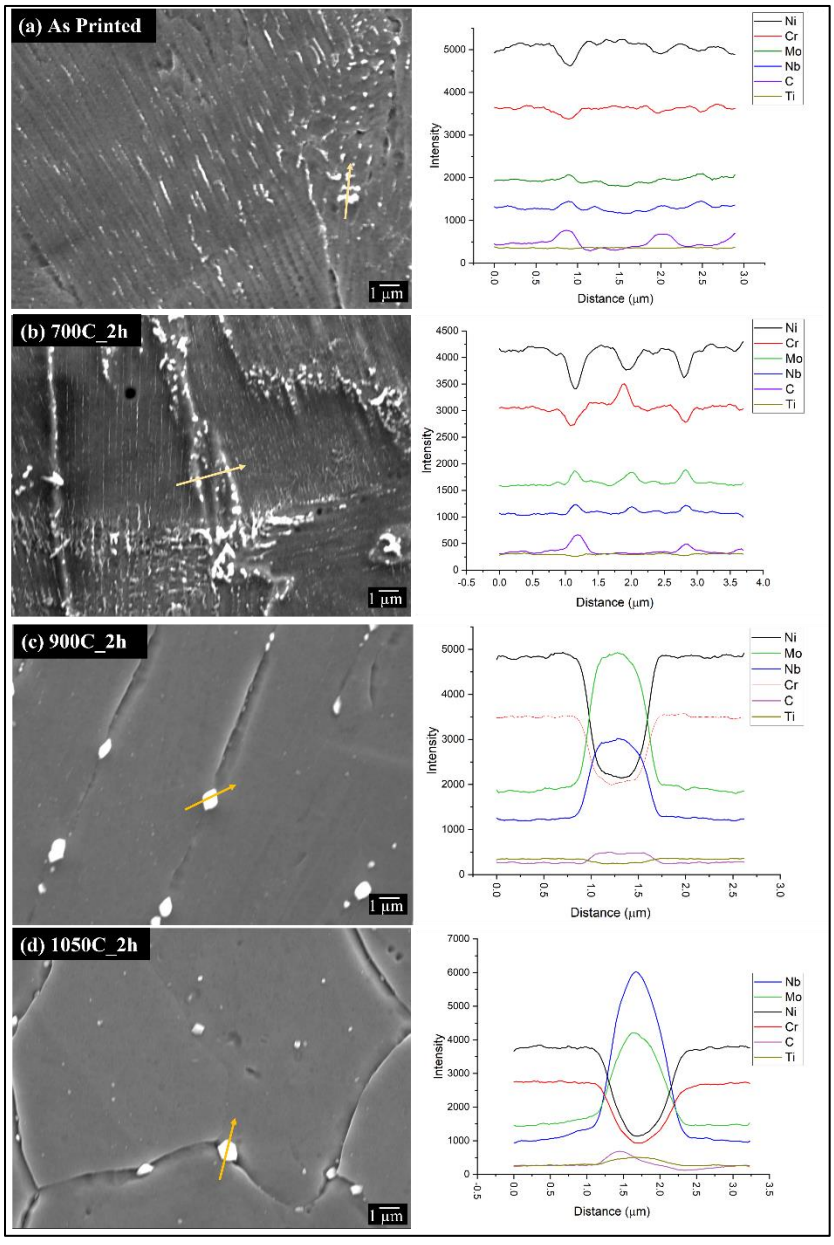

Figure 25: Carbides with corresponding EDS patterns in (a)AP; (b)700_2h; (c) 900_2h and (d)1050_2h samples.

3.5 Al-oxide Inclusions

Al_2O_3 particles were found in all LPBF samples in this work. Fig. 26(a) represents a TEM BF image of the AP sample along with its corresponding EDS spectrum of the precipitate, indicated by arrow. It is clear from the EDS analysis that the particle is rich in Al and O. The size of the precipitates is approximately 35-95 nm. They are observed everywhere in the sample, including at the GBs as well as grain interiors. The presence of metallic oxide inclusions in as-printed LPBF IN625 have been well described by Staroń et al [23]. According to literature, oxide inclusions are likely caused by presence of oxygen in powder as well as in the build chamber environment [18,23,24].

The observed oxides showed little change with heat treatment. Fig. 26(b) shows a TEM backscatter electron image (BSE) of the 700_2h sample. These oxides also appear evenly dispersed throughout the sample with a similar size distribution as the AP sample. Increasing the treatment temperature to 900°C, Fig. 26(c), show little change to the existing Al_2O_3 precipitates, with perhaps a slight coarsening as the larger precipitates are on the order of 105 nm. As described above, this temperature corresponds to the significant formation of the δ precipitate phase. An interesting observation is the emergence of new, small Al_2O_3 ppts adjacent to the δ precipitates as shown in Fig. 27. Based on their location, it can be inferred that some of these Al-rich oxides may have formed during the conversion of existing γ″ precipitates, which contain Al, into Al-free δ precipitates. After treatment to 1050°C, Al_2O_3 particles continue to be observed throughout the sample, see Fig. 26(d). These precipitates have evolved in size to increase the upper range to approximately160 nm in diameter, similar to that observed by others [18,23,24].

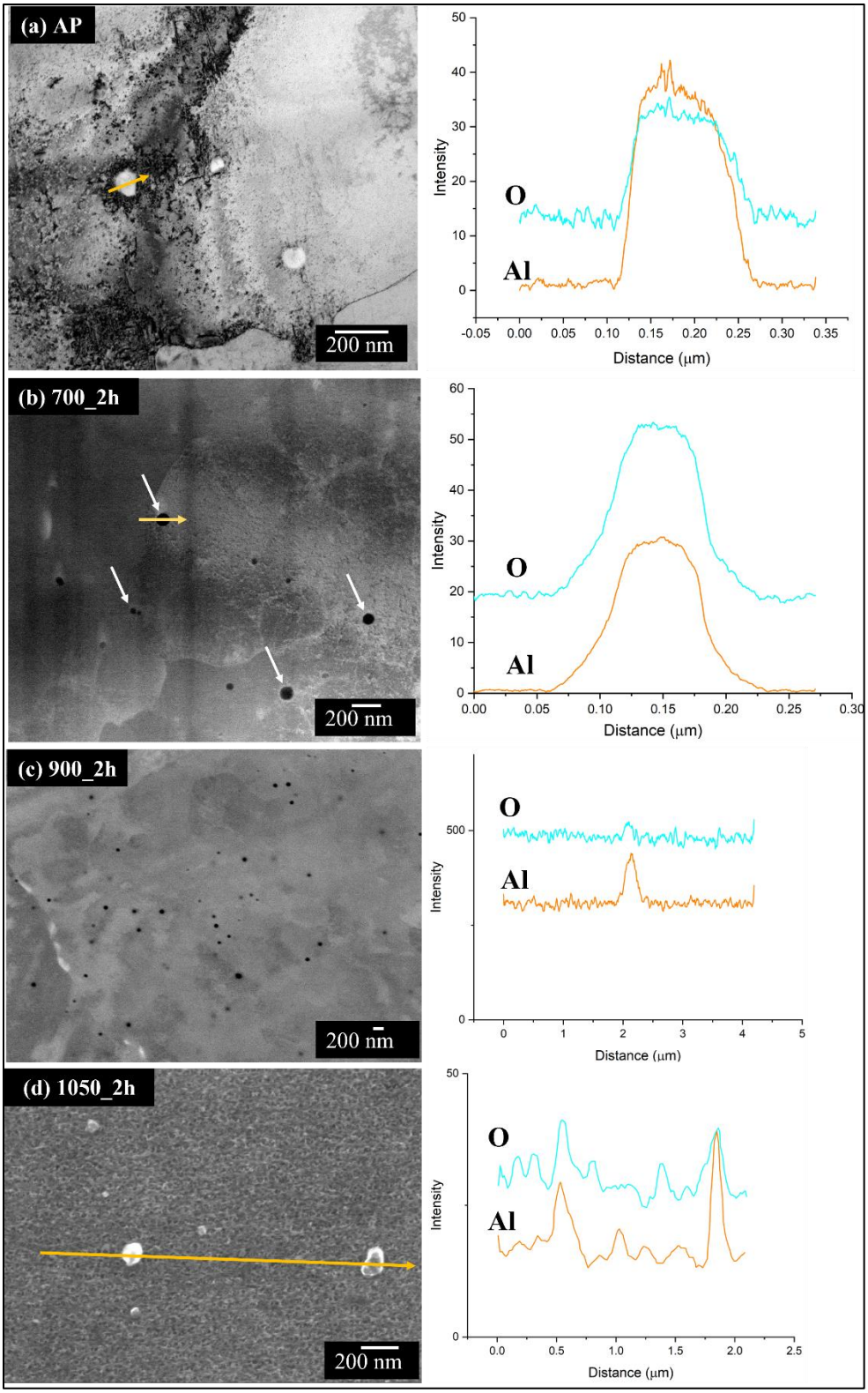

Figure 26: Al_2O_3 particles with EDS spectra in (a) TEM BF image from AP; (b) TEM BSE image from 700_2h; (c) SEM BSE image from 900_2h; and (d) SEM image from 1050_2h sample.

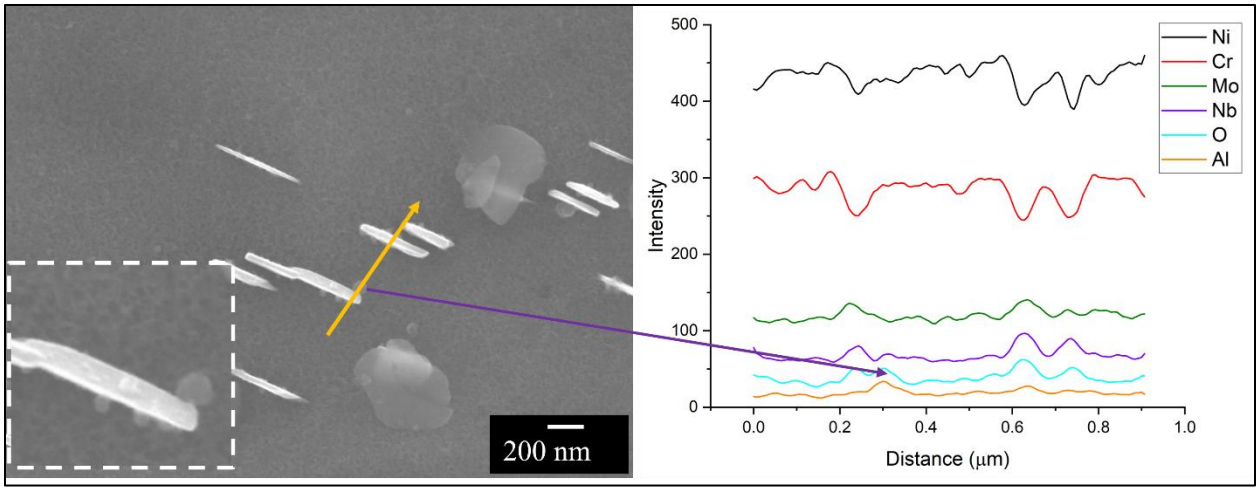

Figure 27: Al-oxide particles near δ precipitate.

3.6 X-Ray Diffraction Analysis

Change in lattice parameter is another way to indirectly prove formation of precipitates [20, 21, 35]. Lattice parameters from each peak for 2h hour samples in Fig. 20 are calculated using following equations:

$$2d_{hkl}sin\theta = n\lambda \quad \text{..... (1)}$$

$$d_{hkl} = a/\sqrt{h^2 + k^2 + l^2} \quad \text{.....(2)}$$

where, d is plane distance, n is diffraction order (usually 1), λ is Cukα wavelength (3.5406 Å) and a is lattice parameter. Then the corrected lattice parameter is calculated using Nelson-Riley function.

$$\text{Nelson-Riley function} = \frac{1}{2}\left(\frac{cos\theta^2}{sin\theta} + \frac{cos\theta^2}{\theta}\right) \quad \text{.....(3)}$$

Lattice parameter values are plotted against Nelson-Riley function as shown in an example in Fig. 28. The corrected lattice parameter is the value for which Nelson-Riley function is zero. The calculated values are summarized in table 5 and plotted in Fig. 29. The error bar in Fig. 29 represents deviation of the corrected value from the lattice parameters from each peak.

For 2h heat treatment, lattice parameter decreases from AP to 700℃ due to formation and growth of γ″ phase. Bigger Nb atoms exit from the matrix to form γ″ making the lattice parameter of γ matrix smaller. Then it increases at 900℃ due to some recrystallization as well as strain introduced to the matrix by the δ phase formation. For 1050℃-2h, the lattice parameter increases further due to dissolution of precipitates, elemental segregation, and dendritic structure into the matrix.

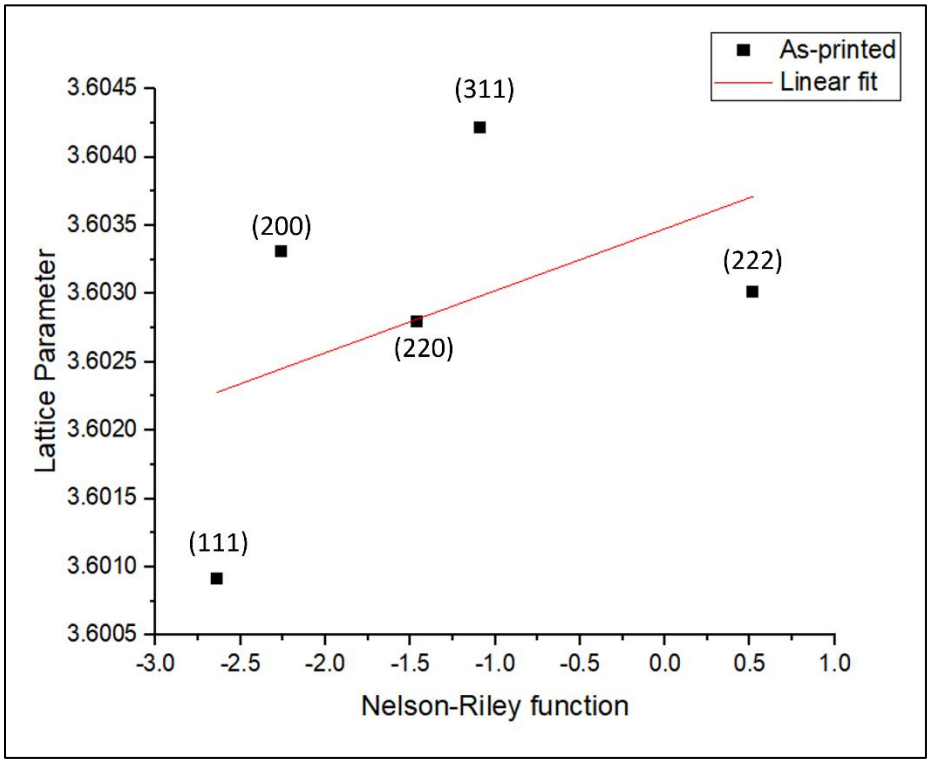

Figure 28: Example calculation of corrected lattice parameter using N-R function

Table 5: Lattice Parameter of γ matrix in LPBF IN625

Sample	(111)	(200)	(220)	(311)	(222)
AP	3.600917	3.603307	3.602792	3.60421	3.603014
700C_2h	3.600809	3.604128	3.60284	3.604494	3.602037

900C_2h	3.599905	3.601515	3.603823	3.604422	3.602372
1050C_2h	3.602457	3.605635	3.603652	3.605898	3.604611

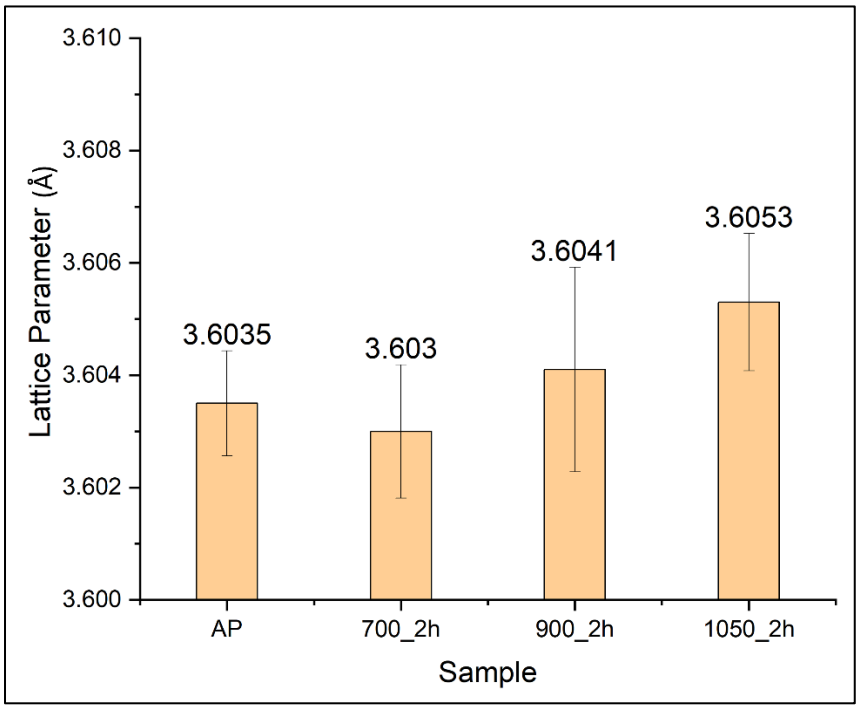

Figure 29: Evolution of lattice parameter with increasing heat treatment temperature

3.7 Hardness

The variations in microstructure and precipitates with direct ageing in this work has shown a significant change in microhardness behavior. Fig. 30 shows the evolution of microhardness with heat treatment of LPBF IN625 at increasing temperature compared to a wrought IN625 counterpart prepared by aerospace material specification AMS 5599. The hardness of AP IN625 is 341.5 ± 6.06 $HV_{1.0}$ was the highest measured of all samples and significantly higher as compared to the wrought sample of 223.25 ± 2.86 $HV_{1.0}$. This high hardness is not only attributed to the fine dendritic microstructure resulting from LPBF's ultra-fast cooling rate and elemental segregation as described in the literature, but also due in part to the unexpected formation of the γ″

strengthening phase. Hardness then reduces somewhat to 324.75±4.49 $HV_{1.0}$ after heat treating at 700℃ for 2h. Here, additional γ″ precipitates formed and grew with heat treatment. In addition, formation of a modest amount of δ precipitate was observed upon dissolution of some γ″. Despite the formation of additional precipitates, that hardness reduction is attributed to the slight increase in grain size, as shown in Fig. 18. The hardness further decreased upon heat treatment at 900℃. Although the δ phase has formed on a wide scale, it generally formed from dissolution of the existing γ″ strengthening precipitates. Although it does participate in part as a strengthening mechanisms it was accompanied by a significant increase in grain size that dominated hardness behavior. The lowest hardness values were achieved in the 1050°C heat treatment where the hardness reduced to 222.5±5.17 $HV_{1.0}$, nearly equivalent to hardness of wrought IN625. The hardness at this temperature decreased despite significant reduction in grain size. This is attributed to the dissolution of major precipitates, dendritic structure and stress release through recrystallization and grain growth of an equiaxed microstructure. Although the hardness is very similar between the 1050°C and wrought samples, the average grain size of the wrought samples is approximately half that of the 1050°C samples. This indicates that directly solution annealing LPBF samples generates microstructures that retain some aspects of their as printed forms, such as precipitates, which results in higher hardness.

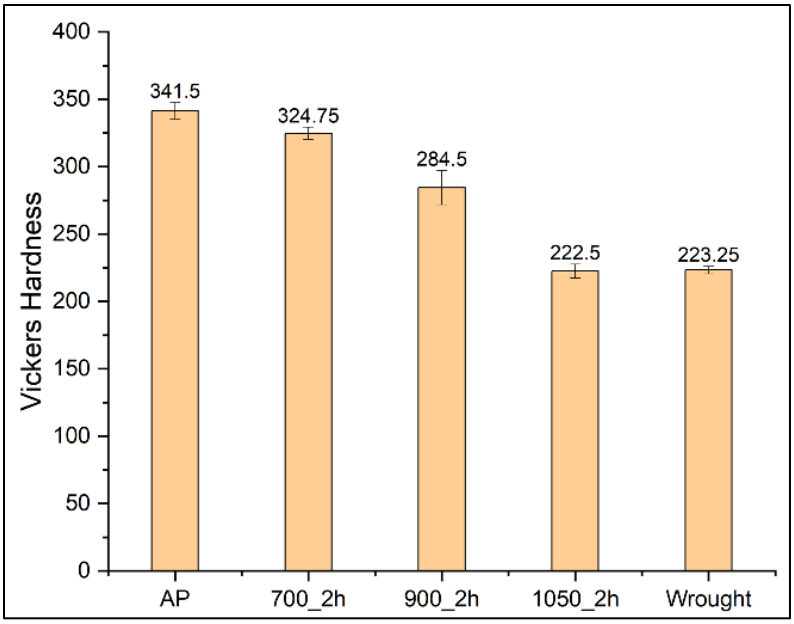

Figure 30: Change in hardness of from as-printed to heat treated LPBF IN625

3.8 Conclusion of Chapter 3

Microstructure of LPBF IN625 with evolution of each precipitate upon heat treatment has been discussed in this study. Strengthening γ″ phase, detrimental δ phase, carbides and aluminum oxide particles were found at different conditions. The findings can be summarized as follows:

- Melt pool boundaries along with dendritic microstructure growing in different directions were observed on the plane normal to sweep direction in as-printed LPBF IN625. The microstructure stayed fairly similar at 700°C. Partial recrystallization took place at 900°C with disappearing melt pool boundaries. Microstructure was almost fully recrystallized with dissolved dendritic structure and precipitates at 1050°C.
- Large elongated grains growing along build direction were observed in as-printed, 700°C and 900°C state of LPBF IN625. Texture became stronger along (100) plane with increasing heat treatment temperature until it becomes random and weak at 1050°C. The microstructure of

LPBF IN625 at 1050℃ is similar to wrought IN625; however, the grain size is still fairly larger compared to that in wrought condition.

- Metastable γ″ precipitates form during manufacturing stage causing higher hardness in as-printed LPBF IN625. 2 out of 3 variants of the precipitate were detected in TEM SAED pattern. The 3rd variant appeared at 700℃ which is caused by direct aging of AP IN625 that contained tensile residual stress along build direction.
- Stable δ phase formed at 700℃ upon dissolution of some γ″ precipitates causing lower hardness compared to AP. 2 variants of δ precipitate were observed at 700℃ which grew upon heat treatment at 900℃. Formation and growth of δ precipitate caused stacking fault in the primary γ matrix. The hardness kept decreasing at 900℃ as well due to recrystallization and dissolution of γ″ phase.
- Carbides were found at all conditions of LPBF IN625. Considering the EDS patterns and morphology of the particles, they appear to be MC carbides rich in Nb and Mo.
- Metallic oxides rich in Al were also found in all LPBF samples. Presence of oxygen in feedstock powder and in build chamber may cause these oxide inclusions. However, some of Al_2O_3 particles surrounding δ precipitates may be caused by dissolution of Al-containing γ″ precipitates.

CHAPTER 4: EVOLUTION OF MICROSTRUCTURE AND ITS EFFECT ON MECHANICAL BEHAVIOR OF LPBF UPON DIRECT AGING

In this study, an effort was made to understand evolution of microstructure and microhardness on the way to complete homogenization. Two most significant precipitates formed in IN625 are γ″ and δ that form in the range of 550-750℃ and 650-982℃, respectively [13,26,28,30,31,36,38]. Three temperatures were chosen as 700°C, 900°C and 1050°C for different lengths of time to form these precipitates mentioned and dissolve the phases at higher temperature. This study also determines the range of hardness that can be achieved until it gets close to hardness of wrought IN625. Microhardness is a useful property that is directly related to strength [74]. Formation of strengthening phase γ″ causes rise in hardness, but over ageing may lead to coarsening of γ″ and formation of detrimental phase δ that result in reduced hardness. Studies performed on AM IN625 reported significantly higher hardness compared to traditionally manufactured IN625 [34,55]. AM microstructure contributes to the superior hardness and strength but poor ductility compared to wrought material. Heat treatment of AM parts at 1100℃ makes the mechanical properties more comparable to that of wrought parts. The superior mechanical properties found in LPBF IN625 may also be attributed to high dislocation density along with the fine dendritic microstructure [44]. This study reports the change in hardness with different one step direct aging processes and tries to explain it using microstructure evolution. Proofs of different precipitates have also been provided using TEM, selected area diffraction patterns (SAED) and energy dispersive spectroscopy (EDS) to avoid ambiguity and assumptions.

4.1 Hardness

Microhardness results for all samples are presented in Fig. 31. The as printed LPBF IN625 hardness is 341.5 ± 6.06 HV1.0, which is significantly higher than the as-received wrought IN625,

223.25 ± 2.86 HV1.0. The literature well describes that the high cooling rate of LPBF produces very fine dendritic and columnar microstructures in IN625 [34], which is the cause of the hardness increase and described later.

Two primary trends in hardness of the heat treated alloy are observed. The first is that hardness values generally decreased with increasing heat treatment temperature with the 1050°C heat treatment temperature approaching that of the wrought standard. The second is that hardness increases with heat treatment time at each temperature. In general, the first can be attributed to recrystallization and grain growth processes. The kinetics of these processes increase with treatment temperature resulting in successively larger grain sizes and corresponding lower hardness. This will be considered in the microstructural analyses presented later.

The second trend of hardness increasing with treatment time at each temperature also involves evolution of the microstructure. For example, at 700°C the hardness first decreases to 325 HV1.0 after 2 hours of heat treatment before increasing successively to the highest obtained hardness of 353 HV1.0 after 10 hours. Similar increases with treatment time in their respective hardness range are seen at the 900°C and 1050°C treatment temperatures. The behavior of all three are generally indicative of the alloy experiencing precipitation hardening processes. This will be considered as the primary mechanism for the second trend in the following microstructure analysis discussion.

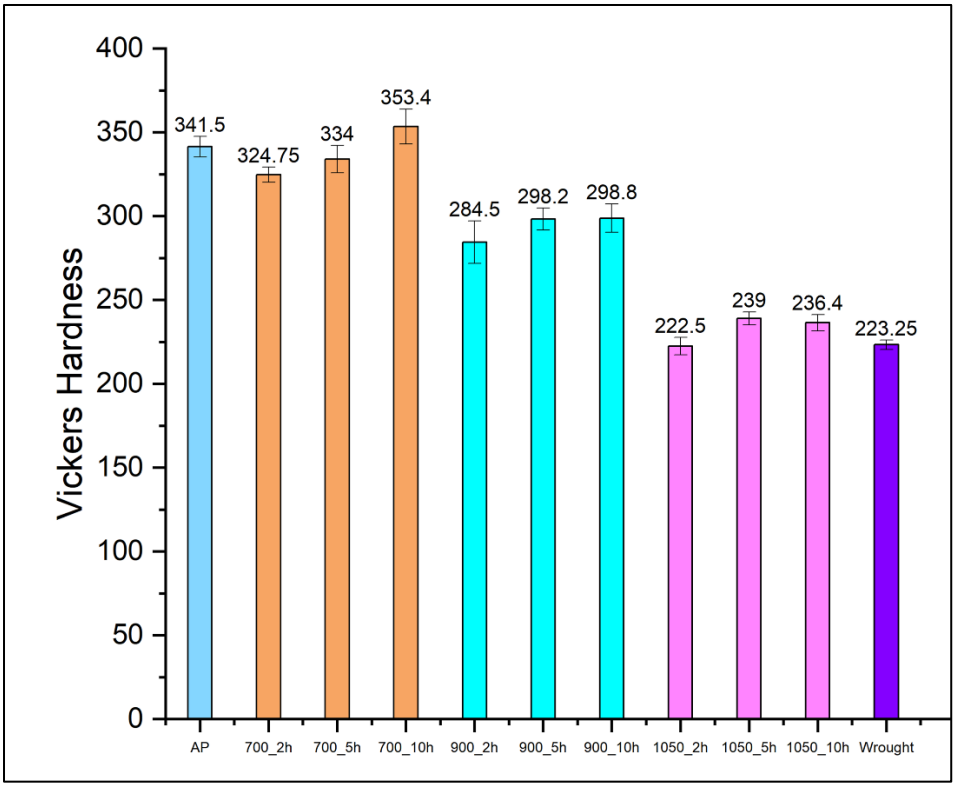

Figure 31: Microhardness of as-printed and heat treated LPBF IN625 for different temperatures and times

4.2 Microstructure: As-Printed

Fig. 32 shows SEM and TEM characterization of LPBF as-printed microstructure. The microstructure was discussed in chapter 3. Here, at higher magnification, Fig. 32(b), the cross-section of two neighboring dendrite networks of different orientation are observed. The one on the left-side is a cross-section along the elongated dendrite dimension while the right-side is a cross-section relatively perpendicular to the length.

Fig. 32(c) is a bright field TEM image of the as-printed microstructure sample. It is essentially comprised of the cross-section of a typical dendrite. Observed within the matrix are thin disc shaped precipitates approximately 3-10 nm in diameter. Selected area electron diffraction (SAED) pattern is shown in Fig. 32(d), and confirmed the precipitates as γ″. The γ″ precipitates are a secondary phase that is coherent with primary Ni-Cr based γ matrix. It grows in ellipsoidal

disc shape due to the lattice misfit strain between the tetragonal precipitate and the FCC matrix [25]. The SAED pattern is indexed according to [25]. The orientation relationship between γ″ precipitate with γ matrix can be described as [32,37]:

$$(100)\gamma'' \parallel \{100\}\gamma \text{ and } [001]\ \gamma'' \parallel \langle 100\rangle\gamma$$

The orientation relationship reveals that there are three variants of γ″ precipitates that lie on {100} planes of γ matrix. However, the SAED pattern shown in Fig. 32(d) only reveals two of the variants with the third, [001] γ″((110)γ″), variant being absent due to unknown mechanisms likely associated with the rapid, directional solidification of LPBF. The presence of γ″ in as-printed LPBF IN625 has been reported before [15], but to the authors' best knowledge rarely presented with convincing proof. Formation of γ″ directly in the as-printed condition confirms it plays a contributing role in the higher measured hardness compared to wrought IN625. Thus, the fine dendritic structure produced by LPBF and the presence of the γ″ precipitation strengthening phase are the primary influencers of the as printed hardness behaviour.

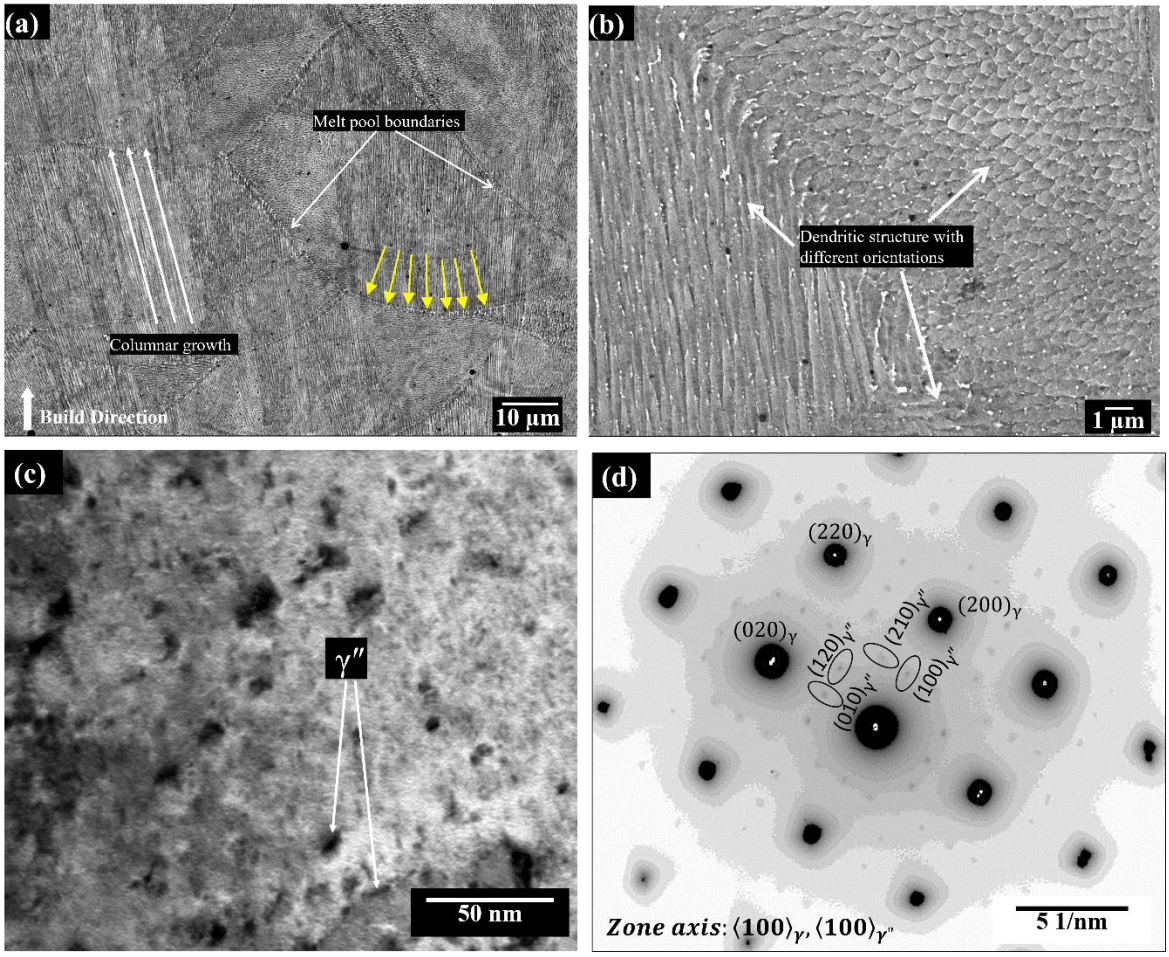

Figure 32: Microstructure of LPBF as-printed sample: (a, b) SEM images showing melt pool boundaries and dendritic growth ; (c) TEM bright field image of γ″ precipitate inside a dendrite; (d) SAED pattern of γ matrix and γ″ precipitates.

4.3 Microstructure: Heat Treated at 700°C

Post heat treatment microstructural characterization for the 700°C samples are shown in Fig. 33. After 2 hours of treatment the microstructure remains relatively unchanged from the as printed state. Melt pool boundaries and dendritic structure are retained, confirming similar observations reported by other researchers [18,34]. The overall microstructure of the 5 and 10 hour treatments also remained mostly unchanged. However, the boundaries between their columnar dendrite networks are not as straight as in the 2 hour treatment. This is highlighted in Fig. 33(d), which is a comparison between the 2 and 10 hour treatments. The boundaries (yellow lines) in the

10 hour sample appear somewhat remodeled. This phenomenon is likely attributed to the onset of recrystallization and grain growth. .

Bright field and SAED TEM characterization of the 700_2h sample are shown in Figs. 33(e) and (f) respectively. The results are very similar to the as printed sample in terms of γ″ precipitate size and frequency. Formation of γ″ precipitate in wrought IN625 at 700°C is not reported until approximately 8h of heat treatment [13]. However, with its formation in the as printed alloy, it already exists before heat treatment and is still within its stable temperature range [13]. Other works have reported γ″ precipitation in LPBF fabricated IN625. Lass et al. reported γ″ formation after heat treating for 1 hour at 870°C [57] while Gola et al. reported it after 5 hours at 600°C [64]. According to their analyses, precipitation of γ″ in a shorter amount of time is triggered by the segregation of Nb and Mo atoms in the interdendritic regions in as built structure.

The TEM results of 700°C also reveal an important development, the γ″ variant [001]γ″ ((110)γ″) that was missing in the as printed sample is now seen in the SAED pattern in Fig. 33(f). This could be attributed to the fact that the sample was directly aged from the as printed condition that contained significant residual tensile stress, measured as 77±15 MPa in other published work by the authors [70]. The complex thermomechanical phenomena that occur during LPBF result in microstructures possessing “complex and large” residual stresses [75]. Moreover, the rapid and directional solidification of columnar-like dendrites indicates limited kinetics for γ formation in at least one direction and thereby formation of coherent γ″ in the matrix. For the 700°C heat treated sample, relief of the as printed residual stress occurs and is supported by the initial reduction in measured hardness after 2 hours. In considering this fact, along with the available kinetics from the heat treatment, likely enabled the missing variant to form. In fact, heat treating under stress conditions has been shown in wrought fabricated IN625 to influence growth of one specific variant

due to the interaction between stress and the misfit strain of the precipitates with matrix [32,69,71]. This stress can be either internal residual stress or applied externally. Oblak et al. reported formation of only the [001]γ″ variant upon aging of traditionally manufactured single crystal IN718 at 790°C for 5h under a tensile load of 69 MPa [25] . It is worth noting that the sizes of [100]γ″ and [010]γ″ variants remain approximately same as in as printed condition. Therefore, [001]γ″ variant grew to an extent after heat treatment under tensile residual stress that it can be detected in a SAED pattern.

The reduction of residual stress in the 2 hour sample, supported by the appearance of the missing γ″ variant is consistent with the observed reduction in measured hardness. Heat treatment for longer times results in aging of the existing γ″ precipitates and is also consistent with the observed increase in hardness with heat treatment time. In fact, the precipitation hardening by γ″ results in the highest obtained hardness of 343 HV1.0 after 10 hours. Thus, processing by LPBF appears to have created the conditions that enabled the accelerated precipitation hardening of IN625.

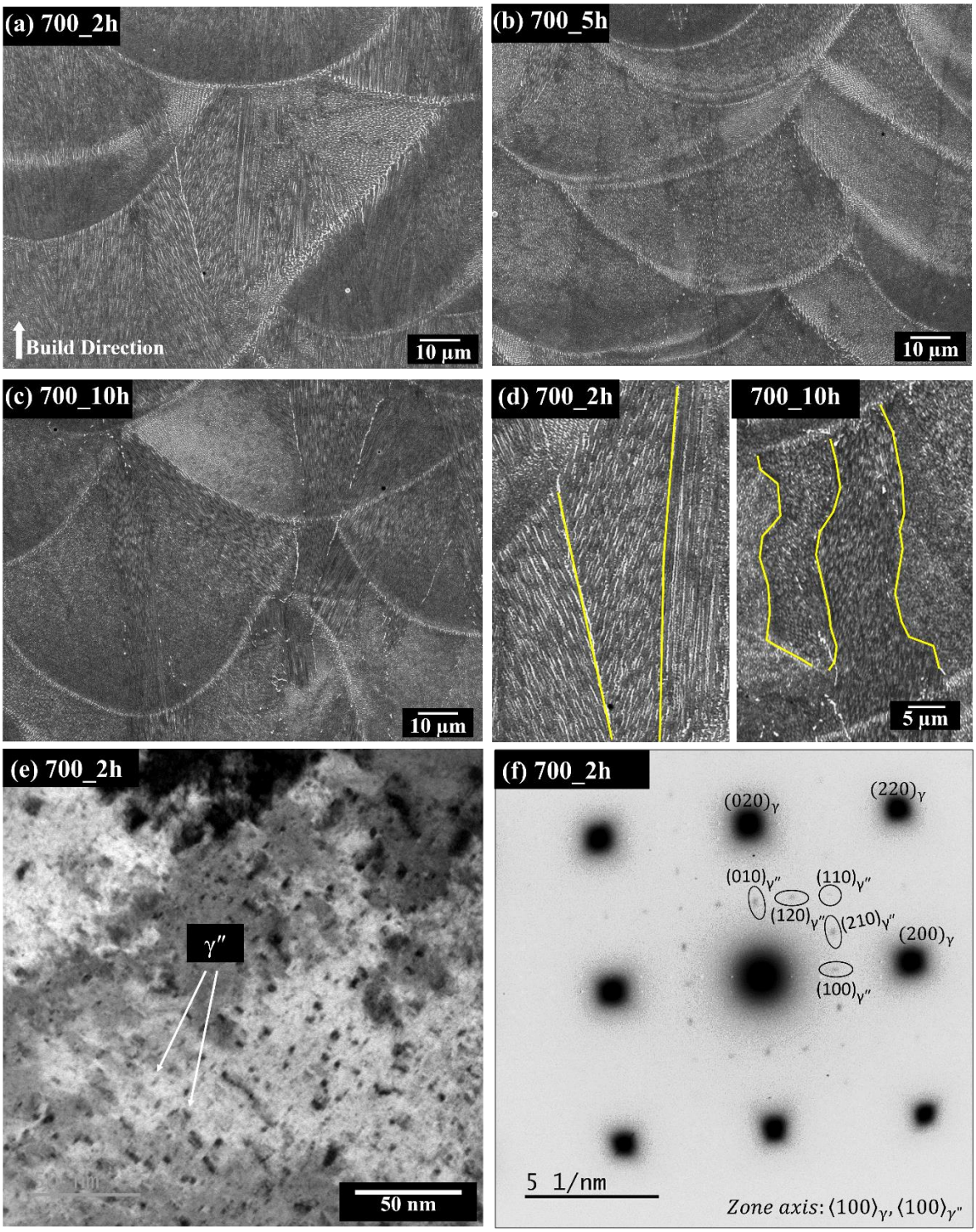

Figure 33: Microstructure of LPBF samples heat treated at 700°C: (a) SEM image of 700_2h sample; (b) SEM image of 700_5h sample; (c) SEM image of 700_10h sample; (d) High magnification SEM image comparison between 700_2h and 700_10h samples; (e) TEM image of 700_2h sample showing γ″ precipitates; (f) SAED pattern from 700_2h sample confirming 3 variants of γ″ precipitates.

4.4 Microstructure: Heat Treated at 900°C

The microstructure of LPBF IN625 after annealing at 900°C for the three treatment times is presented in Fig. 34. Partial recrystallization in certain areas as well as remnants of melt pool boundaries can be observed after 2 hours, Fig. 34(a). Needle and plate shaped precipitates that resemble the typical morphology of δ precipitates exist at both the recrystallized grain boundaries as well as remnant dendritic network regions. After the 5 and 10 hour heat treatments, from Figs. 34(b) and (c), the precipitates not only grow in size, but also in amount. Melt pool boundaries and dendritic structure have essentially disappeared in these samples. Fig. 34(d) is a zoomed region of the 2 hour (left-side) and 10 hour (right-side) treatments illustrating the change in size and distribution of the apparent δ precipitates. At 2 hours, the precipitates are approximately 1 μm in diameter and appear consistently oriented with the remnant dendrite network. After 10 hours, the precipitates are significantly larger and exist both within the grains and at the grain boundaries with those at the boundaries measurably larger.

The TEM characterization confirms the presence of the δ precipitate as well as the size difference based on location, see Fig.35. A bright field image of a larger precipitate at the grain boundary is shown in Fig. 35(a) with its corresponding SAED pattern in Fig. 35(b). An example of the smaller precipitates within the grains is shown in the bright field image in Fig 35(c) with corresponding SAED pattern in Fig. 35(d). The orientation relationship of both precipitates is $<110>\gamma||[100]\delta$ and $\{111\}\gamma||(010)\delta$. Although the δ precipitates appear to be and are sometimes referred to as needle shaped, they are actually plate-like in morphology. Furthermore, a slight rotation of the TEM thin film causes the precipitate to disappear which confirms that the particle is actually two-dimensional thin plate or disc. The plate shape of δ precipitate has also been confirmed in other studies [9,19]. Clearly, the grain boundary precipitate is larger than the

precipitate inside the grain. This is likely attributed to the faster kinetics that exist at the grain boundary [26,29,76].

Formation of δ precipitates takes much longer in traditionally manufactured wrought IN625 [12,13]. For example, it can take as long as approximately 30 hours of heat treatment to observe δ in wrought IN625 at 900°C. However, in LPBF of IN625, more rapid precipitation of δ has been widely reported by other researchers [9,19,20]. Zhang et al. observed δ precipitation at the interdendritic regions in LPBF IN625 after just 30 minutes of heat treatment at 870°C [19]. According to their analysis, elemental segregation of elements such as Nb and Mo at the interdendritic regions in AM IN625 played the primary role in more rapid precipitation compared to wrought IN625.

The initial heat treatment at 900°C for 2 hours resulted in an appreciable reduction in measured hardness. This temperature is very close to the traditional stress relief temperature of 870°C for IN625 [11]. Furthermore, the γ″ precipitation hardening phase detected in the as printed microstructure was not found in this treatment, indicating its likely dissolution and/or conversion to the δ precipitate. Although the formation of δ phase is particularly detrimental to mechanical performance, it does not appear to have formed yet in a sufficient amount. However, the observed development of the δ phase at treatment times of 5 and 10 hours resulted in modest increases in hardness. In particular, when its orthorhombic structure forms in the γ FCC matrix, a significant misfit exists between the two and is the primary cause higher hardness [34]. This is an indication that the δ precipitates formed within the grains are the primary contributor to the hardness increase.

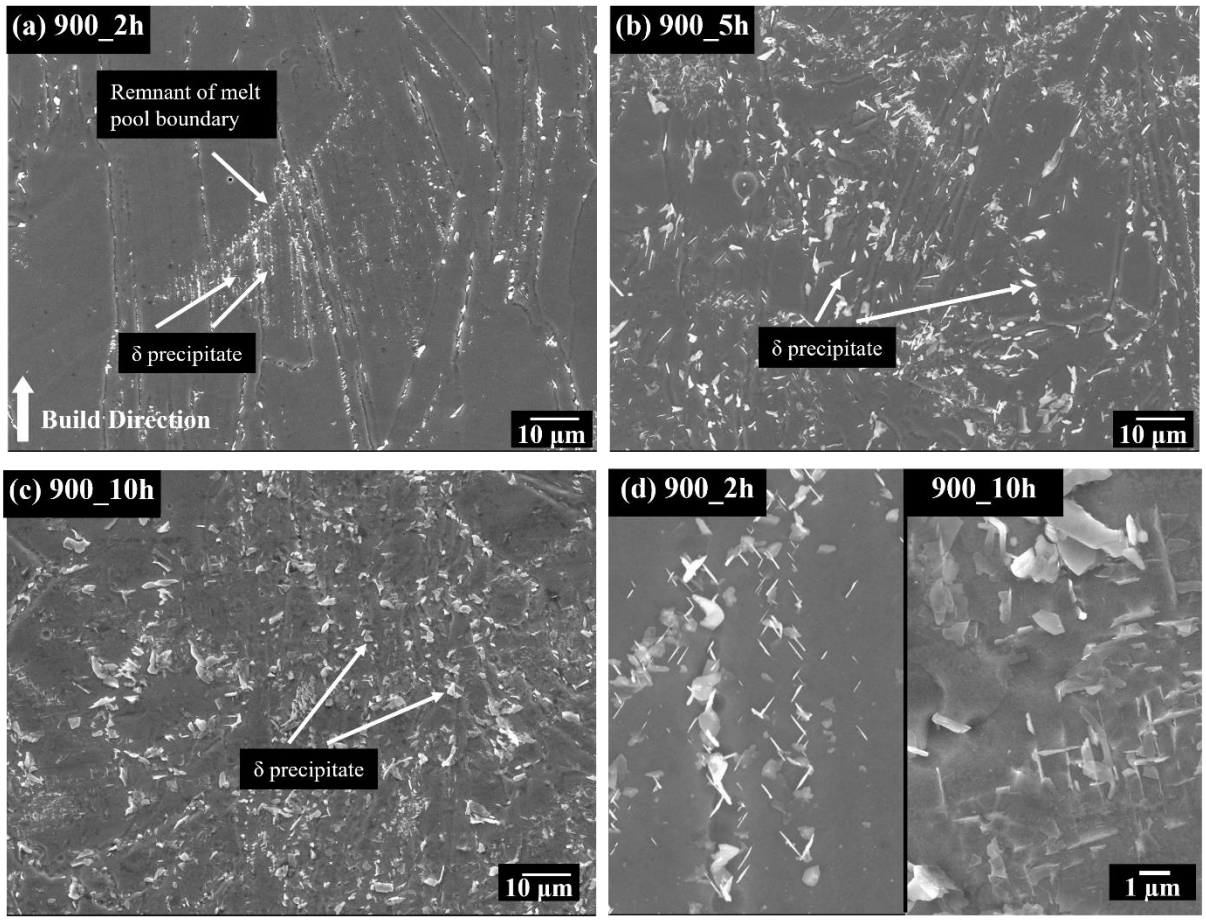

Figure 34: Microstructure of LPBF samples heat treated at 900°C: (a) SEM image of 900_2h sample; (b) SEM image of 900_5h sample; (c) SEM image of 900_10h sample; (d) High magnification SEM image comparison between 900_2h and 900_10h samples.

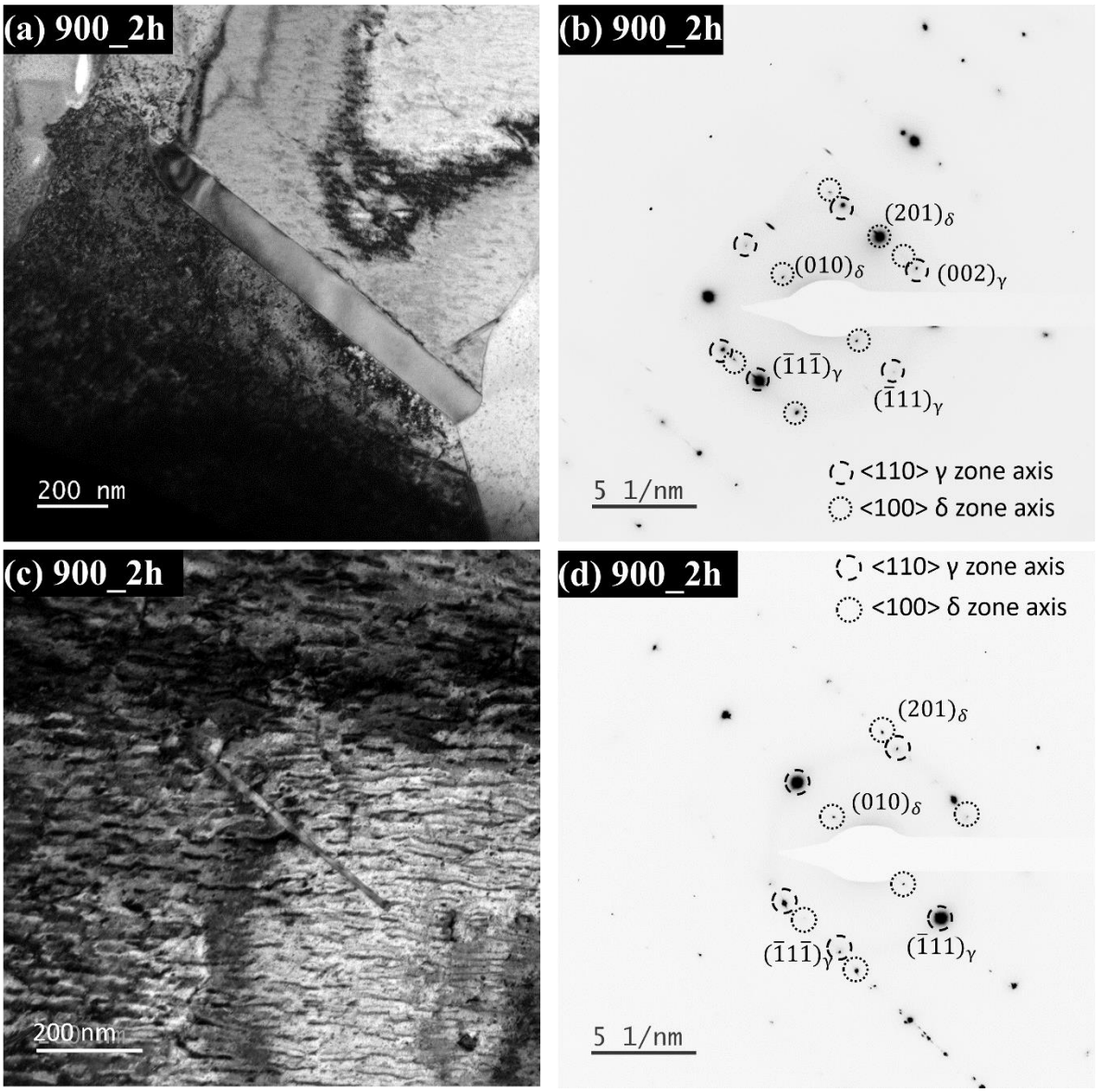

Figure 35: (a-b) TEM image and corresponding SAED pattern from 900_2h sample showing δ precipitate at a grain boundary; (c-d) TEM image and corresponding SAED pattern of 900_2h sample showing δ precipitate inside a grain.

4.5 Microstructure: Heat Treated at 1050°C

SEM micrographs of the LPBF 2, 5 and 10 hour heat treatments at 1050°C along with their comparison with the wrought standard are shown in Fig. 36. The primary microstructural comparators of these samples are the differences in grain size and the presence of carbide precipitates. The first observation is the apparent lack of melt pools and prior dendritic structure

in the LPBF samples after just 2 hours of treatment. The recrystallization and grain growth appear to have progressed sufficiently to mostly erase the as printed microstructure. However, after 5 hours of treatment, there appears to be a relative decrease in grain size before increasing appreciably after 10 hours of treatment. Also, the wrought grain size appears relatively equiaxed and measurably smaller than the LPBF samples. No evidence of γ'' and δ precipitates was found, indicating their dissolution back into the matrix.

The carbide precipitates observed in each sample can help explain the grain size results above. Firstly, the precipitates seen in Fig. 34 are identified as carbides using EDS line scans, shown in Fig. 37. Here, 1050_2h and wrought samples are compared with the LPBF carbides possessing measurably more Nb relative to Mo, which is opposite to the wrought sample. The carbides are blocky, irregular shaped, rich in Nb, Mo and Ti, deficient in Ni and Cr, and have "little to no orientation" relationship with the matrix [11]. Although any direct proof of the chemical formula of the carbides is not provided in this study, but they appear to likely be MC or M_6C considering the TTT diagram of IN625 and absence of Ni and Cr [11–13].

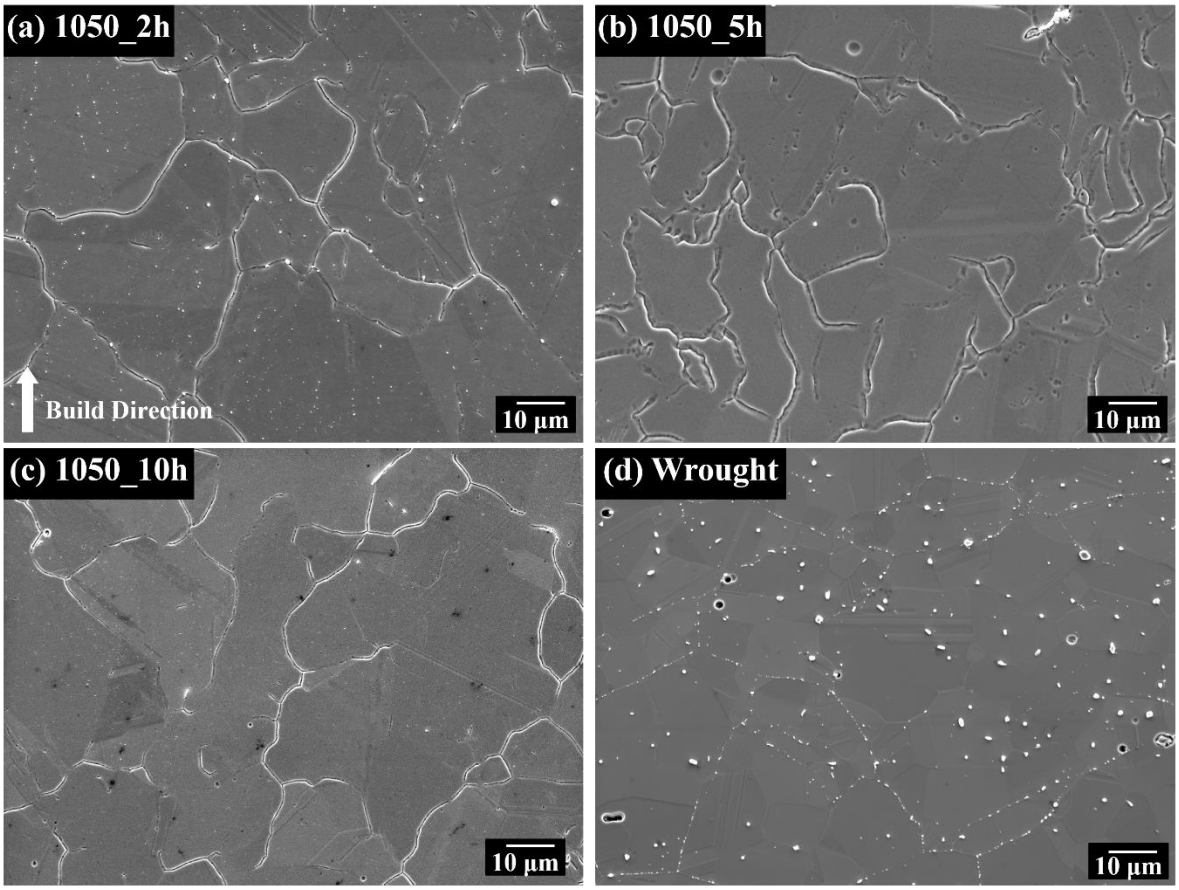

Figure 36: Microstructure of LPBF samples heat treated at 1050°C: (a) SEM image of 1050_2h sample; (b) SEM image of 1050_5h sample; (c) SEM image of 1050_10h sample; (d) SEM image of wrought IN625.

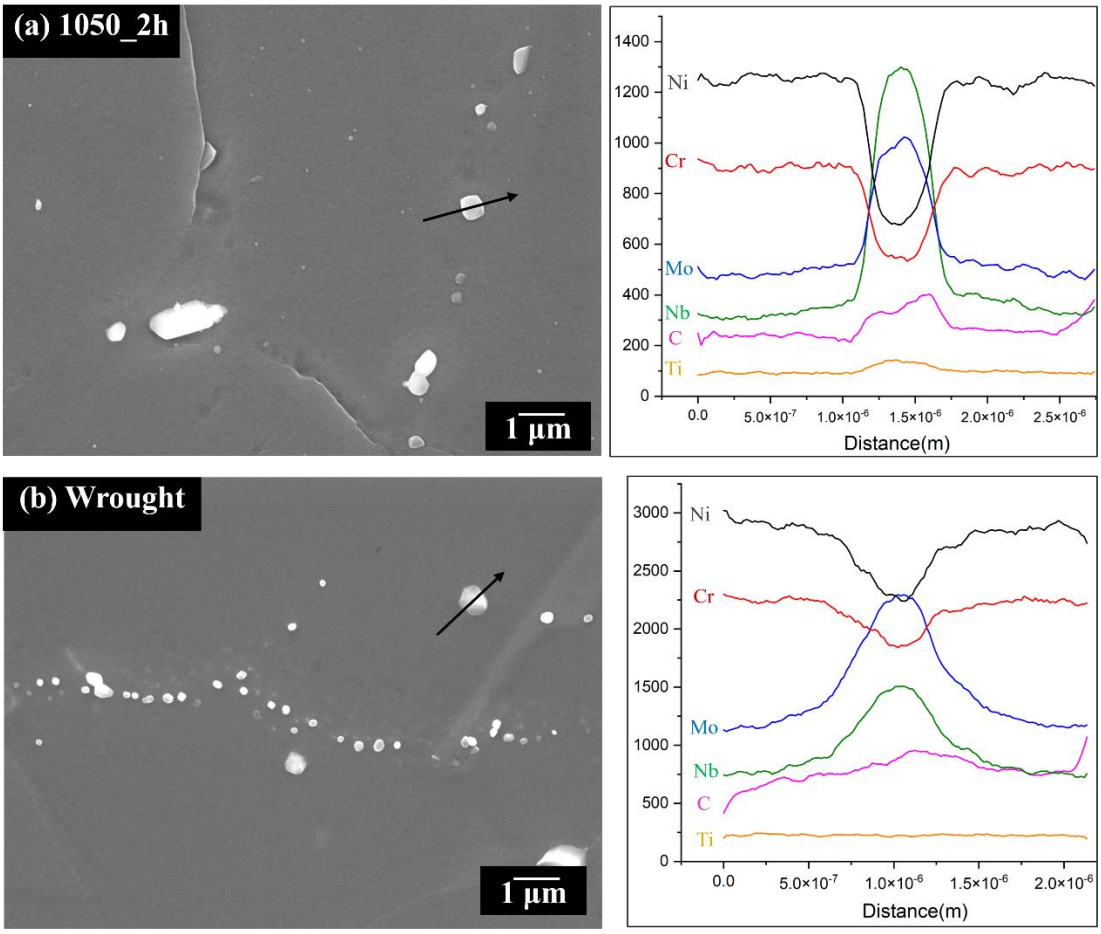

Figure 37: (a) SEM image of 1050_2h sample showing carbides with EDS pattern; (b) SEM image of wrought sample showing carbides with EDS pattern.

The carbide precipitates were observed to manifest differently in all samples. Fig. 38 are high magnification images of the 2, 5 and 10 hour treatments at 1050°C. It is interesting to note that the carbides in the 2 hour sample are larger than the 5 and 10 hour samples. This is counter to the general idea that they are expected to coarsen with heat treatment time. However, the explanation is likely related to the fact that the carbides within the 2 hour sample grains possess a regular alignment very similar to the prior dendritic network in the as printed sample, indicated by yellow line in Fig 38(a). This suggests that they were formed during the fabrication process and were relatively unaffected during the 2 hour anneal. They also suggest that even though the 2 hour sample appears to have undergone appreciable recrystallization and grain growth, that process may not have progressed as far as it may appear. In fact, this evidence offers an explanation of why the

grain size appears to have decreased from the 2 to 5 hours treatments. Although the prior dendritic network may not be easily visible, the carbide configuration suggests it is still present. Thus, further recrystallization can take place and is likely responsible for the observed grain size reduction at 5 hours. Additional evidence for recrystallization is seen by comparing the carbide size of the 2 and 5 hour samples. The carbide precipitates in the 5 hour sample are significantly smaller suggesting they have been remodeled and redistributed during recrystallization. Carbides are also seen to be mostly within grains at 5 hours while an appreciable amount are seen in the grain boundary region of the 2 hour sample. Very little change is seen in the carbide precipitates with increasing treatment time from 5 to 10 hours.

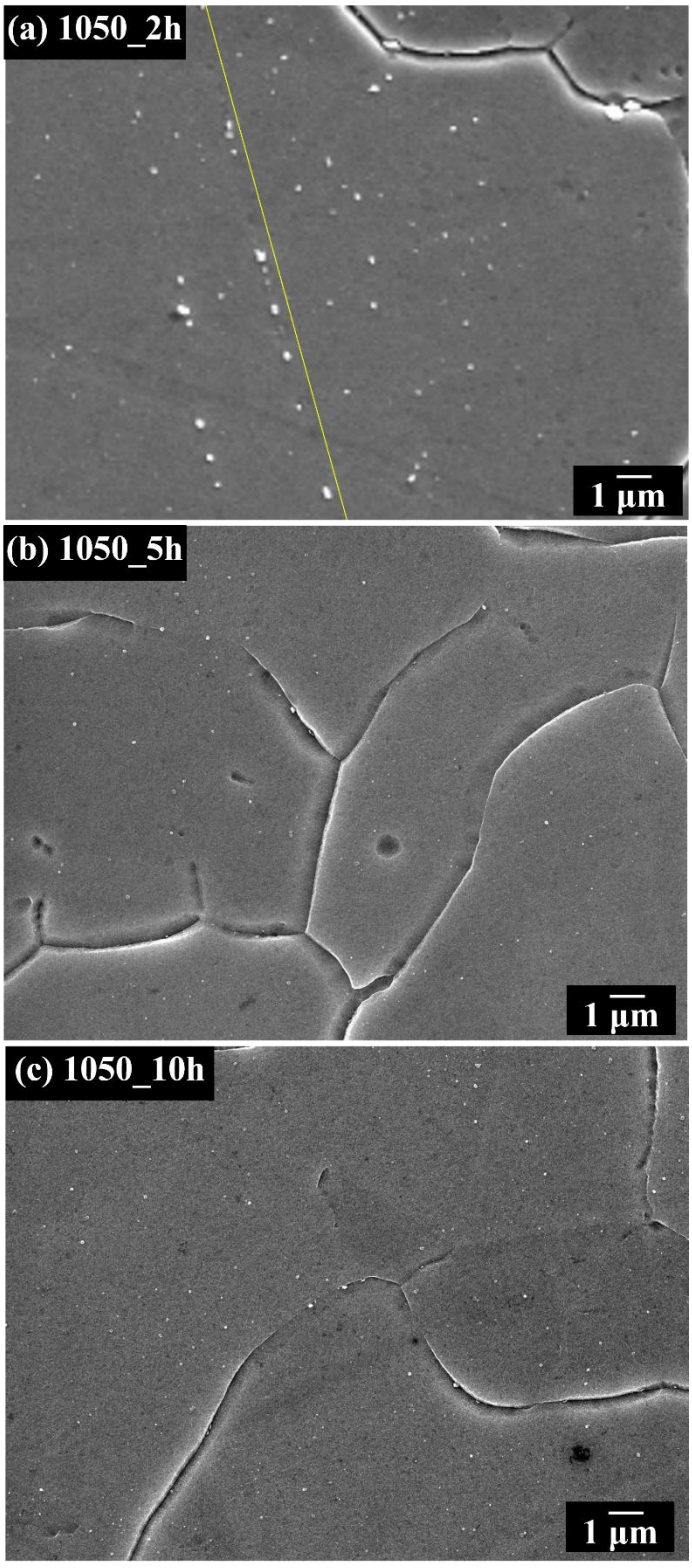

Figure 38: High magnification SEM images of (a)1050_2h; (b)1050_5h; (c)1050_10h samples showing evolution of carbides with longer heat treatment at 1050°C.

These microstructural analyses correspond well to the measured hardness of the 1050°C samples. Firstly, the significant decrease in hardness from the as printed state to the 2 hour 1050°C can be attributed both to residual stress decrease, as well as dissolution of the γ″ precipitates and apparent grain growth. This resulted in a hardness equivalent to the wrought standard. As treatment time increased to 5 hours, additional recrystallization from the remnant dendritic network occurred reducing grain size and remodeling the carbide precipitates and increasing hardness. In progressing to 10 hours of treatment, grain growth occurred towards a more equiaxed microstructure as well as some aging of the carbides, whose counteracting effects marginally decreased hardness. In comparing these results to the wrought standard similar hardness results are obtained, but with significant differences in grain size. Although the grain of the heat treated LPBF samples are larger the location of the carbides imparts a precipitation hardening effect, while the carbides in the wrought sample reside mainly at the grain boundaries.

To obtain an estimate of grain boundary strengthening, Tabor relationship can be used to calculate yield strength which again can be used in Hall-Petch relationship [77,78]. 1050_2h sample and wrought IN625 are considered. Tabor relationship between Vickers hardness in MPa and Yield strength is as follows:

$$\sigma_y = \frac{HV}{3} \quad \text{.....(4)}$$

where σ_y is yield strength and HV is Vickers hardness in MPa. σ_y for LPBF 1050_2h and wrought samples are 727.35 and 729.78 MPa, respectively using equation (4). Although the grain size of 1050_2h sample is twice as that of wrought IN625, the hardness and yield strength are only 0.33% lower than that of wrought.

Hall-Petch relationship to determine grain size strengthening can be described as:

$$\sigma_y = \sigma_0 + \frac{k}{\sqrt{d}} \quad \text{.....(5)}$$

where σ_0 and k are material constants and d is grain size. σ_0 is a measure of strengthening contributions from particles whereas $\frac{k}{\sqrt{d}}$ is a measure of grain boundary strengthening. Since σ_0 and k are same for both 1050_2h and wrought IN625, the ratio of yield strengths of the 2 samples can be described as:

$$\frac{\sigma_{y,1050\_2h}}{\sigma_{y,Wrought}} = \sqrt{\frac{d_{Wrought}}{d_{1050\_2h}}} = \sqrt{\frac{10.11}{20.43}} = 0.7 \quad \text{.....(6)}$$

It can be observed from equation (6) that the yield strength, thus, hardness of 1050_2h should be about 0.7 times of that of wrought, which is around 156 HV. But the hardness of LPBF 1050_2h is much higher than that and almost equal to the hardness of wrought IN625. Therefore, placement of carbides plays a role in the hardening of LPBF 1050_2h.

Equation (5) can be written for 1050_2h and wrought samples as follows:

$$\text{LPBF 1050\_2h: } 727.35 = \sigma_0 + \frac{k}{\sqrt{20.43E-6}} \quad \text{.....(7)}$$

$$\text{Wrought : } 729.78 = \sigma_0 + \frac{k}{\sqrt{10.11E-6}} \quad \text{.....(8)}$$

Solving equations (7) and (8) gives σ_0=721.59 MPa. The value of constant k is 5.75 and 8.177 MPa-$m^{1/2}$ for LPBF 1050_2h and wrought IN625, respectively.

Heat treating LPBF IN625 at 1050°C creates microstructure similar to that of its wrought counterpart as shown in Fig. 36(d). Larger amount of precipitates seem to be present in both grain boundaries and intragranular region of wrought IN625. EDS analysis of a carbide precipitate is presented in Fig. 37(b). Annealing twins are also clearly visible. It is interesting to notice that the grain boundaries are straighter in wrought microstructure compared to grain boundaries in LPBF IN625 that appear to be more “curved”. Studies on curvature of grain boundaries in IN625 are not largely available, but Li et al. reported that the curvature is influenced by MC carbides [34]. Several factors such as size and orientation of the carbides as well as spacing of carbon particles

affect the degree of curvature. Larger MC precipitates may cause higher degree of bending in grain boundaries whereas same orientation of neighboring carbides will result in a straight grain boundary.

4.8 Conclusion of Chapter 4

Microstructural evolution of LPBF IN625 through heat treatment at various temperatures and times and its effect on microhardness have been reported in this study. The major findings can be summarized as follows:

- As-printed LPBF microstructure consists of laser produced melt pool boundaries and dendritic regions in different orientations. Columnar growth along build direction is also evident. Two out of three variants of γ″ precipitates have also been detected. Hardness of AP LPBF IN625 was much higher than its wrought counterpart due to fine dendritic structure with elemental segregation as well as presence of γ″ precipitate.
- Microstructure was very similar to AP after heat treatment at 700°C at all times. However, the columnar growth appeared disrupted in the 5 and 10 hour heat treatments. Presence of all 3 variants of γ″ precipitates was found after treatment at 700°C. This was due to the growth of [001]γ″ variant caused by direct aging under the influence of residual stress present in AP condition. A decrease in hardness occurred after 2 hours of heat treatment due to release of some stress, but it rises again with longer heat treatment due to the formation and growth of γ″ precipitates.
- Grain recrystallization began at 900°C of heat treatment. Melt pool boundaries as well as dendritic structure were consumed with treatment time. The presence of δ precipitates was found at this temperature, which grew in size and amount as the heat treatment time increased. δ precipitates at the grain boundary became larger than those in the grain interior. The hardness

significantly decreased at this temperature after the 2 hour heat treatment, but increase at longer times due to the growth of δ precipitates.

- Microstructure was mostly recrystallized after heat treatment at 1050°C. Melt pool boundaries were erased with recrystallization and γ″ and δ precipitates were dissolved back into the matrix. However, the occasional remnant of pre-existing interdendritic regions were detected as they were highlighted with carbides formed early on in fabrication and heat treatment. Evolution of carbides was detected with increasing heat treatment time. Carbides are larger after 2 hour heat treatment in both grain boundaries as well as intragranular regions. However, carbides at the grain boundary carbides became reduced in size and amount after the 5 hour heat treatment, followed by a uniform distribution of fine carbides after 10 hours heat treatment. Microstructure of 1050°C LPBF IN625 is most similar to wrought IN625. Hardness decreases after 2 hour heat treatment due to dissolution of dendritic structure and precipitates and becomes comparable to wrought IN625, then it increases again due to finer carbide precipitation and smaller grain size with hardness decreasing slightly after 10 hour heat treatment due to grain growth.

This study investigates effect of one-step direct aging at various temperatures and lengths of time on microstructure and mechanical behavior of LPBF IN625. The typical stress relief procedures in wrought processing are not as applicable to LPBF produced alloy as the chemical segregation produced by this method facilitates precipitate formation that affects mechanical response. These results are helpful when considering how to tailor desired mechanical properties of LPBF processed forms through heat treatments.

CHAPTER 5: CHARACTERIZATION AND EVOLUTION OF δ PRECIPITATE OF LPBF INCONEL 625

δ phase is a detrimental and undesirable secondary phase in IN625 that occurs at a temperature close to the stress relief temperature for IN625, 871℃. It has been found that this phase forms in LPBF IN625 much earlier compared to wrought IN625 [9,19,20] due fine dendritic microstructure with elemental segregation at the dendrite boundaries as well as on melt pool boundaries in as-printed condition. Precipitation in wrought IN625 does not occur so early [13]. Therefore, same stress relief annealing treatment cannot be performed on LPBF IN625. This situation gave rise to the urgency to study evolution of detrimental δ phase and establish separate TTT diagram for LPBF IN625. In this study, LPBF and wrought IN625 were heat treated at 900℃ for various lengths of time ranging from 1 h to 40h and it is shown that how the precipitation differs from external surface of the sample that was exposed to the furnace ambience to the internal cross section that represents bulk sample with the help of XRD scans. Then, a systematic attempt was made to quantify the size and volume fraction of the δ precipitates that will facilitate to establish a TTT diagram for LPBF IN625 in future.

5.1 X-Ray Diffraction Analysis

Fig. 39 shows the XRD scans taken on the internal surface and external surface of heat treated wrought and LPBF IN625. No internal surface showed any peak whereas all external surfaces revealed presence of the δ phase. The presence of δ phase at 900℃ for 2h in LPBF IN625 was confirmed in another work of the authors [17]. Li et al. also did not report presence of δ peak in XRD scan on LPBF IN625 heat treated around this temperature [18]. On the other hand, Zhang et al. found δ peak in *in-situ* XRD scans on LPBF IN625 heat treated at 870℃ after as soon as 30 min. [19]. According to the TTT diagram for wrought IN625, δ phase can be found after around

30-40h heat treatment at 900°C, but Fig. 38 shows presence of δ precipitate on the external surface of wrought IN625 after heat treating it for 1h. Presence of δ peak in the XRD scans performed on the external surfaces of heat treated IN625 is no surprise, because the Cr oxide layer formed on the sample during heat treatment causes formation of nearly pure layer of δ phase in the oxide-sample interface [39–41]. Therefore, the size and amount of the δ precipitates are expected to be higher near the external surface compared to the bulk of the sample, hence, the peaks are visible for external surfaces and not for internal surfaces.

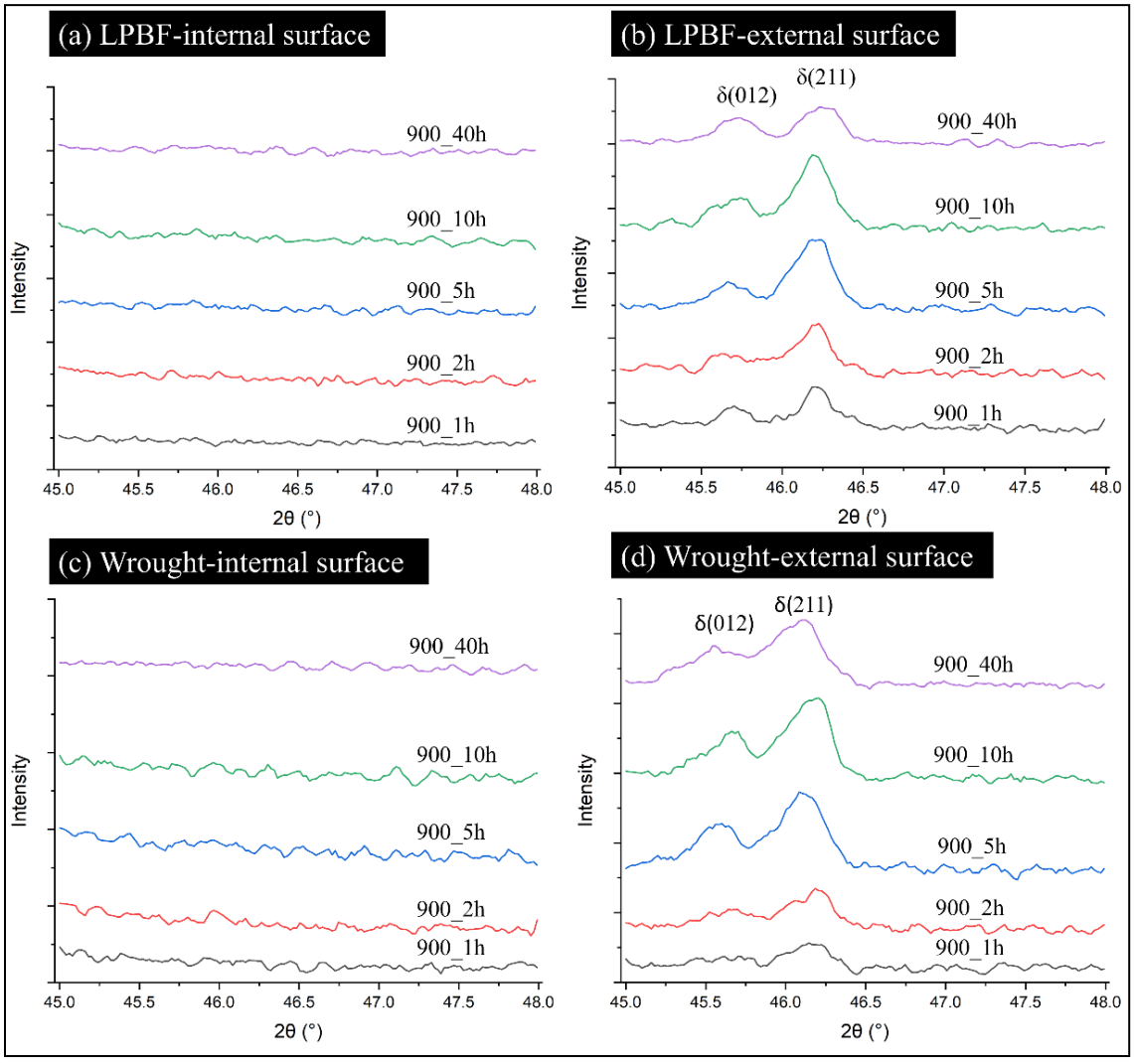

Figure 39: XRD pattern of heat treated LPBF and wrought IN625; (a) Internal surface of LPBF IN625, (b) External surface of LPBF IN625, (c) Internal surface of wrought IN625, and (d) External surface of wrought IN625.

5.2 Evolution of δ Phase: Internal vs. External Surface

SEM images of internal surfaces of all heat treated LPBF IN625 taken with backscatter electron (BSE) are shown in Fig. 40. Polished surfaces are considered instead of etching them to avoid overestimation. Plate or needle shaped δ precipitates are visible on all sample surfaces. However, the "needle" shaped precipitates are just plate shaped particles in different orientation [17]. The precipitates are present both in grain interior as well as on grain boundaries (GB). The precipitates on GB grow coarser than those inside grain [17]. 3 variants of δ precipitates can be observed on 40h sample as shown in Fig. 40(e).

It is clearly visible that the precipitates become coarser and the volume fraction of the δ phase becomes higher with increasing heat treatment time. The difference between 1h and 2h is not quite significant, however, there is visible difference from 2h to 5h in both size and amount of precipitates. Again, 5h and 10h samples appear fairly similar, but there is another jump in the volume fraction from 10h to 40h. The size of the particles in terms of area occupied by each particle as well as volume fraction of δ phase are given in table 5.

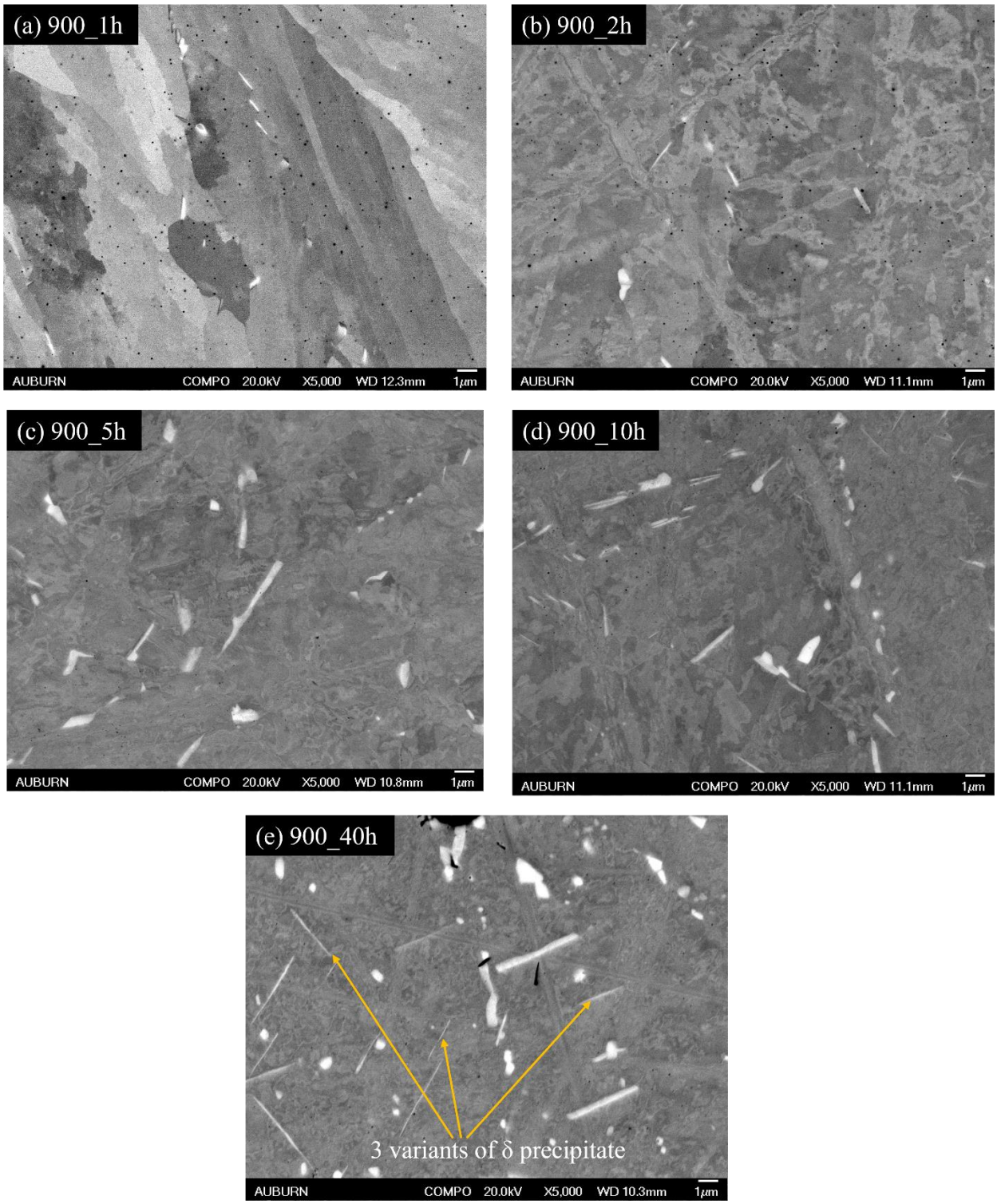

Figure 40: BSE SEM micrographs of internal surfaces of heat treated LPBF IN625; heat treated at (a) 900°C for 1h, (b) 900°C for 2h, (c) 900°C for 5h, (d) 900°C for 10h, and (e) 900°C for 40h.

An example image for particle analysis and volume fraction calculation is shown in Fig. 41, rest of the images from other samples are given in the appendix. Only particles resembling a "needle-like" shape are traced and considered to compare average particle size and volume fraction to avoid any possible confusion arising from different orientations of the particles as well as presence of carbides. Therefore, the "real" volume fraction is expected to be slightly higher than the calculated values shown in table 6.

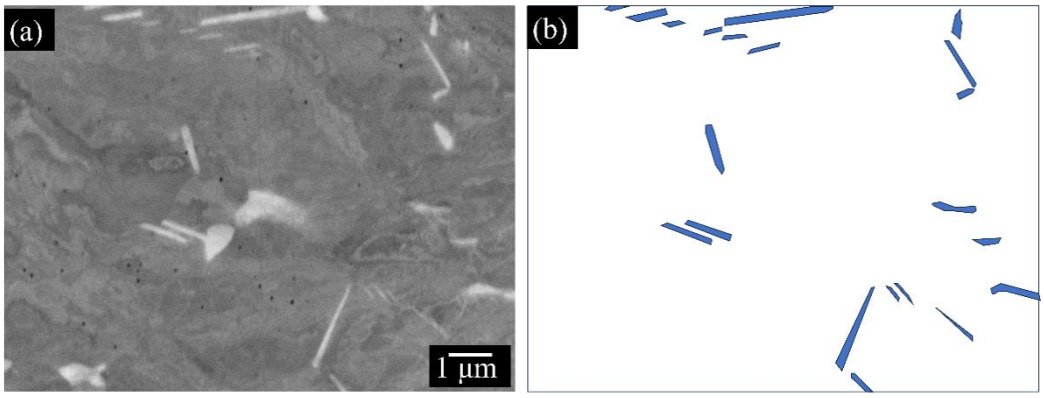

Figure 41: Example image for volume fraction calculation. (a) SEM micrograph of internal surface from 900_5h sample, and (b) needle shaped particles traced from (a).

Fig. 42 shows the graphical representation of evolution of δ precipitate size and volume fraction. The plot agrees with the microstructural observations in Fig. 40. There is hardly visible increase in the particle area and volume fraction of δ precipitates from 1h to 2h, but significant increase from 2h to 5h. There is slight decrease in both particle size and amount after 10h heat treatment that can be triggered by consumption of some precipitates during grain growth as well as formation of new thinner precipitates. There is another rise in the size an amount of δ precipitates after 40h. Considering the "plate-like" particles that have not been counted in this study, it can be safely assumed that 1% precipitation of δ phase should occur between 2 and 5 hours of heat treatment at 900℃.

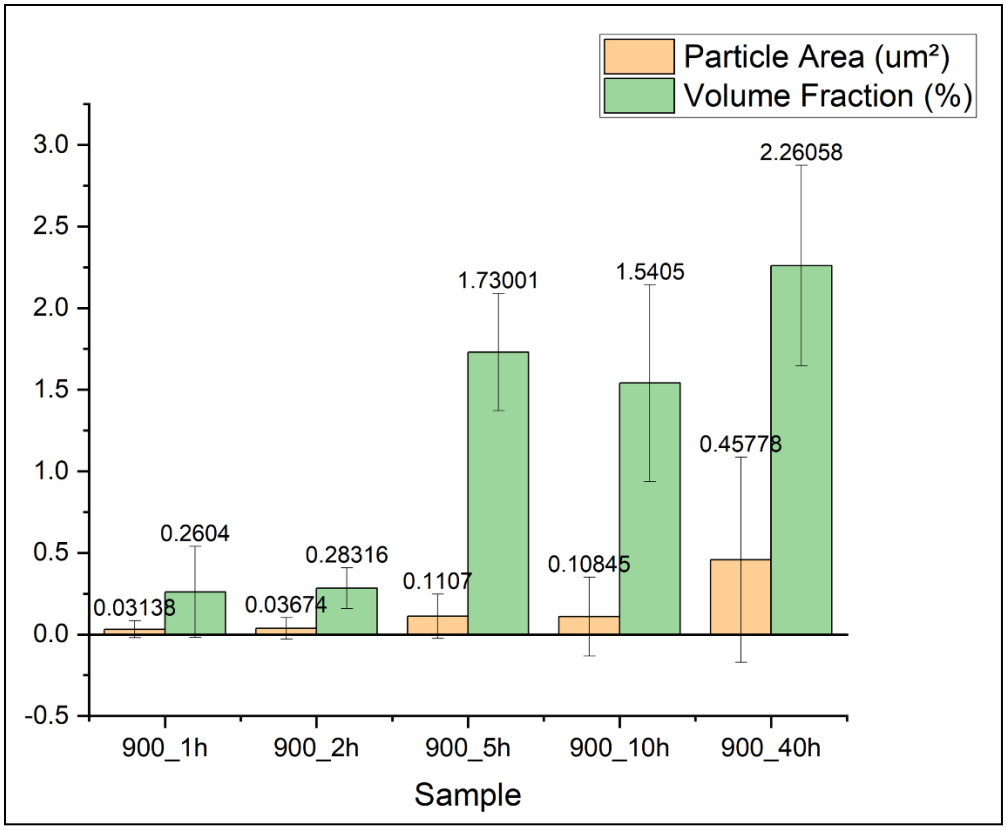

Figure 42: Evolution of particle size and volume fraction of δ precipitate with heat treatment time.

Table 6: Particle size and volume fraction of δ precipitate in different LPBF samples.

Sample	Particle area (size) (μm^2)	Volume fraction (%)
900_1h	0.03138	0.2604
900_2h	0.03674	0.28316
900_5h	0.1107	1.73001
900_10h	0.10845	1.5405
900_40h	0.45778	2.26058

Fig. 43 shows external surface of LPBF IN625 sample heat treated at 900℃ for 1h as an example. The Cr oxide layer with δ precipitates can be observed from the SEM image. Although

the size and volume fraction of δ precipitates have not quantified in this study due to the complexity of the microstructure in the presence of the oxide layer, it can be observed from Fig. 43(a) that there is a dominance of δ precipitation on the external surface compared to internal surface. Comparing to Fig. 40(a) where the average length of the precipitate is around 0.833 μm on internal surface, it is around 1.405 μm on external surface. This phenomenon has been explained by Chyrkin et al. [41]. Due to the formation of Cr oxide, there is Cr depletion right below the oxide scale which causes enrichment of other elements such as Ni, Nb and Mo in the Cr-depleted zone. This triggers diffusion of Nb towards surface from the bulk of the material causing earlier formation of δ precipitates at the oxide-alloy interface. Other studies have also confirmed this observation [39,40,42]. Due to this phenomenon, δ peaks are detected on XRD scans much earlier for external surfaces compared to external surfaces.

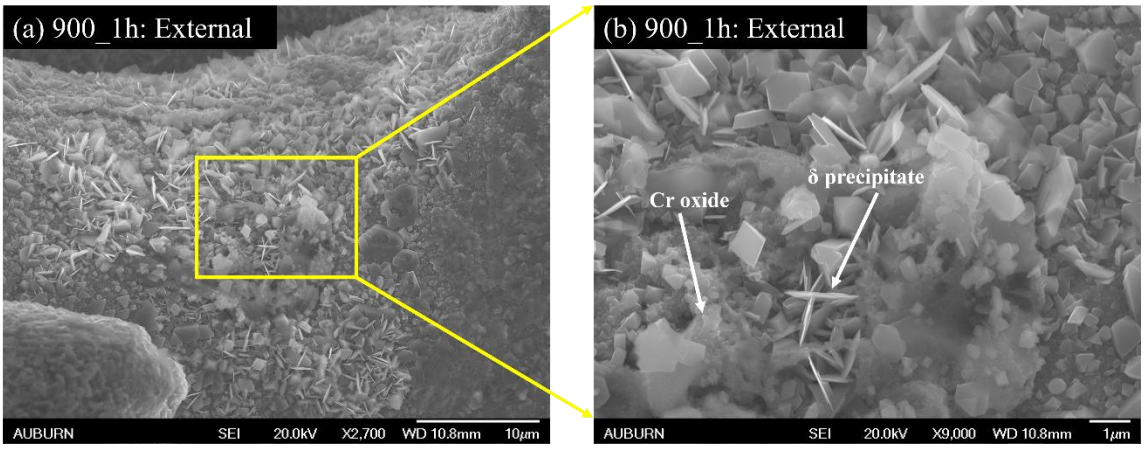

Figure 43: (a) SEM micrograph of external surface of LPBF IN625 heat treated at 900°C for 1h and (b) magnified view of the location highlighted in (a) showing δ precipitate and Cr oxide layer.

Based on the volume fraction summarized in Fig. 42 and table 6, a revised TTT diagram is proposed in Fig. 44. The precipitation of δ phase in LPBF IN625 does indeed occur faster than that in its wrought counterpart [12,13], but the shift of the TTT diagram towards the left will be more modest than it is suggested by other researchers [20].

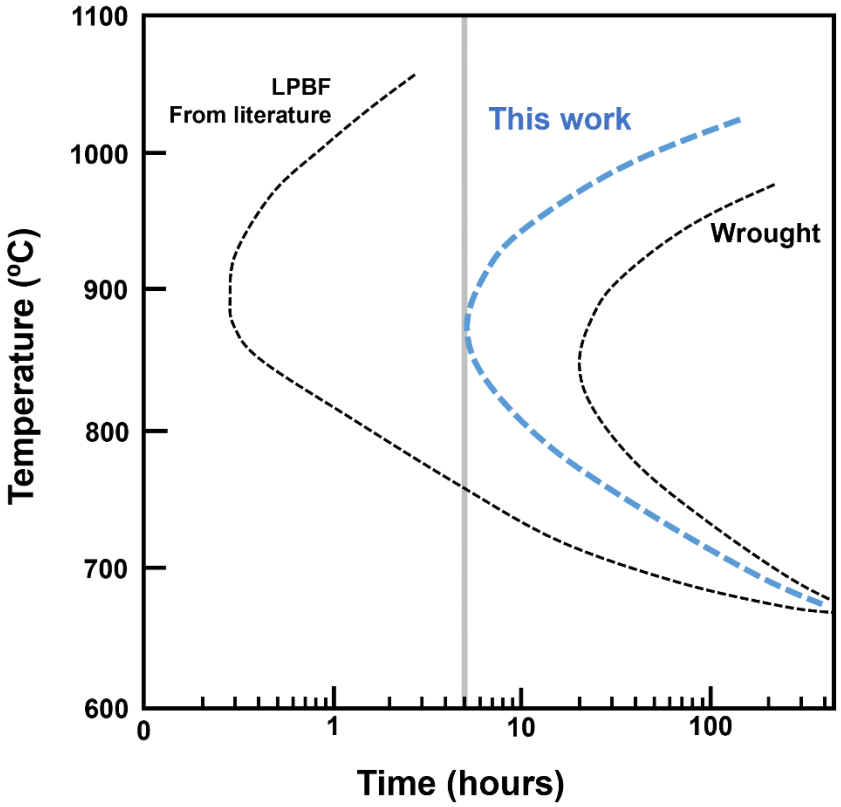

Figure 44: Proposed TTT diagram for δ phase in LPBF IN625 compared to TTT diagram from literature for LPBF and wrought IN625.

5.3 Conclusion of Chapter 5

Evolution of particle size and volume fraction of δ phase in heat treated LPBF IN625 has been investigated in this study. The major findings that can be drawn from this study can be summarized as follows:

- δ peaks appear in XRD data on external surfaces of heat treated IN625 much earlier than on internal surfaces regardless of the manufacturing technique. Therefore, it is not a reliable technique to quantify the precipitates in the bulk sample.
- Both size and volume fraction of δ particles increase with increasing heat treatment time.
- 1% precipitation of δ phase in LPBF IN625 should occur in between 2 and 5 hours when heat treated at 900°C which is faster than that in wrought IN625.

- δ precipitation on external surface of the sample occurs faster and in larger size and amount due to Cr depletion and Nb enrichment right underneath the Cr oxide layer.

CONCLUSION

Laser Powder Bed Fusion is an advanced manufacturing technique that enables producing complex parts using high strength material like Inconel 625. However, the complex microstructure produced by this technique gives rise to the necessity of studying the precipitation behavior in this material. LPBF is a near net shape manufacturing technology, therefore, only heat treatment can be used to obtain desired microstructure as well as tailor mechanical properties. This research has proved that precipitation occurs in IN625 during the manufacturing process. The study also explores presence of different variants of γ″ precipitates. Presence of at least 2 variants of δ precipitates was found at temperature as low as 700℃. Carbides and Al_2O_3 particles are found at all temperatures as well. An appreciable range of microhardness from 222.5 HV to 341 HV was obtained by different direct aging procedure and the microstructure analysis revealed that comparable hardness to wrought IN625 can be achieved in LPBF IN625 despite larger grain size. The analysis will facilitate better understanding of the microstructure evolution in LPBF IN625 compared to its wrought counterpart and tailor desired microstructure by heat treatment to achieve superior mechanical properties. A detail analysis on δ precipitate was conducted to understand evolution of this detrimental phase with different heat treatment times at 900℃. This study will enable correct prediction of formation of δ phase by contributing to a revised TTT diagram for LPBF IN625 in future.

REFERENCES

[1] Gibson I, Rosen D, Stucker B. Additive Manufacturing Technologies: 3D Printing, Rapid Prototyping, and Direct Digital Manufacturing. New York, NY: Springer New York; 2015. https://doi.org/10.1007/978-1-4939-2113-3.

[2] Additive manufacturing - General principles - Fundamentals and vocabulary: BSI British Standards; n.d. https://doi.org/10.3403/30448424.

[3] Kruth JP, Froyen L, Van Vaerenbergh J, Mercelis P, Rombouts M, Lauwers B. Selective laser melting of iron-based powder. J Mater Process Technol 2004;149:616–22. https://doi.org/10.1016/j.jmatprotec.2003.11.051.

[4] ASM Specialty Handbook: Nickel, Cobalt, and Their Alloys. ASM Int n.d. https://www.asminternational.org/asm-specialty-handbook-nickel-cobalt-and-their-alloys/results/-/journal_content/56/06178G/PUBLICATION/ (accessed May 16, 2023).

[5] O'Brien MJ. Development and qualification of additively manufactured parts for space. Opt Eng 2019;58:010801. https://doi.org/10.1117/1.OE.58.1.010801.

[6] plc R. Renishaw: Home. Renishaw n.d. http://www.renishaw.com/en/renishaw-enhancing-efficiency-in-manufacturing-and-healthcare--1030 (accessed July 14, 2023).

[7] Metal Additive Manufacturing magazine - for the latest in 3D printing. Met AM Mag 2016. https://www.metal-am.com/ (accessed July 14, 2023).

[8] Network eSites. Nickel in elemental form or alloyed with other metals and materials has made significant contributions to our present-day society and promises to continue to supply materials for an even more demanding future. n.d. https://www.nickel-alloys.net/ (accessed May 16, 2023).

[9] Lass EA, Stoudt MR, Williams ME, Katz MB, Levine LE, Phan TQ, et al. Formation of the Ni3Nb δ-Phase in Stress-Relieved Inconel 625 Produced via Laser Powder-Bed Fusion Additive Manufacturing. Metall Mater Trans A 2017;48:5547–58. https://doi.org/10.1007/s11661-017-4304-6.

[10] Reed RC. The Superalloys: Fundamentals and Applications. Cambridge University Press; 2008.

[11] Donachie MJ, Donachie SJ. Superalloys: A Technical Guide. 2nd ed. ASM International; 2002. https://doi.org/10.31399/asm.tb.stg2.9781627082679.

[12] Shoemaker LE. Alloys 625 and 725: Trends in Properties and Applications. Superalloys 718 625 706 Var. Deriv. 2005, TMS; 2005, p. 409–18. https://doi.org/10.7449/2005/Superalloys_2005_409_418.

[13] Floreen S, Fuchs GE, Yang WJ. The metallurgy of alloy 625. Superalloys 1994;718:13–37.

[14] Schröder J, Mishurova T, Fritsch T, Serrano-Munoz I, Evans A, Sprengel M, et al. On the influence of heat treatment on microstructure and mechanical behavior of laser powder bed fused Inconel 718. Mater Sci Eng A 2021;805:140555. https://doi.org/10.1016/j.msea.2020.140555.

[15] Amato K. Comparison of Microstructures and Properties for a Ni-Base Superalloy (Alloy 625) Fabricated by Electron Beam Melting. J Mater Sci Res 2012;1. https://doi.org/10.5539/jmsr.v1n2p3.

[16] Keya T, O'Donnell V, Lieben J, Romans A, Harvill G, Andurkar M, et al. Effects of Heat Treatment and Fast Neutron Irradiation on the Microstructure and Microhardness of Inconel 625 Fabricated via Laser-Powder Bed Fusion. 2021 Int. Solid Free. Fabr. Symp., University of Texas at Austin; 2021.

[17] Keya T, Bikmukhametov I, Shmatok A, Harvill G, Brewer LN, Thompson GB, et al. Evolution of Microstructure and its Influence on the Mechanical Behavior of LPBF Inconel 625 upon Direct Aging. Manuf Lett 2023.

[18] Li C, White R, Fang XY, Weaver M, Guo YB. Microstructure evolution characteristics of Inconel 625 alloy from selective laser melting to heat treatment. Mater Sci Eng A 2017;705:20–31.

[19] Zhang F, Levine LE, Allen AJ, Stoudt MR, Lindwall G, Lass EA, et al. Effect of heat treatment on the microstructural evolution of a nickel-based superalloy additive-manufactured by laser powder bed fusion. Acta Mater 2018;152:200–14.

[20] Stoudt MR, Lass EA, Ng DS, Williams ME, Zhang F, Campbell CE, et al. The influence of annealing temperature and time on the formation of δ-phase in additively-manufactured Inconel 625. Metall Mater Trans A 2018;49:3028–37.

[21] Keller T, Lindwall G, Ghosh S, Ma L, Lane BM, Zhang F, et al. Application of finite element, phase-field, and CALPHAD-based methods to additive manufacturing of Ni-based superalloys. Acta Mater 2017;139:244–53. https://doi.org/10.1016/j.actamat.2017.05.003.

[22] Liu X, Fan J, Zhang P, Cao K, Wang Z, Chen F, et al. Influence of heat treatment on Inconel 625 superalloy sheet: carbides, γ'', δ phase precipitation and tensile deformation behavior. J Alloys Compd 2023;930:167522. https://doi.org/10.1016/j.jallcom.2022.167522.

[23] Staroń S, Dubiel B, Gola K, Kalemba-Rec I, Gajewska M, Pasiowiec H, et al. Quantitative Microstructural Characterization of Precipitates and Oxide Inclusions in Inconel 625 Superalloy Additively Manufactured by L-PBF Method. Metall Mater Trans A 2022;53:2459–79. https://doi.org/10.1007/s11661-022-06679-1.

[24] Son K, Kassner ME, Lee KA. The Creep Behavior of Additively Manufactured Inconel 625. Adv Eng Mater 2020;22:1900543. https://doi.org/10.1002/adem.201900543.

[25] Oblak JM, Paulonis DF, Duvall DS. Coherency Strengthening in Ni Base Alloys Hardened by D022 Precipitates. Metall Trans n.d.:11.

[26] Sundararaman M, Mukhopadhyay P, Banerjee S. Precipitation of the δ-Ni3Nb phase in two nickel base superalloys. Metall Trans A 1988;19:453–65.

[27] Yu L-J, Marquis EA. Precipitation behavior of Alloy 625 and Alloy 625 plus. J Alloys Compd 2019;811:151916. https://doi.org/10.1016/j.jallcom.2019.151916.

[28] Suave LM, Cormier J, Villechaise P, Soula A, Hervier Z, Bertheau D, et al. Microstructural evolutions during thermal aging of alloy 625: impact of temperature and forming process. Metall Mater Trans A 2014;45:2963–82.

[29] Kirman I, Warrington DH. The Precipitation of NisNb Phases in a Ni-Fe-Cr-Nb Alloy. Metall Trans n.d.:9.

[30] Rai SK, Kumar A, Shankar V, Jayakumar T, Rao KBS, Raj B. Characterization of microstructures in Inconel 625 using X-ray diffraction peak broadening and lattice parameter measurements. Scr Mater 2004;51:59–63.

[31] Sarkar A, Mukherjee P, Barat P, Jayakumar T, Mahadevan S, Rai SK. Lattice misfit measurement in Inconel 625 by X-ray diffraction technique. Int J Mod Phys B 2008;22:3977–85.

[32] Qin H, Bi Z, Yu H, Feng G, Zhang R, Guo X, et al. Assessment of the stress-oriented precipitation hardening designed by interior residual stress during ageing in IN718 superalloy. Mater Sci Eng A 2018;728:183–95. https://doi.org/10.1016/j.msea.2018.05.016.

[33] Hong SJ, Chen WP, Wang TW. A diffraction study of the γ″ phase in INCONEL 718 superalloy. Metall Mater Trans A 2001;32:1887–901. https://doi.org/10.1007/s11661-001-0002-4.

[34] Li S, Wei Q, Shi Y, Zhu Z, Zhang D. Microstructure characteristics of Inconel 625 superalloy manufactured by selective laser melting. J Mater Sci Technol 2015;31:946–52.

[35] Dinda GP, Dasgupta AK, Mazumder J. Laser aided direct metal deposition of Inconel 625 superalloy: Microstructural evolution and thermal stability. Mater Sci Eng A 2009;509:98–104. https://doi.org/10.1016/j.msea.2009.01.009.

[36] Shankar V, Rao KBS, Mannan SL. Microstructure and mechanical properties of Inconel 625 superalloy. J Nucl Mater 2001;288:222–32.

[37] Rong Y, Chen S, Hu G, Gao M, Wei RP. Prediction and characterization of variant electron diffraction patterns for {gamma}{double_prime} and {delta} precipitates in an Inconel 718 alloy. Metall Mater Trans Phys Metall Mater Sci 1999;30. https://doi.org/10.1007/s11661-999-0239-x.

[38] Baldan R, Silva AAAP da, Tanno TM, Costa ET da, Brentegani JVN, Couto AA. Experimental Investigation of Delta Phase Precipitation in Inconel 625 Superalloy Aged at 550, 625 and 725° C. Mater Res 2020;23.

[39] Parizia S, Marchese G, Rashidi M, Lorusso M, Hryha E, Manfredi D, et al. Effect of heat treatment on microstructure and oxidation properties of Inconel 625 processed by LPBF. J Alloys Compd 2020;846:156418. https://doi.org/10.1016/j.jallcom.2020.156418.

[40] Lewis ER, Taylor MP, Attard B, Cruchley N, Morrison APC, Attallah MM, et al. Microstructural characterisation and high-temperature oxidation of laser powder bed fusion processed Inconel 625. Mater Lett 2022;311:131582. https://doi.org/10.1016/j.matlet.2021.131582.

[41] Chyrkin A, Huczkowski P, Shemet V, Singheiser L, Quadakkers WJ. Sub-Scale Depletion and Enrichment Processes During High Temperature Oxidation of the Nickel Base Alloy 625 in the Temperature Range 900–1000 °C. Oxid Met 2011;75:143–66. https://doi.org/10.1007/s11085-010-9225-3.

[42] Chyrkin A, Huczkowski P, Shemet V, Singheiser L, Quadakkers WJ. PREDICTING SUBSURFACE ENRICHMENT/DEPLETION PROCESSES DURING HIGH-TEMPERATURE OXIDATION OF ALLOY 625 THIN FOILS n.d.

[43] Chen F, Wang Q, Zhang C, Huang Z, Jia M, Shen Q. Microstructures and mechanical behaviors of additive manufactured Inconel 625 alloys via selective laser melting and laser engineered net shaping. J Alloys Compd 2022;917:165572. https://doi.org/10.1016/j.jallcom.2022.165572.

[44] Marchese G, Lorusso M, Parizia S, Bassini E, Lee J-W, Calignano F, et al. Influence of heat treatments on microstructure evolution and mechanical properties of Inconel 625 processed by laser powder bed fusion. Mater Sci Eng A 2018;729:64–75.

[45] Deng P, Song M, Yang J, Pan Q, McAllister S, Li L, et al. On the thermal coarsening and transformation of nanoscale oxide inclusions in 316L stainless steel manufactured by laser powder bed fusion and its influence on impact toughness. Mater Sci Eng A 2022;835:142690. https://doi.org/10.1016/j.msea.2022.142690.

[46] Deng P, Karadge M, Rebak RB, Gupta VK, Prorok BC, Lou X. The origin and formation of oxygen inclusions in austenitic stainless steels manufactured by laser powder bed fusion. Addit Manuf 2020;35:101334. https://doi.org/10.1016/j.addma.2020.101334.

[47] Lou X, Andresen PL, Rebak RB. Oxide inclusions in laser additive manufactured stainless steel and their effects on impact toughness and stress corrosion cracking behavior. J Nucl Mater 2018;499:182–90. https://doi.org/10.1016/j.jnucmat.2017.11.036.

[48] Yang B, Shang Z, Ding J, Lopez J, Jarosinski W, Sun T, et al. Investigation of strengthening mechanisms in an additively manufactured Haynes 230 alloy. Acta Mater 2022;222:117404. https://doi.org/10.1016/j.actamat.2021.117404.

[49] Cao GH, Sun TY, Wang CH, Li X, Liu M, Zhang ZX, et al. Investigations of γ′, γ″ and δ precipitates in heat-treated Inconel 718 alloy fabricated by selective laser melting. Mater Charact 2018;136:398–406. https://doi.org/10.1016/j.matchar.2018.01.006.

[50] Chlebus E, Gruber K, Kuźnicka B, Kurzac J, Kurzynowski T. Effect of heat treatment on the microstructure and mechanical properties of Inconel 718 processed by selective laser melting. Mater Sci Eng A 2015;639:647–55. https://doi.org/10.1016/j.msea.2015.05.035.

[51] Zhang X, Xu H, Li Z, Dong A, Du D, Lei L, et al. Effect of the scanning strategy on microstructure and mechanical anisotropy of Hastelloy X superalloy produced by Laser Powder Bed Fusion. Mater Charact 2021;173:110951. https://doi.org/10.1016/j.matchar.2021.110951.

[52] Marchese G, Basile G, Bassini E, Aversa A, Lombardi M, Ugues D, et al. Study of the Microstructure and Cracking Mechanisms of Hastelloy X Produced by Laser Powder Bed Fusion. Materials 2018;11:106. https://doi.org/10.3390/ma11010106.

[53] Yan D, Ghayoor M, Coldsnow K, Pirgazi H, Poorganji B, Ertorer O, et al. Laser powder bed fusion and post processing of alloy 22. Addit Manuf 2022;50:102490. https://doi.org/10.1016/j.addma.2021.102490.

[54] Zhao Y, Guan K, Yang Z, Hu Z, Qian Z, Wang H, et al. The effect of subsequent heat treatment on the evolution behavior of second phase particles and mechanical properties of the Inconel 718 superalloy manufactured by selective laser melting. Mater Sci Eng A 2020;794:139931. https://doi.org/10.1016/j.msea.2020.139931.

[55] Nguejio J, Szmytka F, Hallais S, Tanguy A, Nardone S, Martinez MG. Comparison of microstructure features and mechanical properties for additive manufactured and wrought nickel alloys 625. Mater Sci Eng A 2019;764:138214.

[56] Amato KN, Hernandez J, Murr LE, Martinez E, Gaytan SM, Shindo PW, et al. Comparison of microstructures and properties for a Ni-base superalloy (Alloy 625) fabricated by electron and laser beam melting. J Mater Sci Res 2012;1:3.

[57] Lass EA, Stoudt MR, Katz MB, Williams ME. Precipitation and dissolution of δ and γ″ during heat treatment of a laser powder-bed fusion produced Ni-based superalloy. Scr Mater 2018;154:83–6. https://doi.org/10.1016/j.scriptamat.2018.05.025.

[58] Zhang F, Ilavsky J, Lindwall G, Stoudt MR, Levine LE, Allen AJ. Solid-State Transformation of an Additive Manufactured Inconel 625 Alloy at 700 °C. Appl Sci 2021;11:8643. https://doi.org/10.3390/app11188643.

[59] Marchese G, Bassini E, Parizia S, Manfredi D, Ugues D, Lombardi M, et al. Role of the chemical homogenization on the microstructural and mechanical evolution of prolonged heat-treated laser powder bed fused Inconel 625. Mater Sci Eng A 2020;796:140007. https://doi.org/10.1016/j.msea.2020.140007.

[60] Carter LN, Martin C, Withers PJ, Attallah MM. The influence of the laser scan strategy on grain structure and cracking behaviour in SLM powder-bed fabricated nickel superalloy. J Alloys Compd 2014;615:338–47. https://doi.org/10.1016/j.jallcom.2014.06.172.

[61] Giannuzzi LA, Drown JL, Brown SR, Irwin RB, Stevie FA. Focused ion beam milling and micromanipulation lift-out for site specific cross-section TEM specimen preparation. MRS Online Proc Libr OPL 1997;480.

[62] Wang Z, Guan K, Gao M, Li X, Chen X, Zeng X. The microstructure and mechanical properties of deposited-IN718 by selective laser melting. J Alloys Compd 2012;513:518–23. https://doi.org/10.1016/j.jallcom.2011.10.107.

[63] Zhang F, Levine LE, Allen AJ, Campbell CE, Lass EA, Cheruvathur S, et al. Homogenization kinetics of a nickel-based superalloy produced by powder bed fusion laser sintering. Scr Mater 2017;131:98–102. https://doi.org/10.1016/j.scriptamat.2016.12.037.

[64] Gola K, Dubiel B, Kalemba-Rec I. Microstructural Changes in Inconel 625 Alloy Fabricated by Laser-Based Powder Bed Fusion Process and Subjected to High-Temperature Annealing. J Mater Eng Perform 2020;29:1528–34. https://doi.org/10.1007/s11665-020-04605-3.

[65] Calandri M, Yin S, Aldwell B, Calignano F, Lupoi R, Ugues D. Texture and Microstructural Features at Different Length Scales in Inconel 718 Produced by Selective Laser Melting. Materials 2019;12:1293. https://doi.org/10.3390/ma12081293.

[66] Kulawik K, Buffat PA, Kruk A, Wusatowska-Sarnek AM, Czyrska-Filemonowicz A. Imaging and characterization of γ′ and γ″ nanoparticles in Inconel 718 by EDX elemental mapping and FIB–SEM tomography. Mater Charact 2015;100:74–80. https://doi.org/10.1016/j.matchar.2014.12.012.

[67] Zhang RY, Qin HL, Bi ZN, Tang YT, Araújo de Oliveira J, Lee TL, et al. γ″ variant-sensitive deformation behaviour of Inconel 718 superalloy. J Mater Sci Technol 2022;126:169–81. https://doi.org/10.1016/j.jmst.2022.03.018.

[68] Zhang H, Li C, Guo Q, Ma Z, Li H, Liu Y. Improving creep resistance of nickel-based superalloy Inconel 718 by tailoring gamma double prime variants. Scr Mater 2019;164:66–70. https://doi.org/10.1016/j.scriptamat.2019.01.041.

[69] Zhang RY, Qin HL, Bi ZN, Li J, Paul S, Lee TL, et al. Evolution of Lattice Spacing of Gamma Double Prime Precipitates During Aging of Polycrystalline Ni-Base Superalloys: An In Situ Investigation. Metall Mater Trans A 2020;51:574–85. https://doi.org/10.1007/s11661-019-05536-y.

[70] Andurkar M, Suzuki T, Omori M, Prorok B, Gahl J. Residual Stress Measurements via X-ray Diffraction Cos α Method on Various Heat-Treated Inconel 625 Specimens Fabricated via Laser-Powder Bed Fusion n.d.:13.

[71] Zhang R, Qin H, Bi Z, Li J, Paul S, Lee T, et al. Using Variant Selection to Facilitate Accurate Fitting of γ″ Peaks in Neutron Diffraction. Metall Mater Trans A 2019;50. https://doi.org/10.1007/s11661-019-05393-9.

[72] Dehmas M, Lacaze J, Niang A, Viguier B. TEM Study of High-Temperature Precipitation of Delta Phase in Inconel 718 Alloy. Adv Mater Sci Eng 2011;2011:1–9. https://doi.org/10.1155/2011/940634.

[73] Zhang JP, Ye HQ, Kuo KH, Amelinckx S. A High-Resolution Electron Microscopy Study of the Domain Structure in Ni3Nb. II. Orientation and General Domains. Phys Status Solidi A 1986;93:457–62. https://doi.org/10.1002/pssa.2210930207.

[74] Tian Z, Zhang C, Wang D, Liu W, Fang X, Wellmann D, et al. A Review on Laser Powder Bed Fusion of Inconel 625 Nickel-Based Alloy. Appl Sci 2020;10:81. https://doi.org/10.3390/app10010081.

[75] Attallah MM, Jennings R, Wang X, Carter LN. Additive manufacturing of Ni-based superalloys: The outstanding issues. MRS Bull 2016;41:758–64. https://doi.org/10.1557/mrs.2016.211.

[76] Rafiei M, Mirzadeh H, Malekan M. Precipitation kinetics of γ ″phase and its mechanism in a Nb-bearing nickel-based superalloy during aging. Vacuum 2020;178:109456.

[77] Hansen N. Hall–Petch relation and boundary strengthening. Scr Mater 2004;51:801–6. https://doi.org/10.1016/j.scriptamat.2004.06.002.

[78] Tabor D, Taylor GI. A simple theory of static and dynamic hardness. Proc R Soc Lond Ser Math Phys Sci 1997;192:247–74. https://doi.org/10.1098/rspa.1948.0008.

APPENDIX

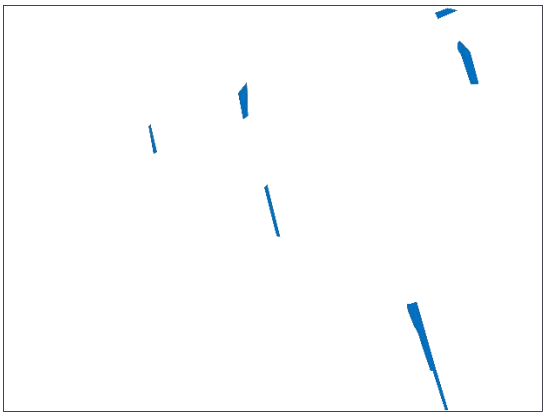

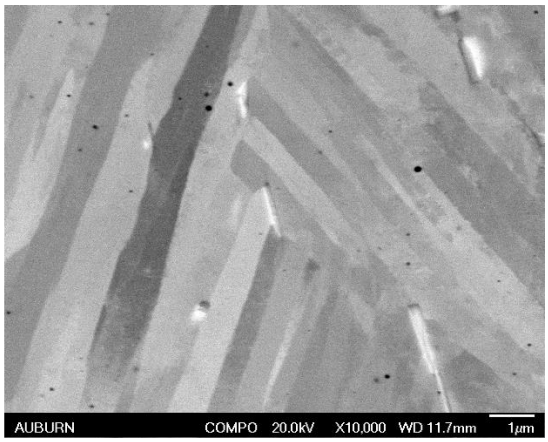
AUBURN COMPO 20.0kV X10,000 WD 11.7mm 1μm

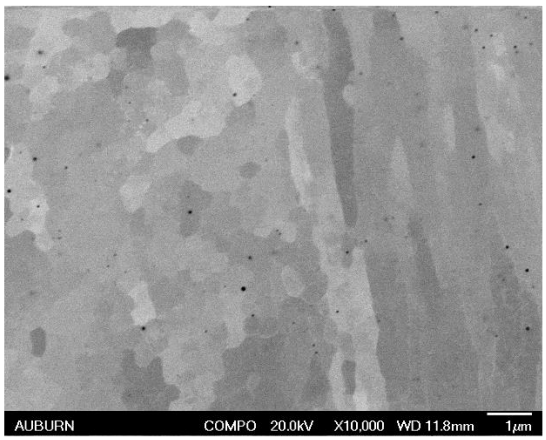
AUBURN COMPO 20.0kV X10,000 WD 11.8mm 1μm

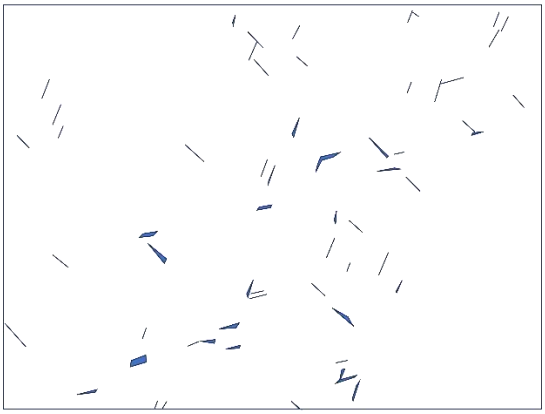

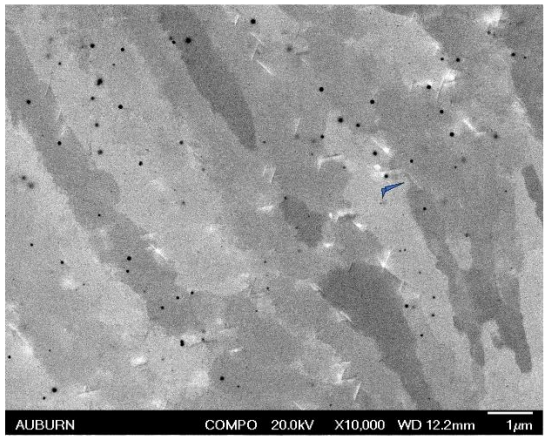
AUBURN COMPO 20.0kV X10,000 WD 12.2mm 1μm

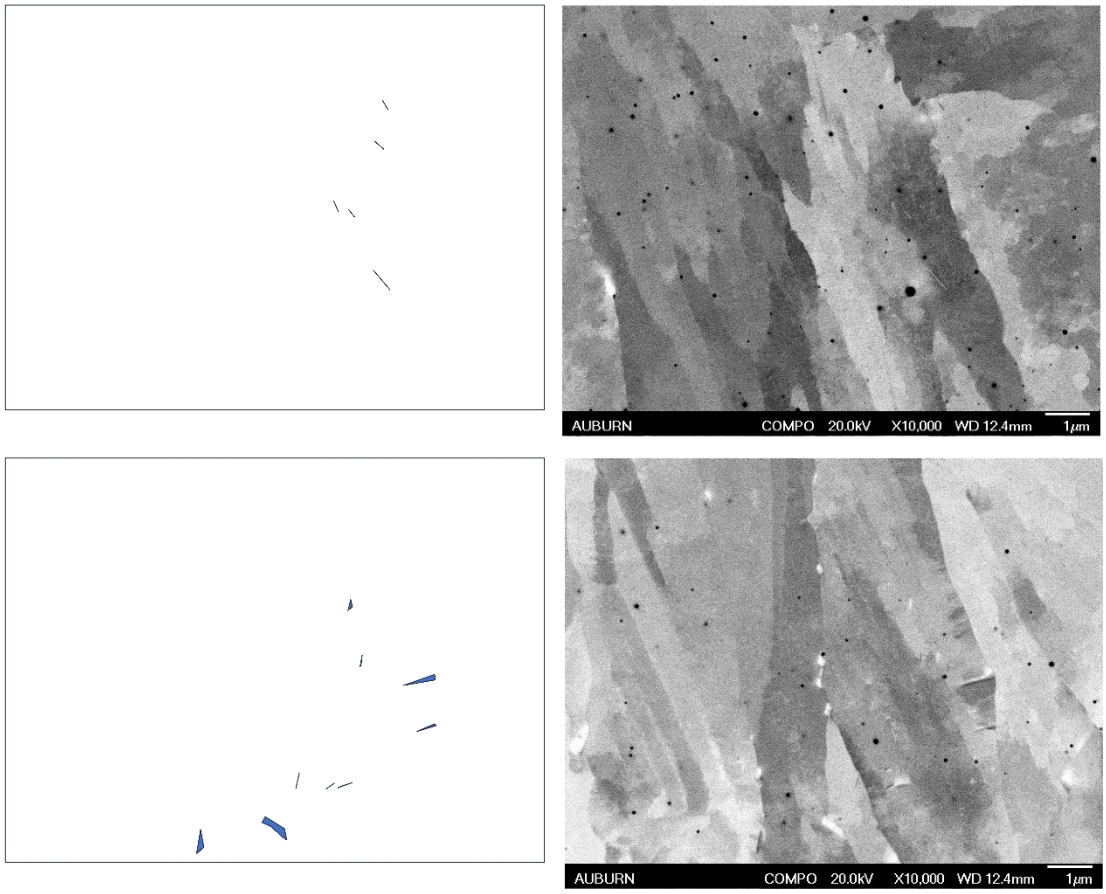

Figure 45: SEM BSE images from internal surface of 900_1h sample.

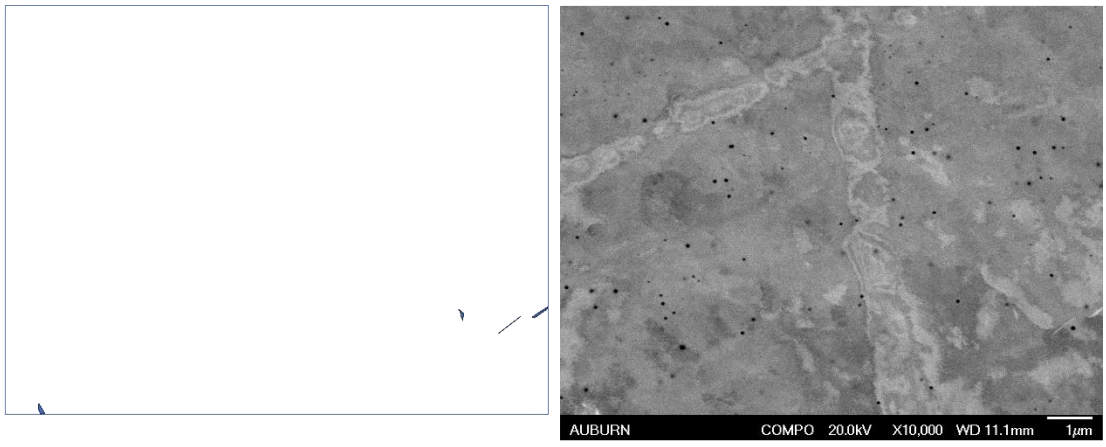

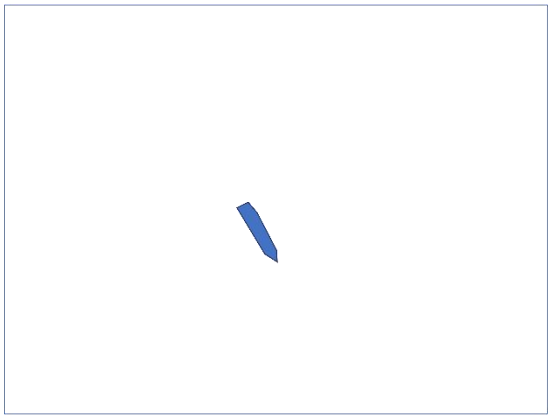

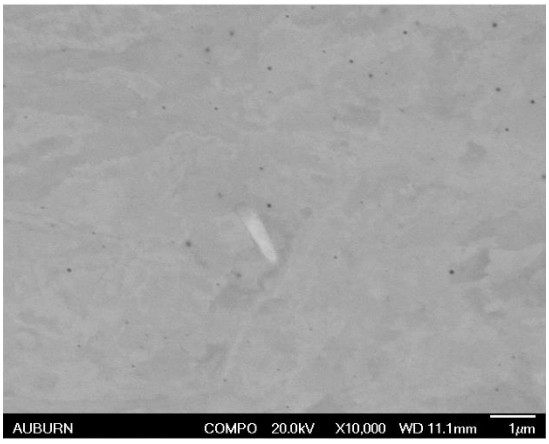
AUBURN COMPO 20.0kV X10,000 WD 11.1mm 1μm

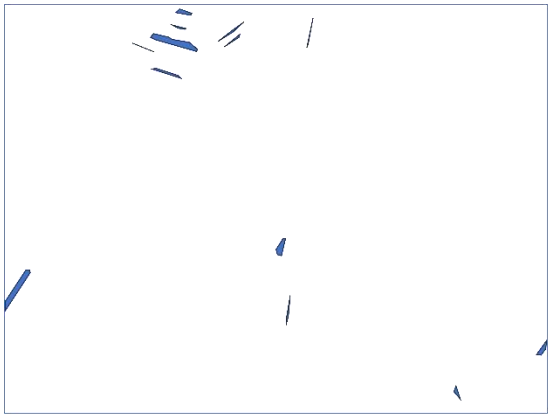

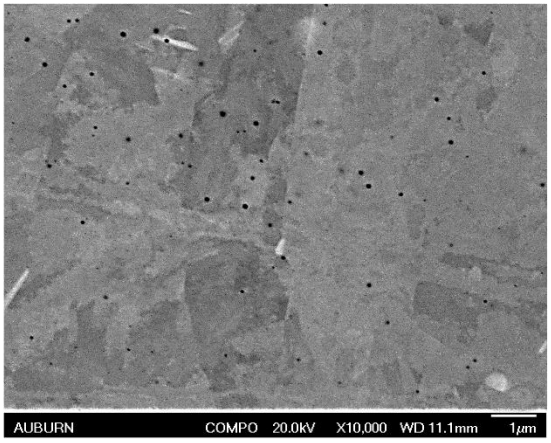
AUBURN COMPO 20.0kV X10,000 WD 11.1mm 1μm

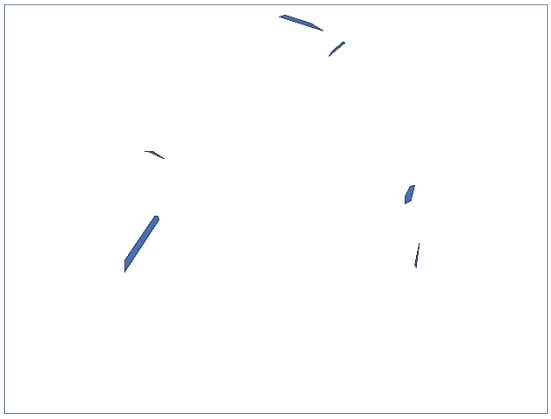

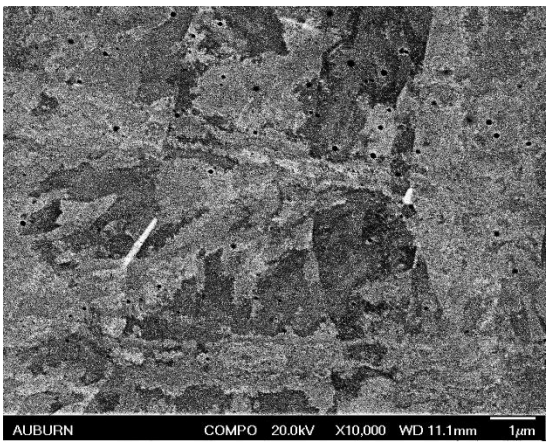
AUBURN COMPO 20.0kV X10,000 WD 11.1mm 1μm

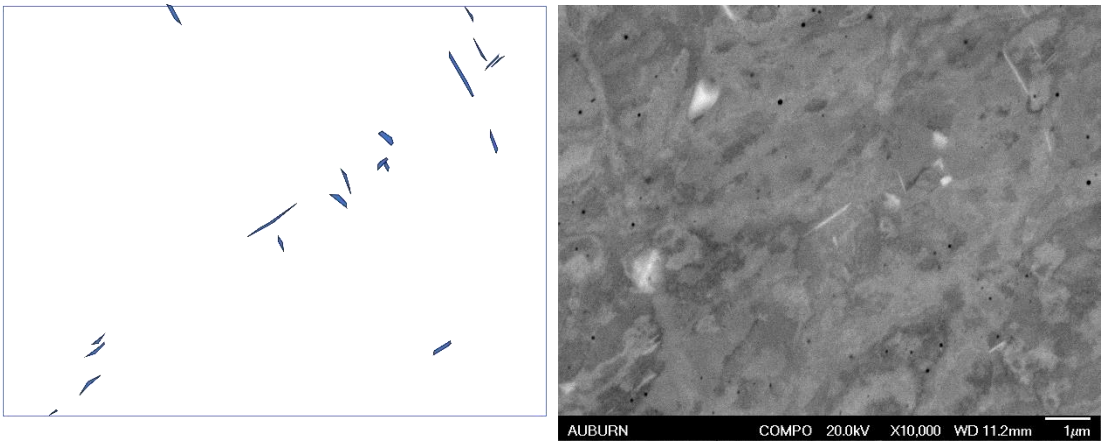

Figure 46: SEM BSE images from internal surface of 900_2h sample.

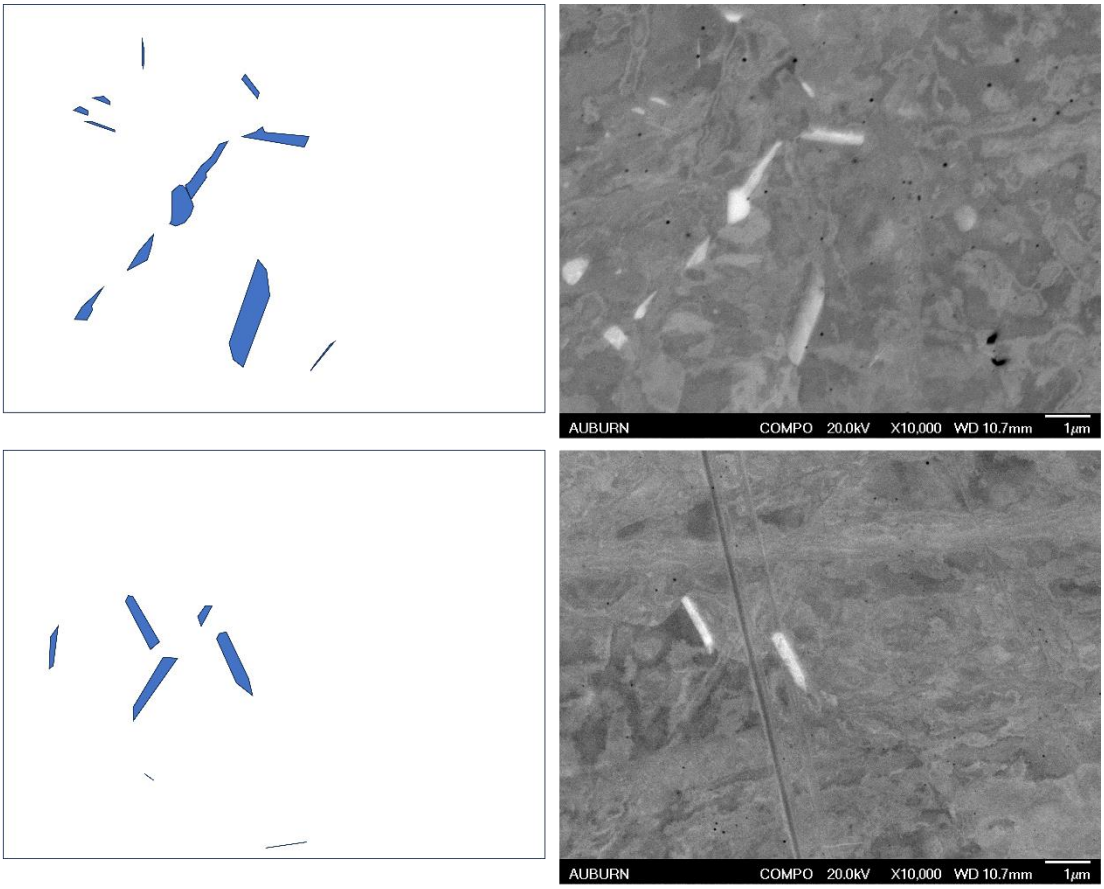

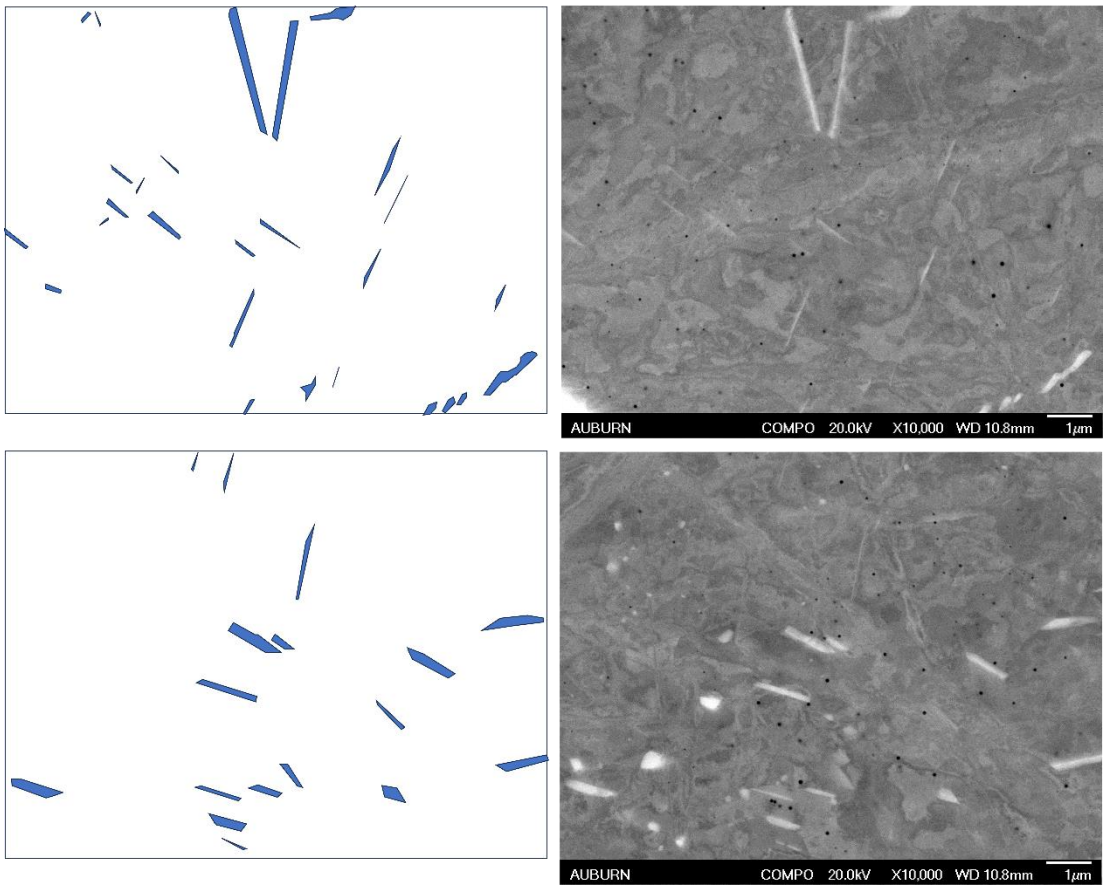

Figure 47: SEM BSE images from internal surface of 900_5h sample.

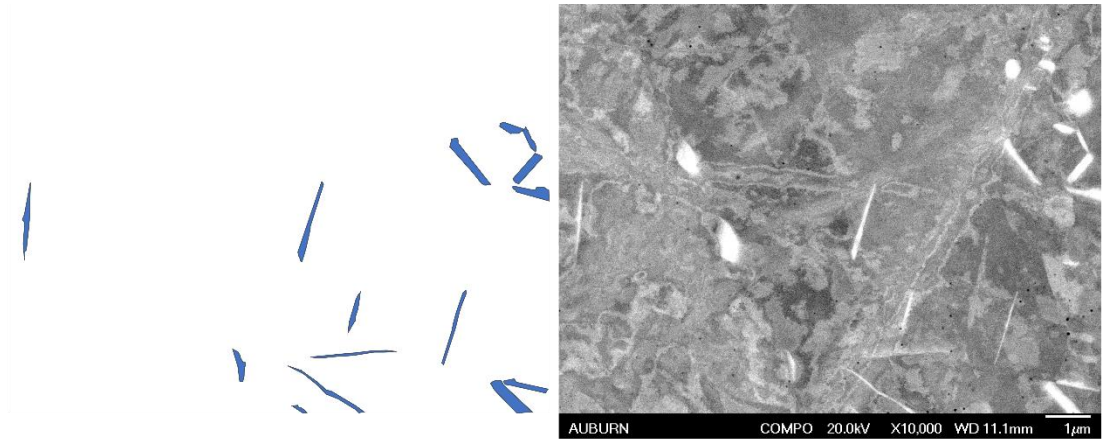

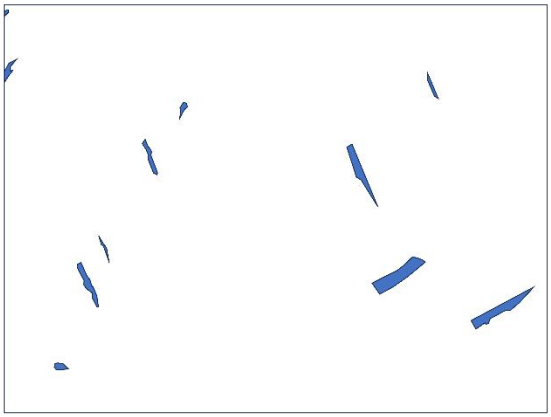

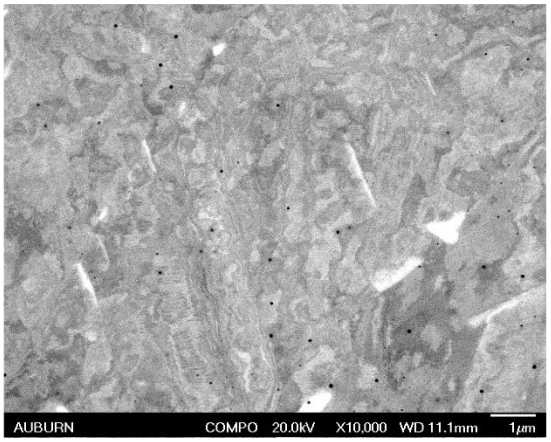
AUBURN COMPO 20.0kV X10,000 WD 11.1mm 1μm

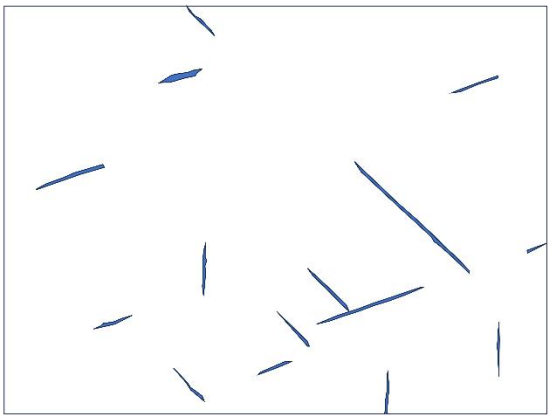

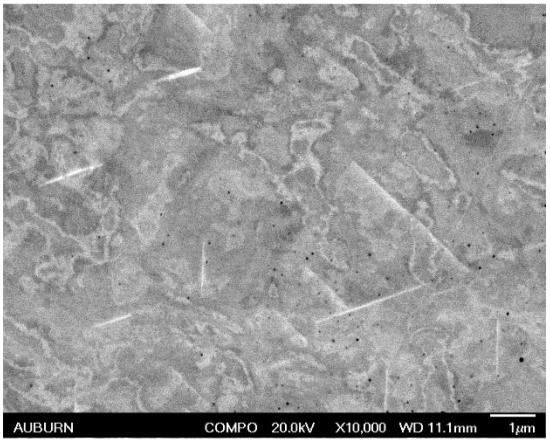
AUBURN COMPO 20.0kV X10,000 WD 11.1mm 1μm

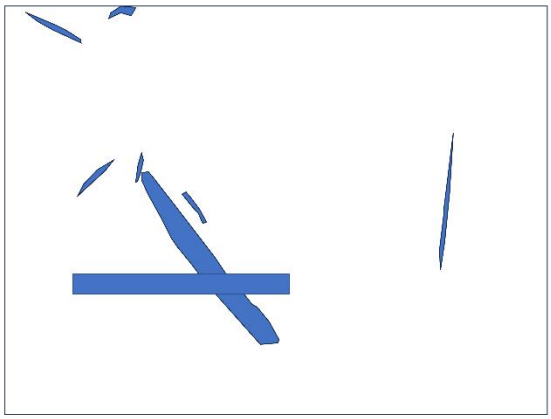


AUBURN COMPO 20.0kV X10,000 WD 11.1mm 1μm

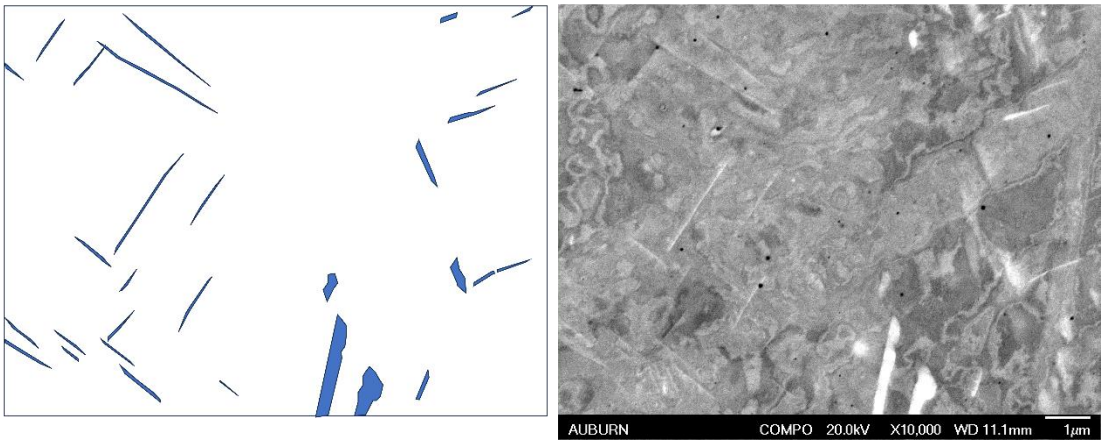

Figure 48: SEM BSE images from internal surface of 900_10h sample.

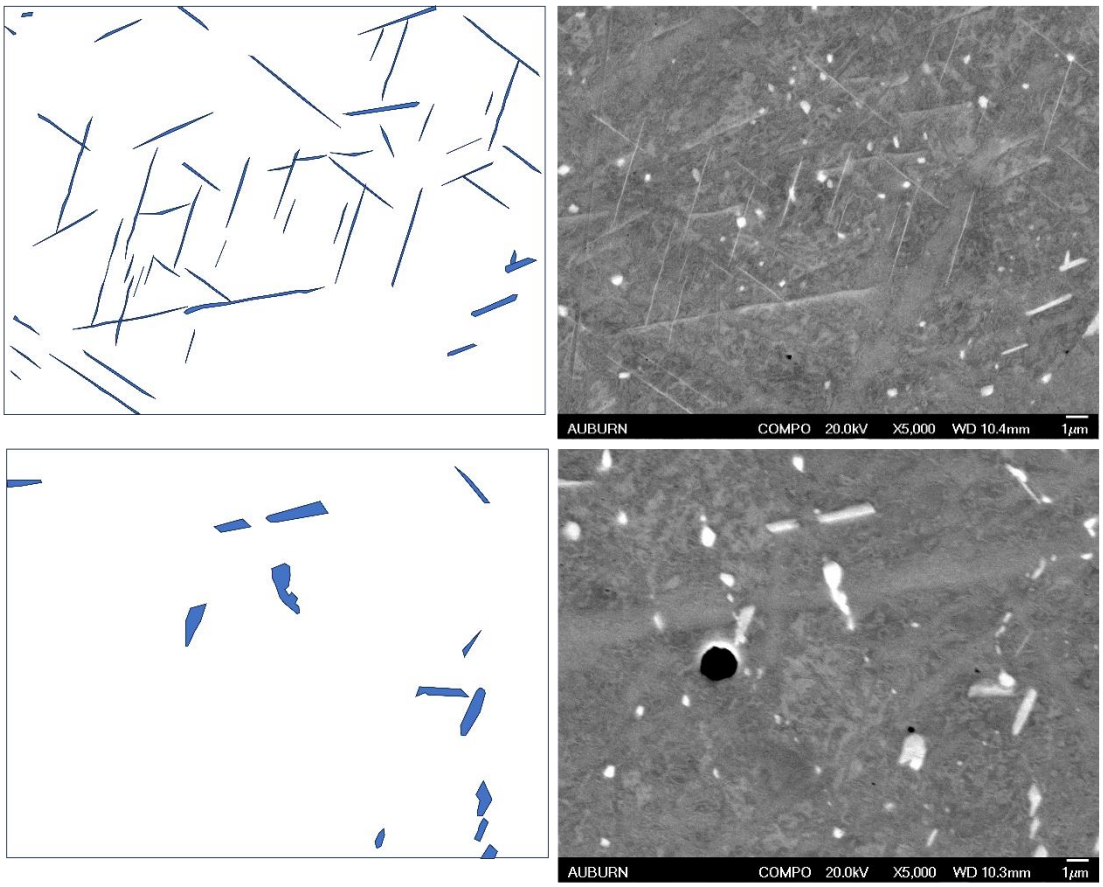

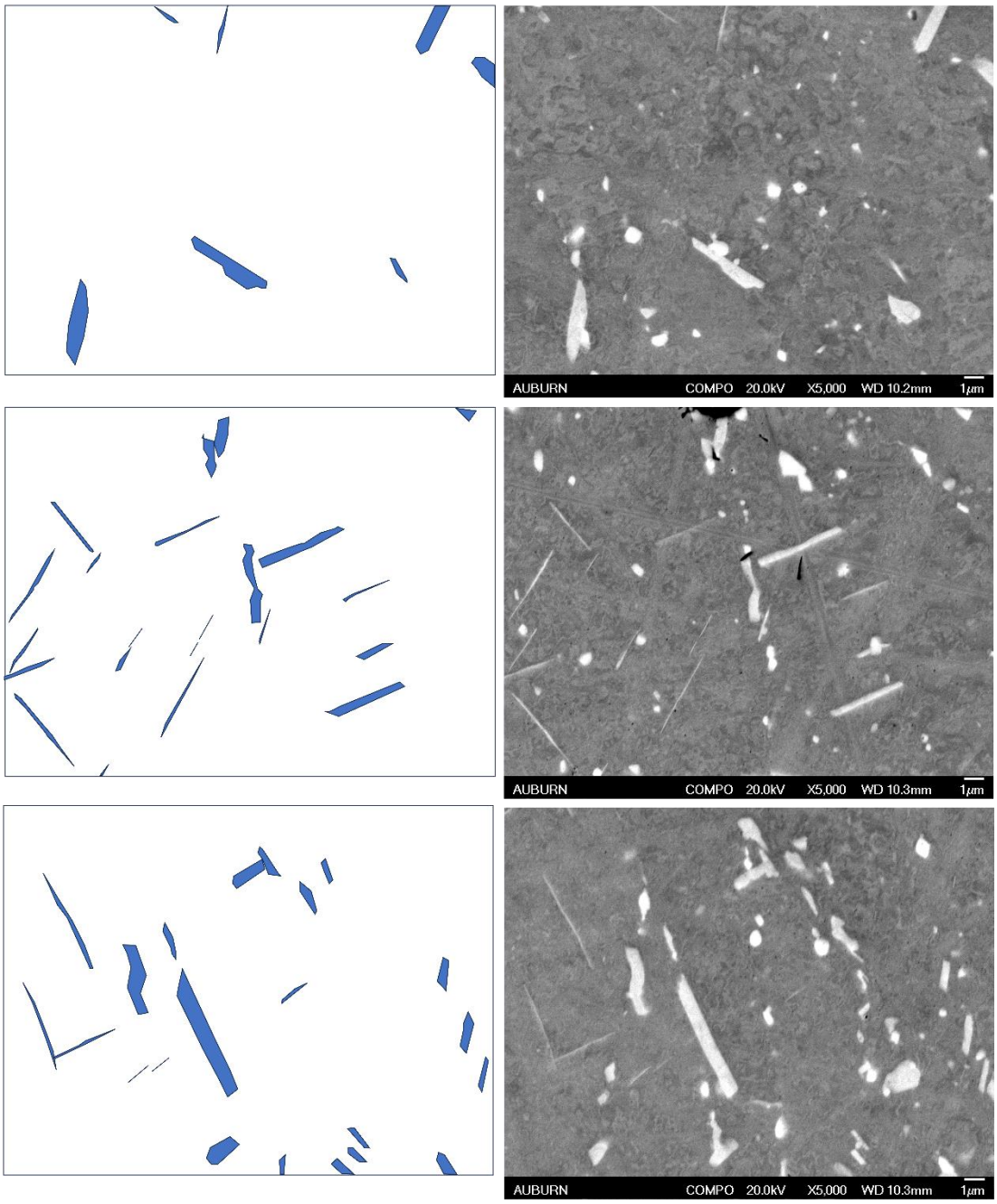

Figure 49: SEM BSE images from internal surface of 900_40h sample.